EPFL

Thèse n° 8656

Cold gas in the cosmic web around galaxy clusters

Présentée le 21 mai 2021

Faculté des sciences de base
Laboratoire d'astrophysique
Programme doctoral en physique

pour l'obtention du grade de Docteur ès Sciences

par

Damien Louis Alexandre SPÉRONE-LONGIN

Acceptée sur proposition du jury

Prof. F. Carbone, président du jury
Prof. P. Jablonka, Prof. J.-P. R. Kneib, directeurs de thèse
Prof. C. Haines, rapporteur
Dr S. García-Burillo, rapporteur
Prof. L. Shchutska, rapporteuse

École polytechnique fédérale de Lausanne

2021

‘Few people realise the immensity of vacancy
in which the dust of the material universe swims.’
— *The War of the Worlds* by H. G. Wells

‘Peu de gens peuvent concevoir l’immensité du vide
dans lequel nage la poussière de l’univers matériel.’
— *La Guerre des Mondes* de H. G. Wells,
traduction de Henry D. Davray

A mon grand-père,

Acknowledgements

It is good practice to thank all the people, who took part and bore with me during this odyssey, which is a thesis. Much like in Homer's poem, mine was also difficult, long and fraught with obstacles. But it was also filled with joyful and rewarding moments. I also met some wonderful people on the way that I would like to thank. The first person I would like to acknowledge is Pascale Jablonka, my PhD advisor, who offered me the opportunity to spend those 4 years (and few months) there. This allowed me to reach one of the few objectives I had set myself: obtaining a PhD in astrophysics. In those 4 years, I have learned a lot, both scientifically and personally. I also had the opportunity to enter in a collaboration, spend some time observing at the Isaac Newton Telescope in La Palma.

I would also like to give special thanks to Christoph and Loïc, my office mates, for the (too ?) long and passionate discussions we have had, as well as the great 'afterwork' moments, that made the PhD life much easier to deal with. That now gives me the opportunity to thank the rest of the great people I have met during those 4 years: Elodie, Claudio, Sophie, Rémy, Olga, Vivien, for the good times in general, Gianluca, for the great discussions on my results and the science in general, Romain, for the motivation we gave each other (or at least tried to) during the last months of our respective thesis, Nicolas, for the coffee breaks, James, for his communicative happiness, and all the other people from LASTRO and Geneva Observatory.

The last 14 months have been pretty rough: finishing a PhD in the middle of a global pandemic, while juggling around the various restrictions, is not something I would recommend. However, during the lockdown of spring 2020, the regular meetings and small challenges between all of us, Pascale, Carmela, Gianluca, Romain, Nicolas and I, were a great way to be entertained.

Je passe en français, car cette section concerne des personnes qui ne sont pas (ou plus) anglophones. Je voudrais tout d'abord remercier mes amis, de plus de 10 ans maintenant, qui m'ont permis de décompresser durant les quelques moments passés ensemble. Enfin, je remercie tout particulièrement ma famille, et surtout mes parents, pour m'avoir apporté le soutien et la motivation nécessaires pour mener mes études jusqu'à ce stade.

D. S-L

Abstract

Galaxies live in very different types of environment. Those different environments are relics from the evolution of the Universe since the Big Bang. This network of structures observed via large scale surveys is called Cosmic Web. Within this web, galaxies can be isolated, in a filament, in a group, or in a cluster. When part of a cluster of galaxies, their morphologies, gas content (cold and hot), and star formation activities is seen to be affected by other galaxies, or by the gas inside the cluster. However, the long-term effects of the local environment on galaxy evolution remain unclear. Also, it has been observed that a pre-processing is happening long before the galaxies enter the cluster cores, which could explain the build-up of the passive galaxy sequence, where galaxies have quenched star formation. The aim of this thesis is to see if and how the cold molecular gas reservoir of galaxies is modified when star formation activity is decreasing and if there is a link with the position of the galaxy in the CW around the cluster.
We gathered unprecedented observations: the first and largest survey of the molecular gas content of galaxies in and around the same cluster environment at intermediate redshifts. These Atacama Large Millimeter Array observations are part of a larger survey called Spatially Extended ESO Distant Cluster Survey. We are focusing on two clusters at a redshift of 0.5, which benefit from previous deep photometric and spectroscopic observations. This will allow us to derive accurate stellar masses and star formation rates, in order to compare those galaxies to other surveys of the cold gas content of galaxies, either in the field or inside different clusters. We unveiled a new population of galaxies with normal star formation rates but less cold molecular gas than other galaxies at the same stellar mass. This could be an indication that the gas reservoir responsible for the star formation changes either in mass or properties, before the star formation is affected. We also noticed that galaxies with the lowest cold-molecular-gas-to-stellar-mass ratios are preferentially either in the cluster core or in overdensities away from the cluster, confirming the existence of a pre-processing in overdensities surrounding the cluster. But active galaxies inside or close to the cluster, do not always have depleted CO reservoir.
This thesis opens up new prospects on the study of the cold gas content of galaxies at intermediate redshift. It showed the necessity to observe galaxies that are in a transition regime between star forming and passive, in order to understand how star formation is suppressed around clusters. Those results could be extended to much larger samples, with the help of the upcoming new generation of instruments such as the Square Kilometer Array.

Key words : galaxy evolution, galaxy clusters, cold molecular gas, submillimeter, intermediate redshift, star formation

Résumé

Les galaxies résident dans différents environnements. Ces différents environnements sont des vestiges issus de l'évolution de l'Univers depuis le Big Bang. Ce réseau de structures, observé par des études à grande échelle, est appelé toile cosmique. Au sein de ce réseau, les galaxies peuvent être isolées, dans un filament, un groupe, ou encore un amas. Lorsqu'elles font partie d'un amas de galaxies, leur morphologie, contenu en gaz (chaud ou froid), et leur capacité à former des étoiles sont perçus comme étant influencés par les autres galaxies, ou le gaz à l'intérieur de l'amas. Cependant, les effets à long terme de l'environnement proche sur l'évolution d'une galaxie restent peu connus. Aussi, un phénonème de pré-transformation a été détecté bien avant que les galaxies n'entrent au cœur de l'amas. Cela pourrait expliquer le développement de la séquence passive, dans laquelle les galaxies ne forment pas ou très peu d'étoiles. Le but de cette thèse est de voir si et comment le réservoir de gaz froid moléculaire des galaxies est modifié lorsque l'activité de formation stellaire diminue, et s'il y a un lien avec la position desdites galaxies dans la toile cosmique autour de l'amas. Nous avons réuni des observations inédites : la première et plus grande étude du contenu en gaz moléculaire de galaxies situées dans le même amas et, surtout autour, à un redshift intermédiaire. Ces observations, obtenues grâce à l'Atacama Large Millimeter Array, font parti d'une étude plus importante qui s'appelle Spatially Extended ESO Distant Cluster Survey. Nous nous concentrons sur deux amas à un redshift de 0,5, et qui bénéficient d'observations photométriques et spectroscopiques profondes, obtenues précédemment. Cela nous permettra d'obtenir des masses et taux de formation stellaires précis, afin de comparer nos résultats à d'autres études sur le gaz froid moléculaire des galaxies de champ et/ou d'amas. Nous avons découvert une nouvelle population de galaxies avec des taux de formation stellaire dans la moyenne, mais avec un déficit en gaz froid comparé à la moyenne des autres galaxies, à même masse stellaire. Cela pourrait indiquer que le réservoir de gaz froid à l'origine de la formation des étoiles, voit sa masse ou ses propriétés modifiées, avant que la formation stellaire ne le soit. Nous avons aussi observé que les galaxies avec le plus faible ratio entre la masse de gaz froid moléculaire et la masse stellaire se trouvent plutôt dans les amas ou dans les milieux éloignés de l'amas où la densité est plus élevée que la moyenne, ce qui conforte la théorie sur la pré-tranformation dans les sur-densités entourant l'amas. Mais, des galaxies actives dans ou proches de l'amas, ne présentent pas toujours un déficit en CO. Cette thèse ouvre de nouvelles perspectives sur l'étude du contenu en gaz froid des galaxies à redshift intermédiaire. Elle montre la nécessité d'observer des galaxies qui sont en transition entre une phase active et une phase passive, afin de mieux comprendre comment l'activité de formation stellaire diminue autour des amas. Ces résultats pourraient être adaptés pour des échantillons beaucoup plus large,

grâce aux futurs instruments tels le Square Kilometer Array.

Mots clés : évolution des galaxies, amas de galaxies, gaz moléculaire froid, submillimétrique, redshift intermédiaire, formation stellaire

Contents

Acknowledgements **i**

Abstract (English/Français) **iii**

1 Introduction **1**
1.1 Cosmic Web 1
1.2 Cold molecular gas 5
1.3 Evolution of galaxies in clusters 6
1.4 Our cluster sample 7
1.5 Objectives of this thesis 10

2 Preliminary work and details about data reduction **11**
2.1 Photometric sample 11
2.2 Photometric corrections 11
2.2.1 Stellar sequence 11
2.2.2 Aperture corrections 12
2.3 Stellar masses and star formation rates 14
2.4 Observational setup 17
2.5 Data reduction 19

3 Paper I : ALMA results for CL1411.1−1148 **21**

4 Paper II : ALMA results for CL1301.7−1139 **39**

5 Conclusions **55**
5.1 Future work 56
5.2 Outlook 57

Curriculum Vitae **63**

1 Introduction

In astrophysics, the further the object, the more we look into the past. Astrophysicists can then be described as historians of the Universe, whose goal is to understand how the Universe evolved from a tiny singularity into the vast, and mostly empty, space we observe today.

In this introduction, we describe the topic of this thesis in details: the theoretical context, the state of the art in the topic and the yet-to-explore features we concentrate on.

1.1 Cosmic Web

The modern view on structure formation and evolution relies on the Λ cold dark matter (ΛCDM) cosmological model. In this framework, three major components are constituting the Universe. The dominant ingredient is the dark energy (69%), which is responsible for the accelerated expansion of the Universe (Riess et al. 1998; Perlmutter et al. 1999). The dark matter (DM) is only susceptible to gravity and accounts for 26% of the total mass-energy content of the Universe (Rubin et al. 1980; Persic et al. 1996). Finally, the visible matter, which only represents 5% of the mass from the total mass-energy budget of the Universe, is the only one detected directly thanks to its electromagnetic emission (Planck Collaboration 2020). The ΛCDM cosmological model is the favoured one, as it is agreeing with a large number of observations.

A scenario explaining the evolution of the Universe and the formation of structures, independent of their sizes, was created from this theory. Shortly after the Big Bang, the Universe was still a hot and dense plasma, when it increased dramatically in size during a phase called inflation. The initial quantum fluctuations grew up to a cosmological scale. They are still visible today via the Cosmic Microwave Background (CMB), which is a relic radiation from when the Universe just became transparent and the photons were able to propagate freely. This inflation induced an intense cooling of these density variations, letting them collapse under their own gravity and form the first stars and galaxies of the history of the Universe. The galaxies additionally attracted each other to form a complex network made of filaments, with overdensities lying at their junctions, called the Cosmic Web (CW). The largest gravitationally bound structures in this network are the

galaxy clusters, constituted of hundreds to thousands of galaxies, which can be traced back to those small density fluctuations (see review by Kravtsov & Borgani 2012).

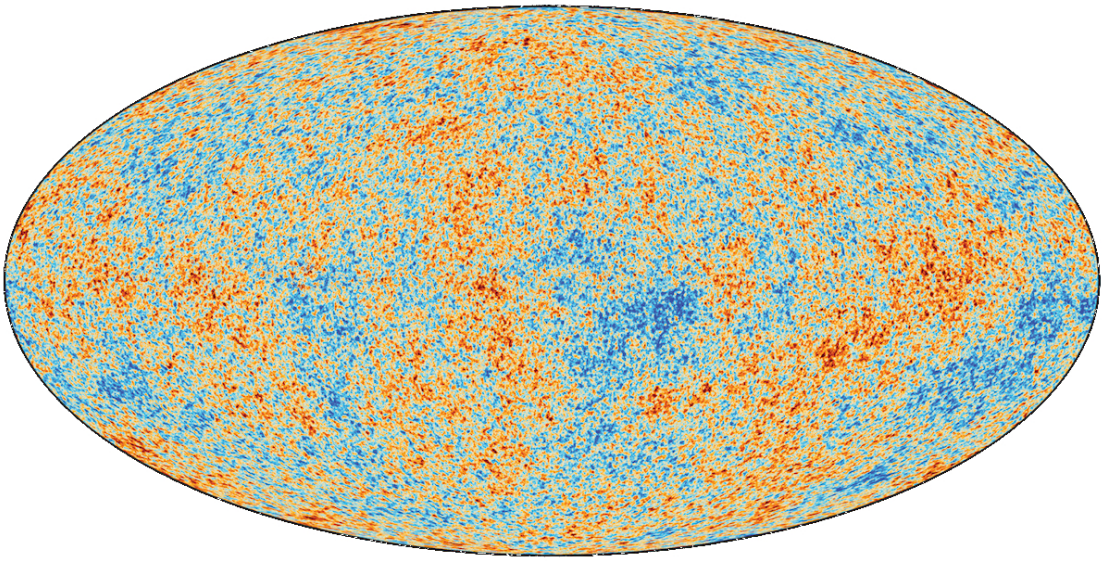

Figure 1.1 – Map of the CMB obtained by the *Planck* satellite and released in 2018. It shows tiny temperature fluctuations, in red and blue, that correspond to regions of slightly different densities, which gave birth to the stars and galaxies of today. Credit: European Space Agency (ESA) and the Planck Collaboration

Many observations confirmed this broad picture. One of them was the direct observation of the CMB. The latest map of the CMB can be seen on Fig. 1.1, which shows the fluctuations in densities as they were when the Universe became transparent, 380 000 years after the Big Bang, observed by the *Planck* satellite.

Another success of this theory is the explanation of the creation, evolution and current distribution of the large scale structures (LSS) of the Universe. This can be seen in Fig. 1.2, where the local distribution of galaxies as a function of redshift and right ascension as it was observed by the Sloan Digital Sky Survey[1] (SDSS), is shown. The maximum redshift on this image would correspond to a distance of $\sim 540\,\mathrm{Mpc}$[2]. Figure 1.3 shows the distribution of dark matter, hence galaxies, in a simulation box of size 800 Mpc[3], where 800 Mpc would correspond to a redshift of $z \sim 0.19$, with our choice of cosmological parameters (see end of Section 1.5). This snapshot is obtained using the SWIFT[3] simulation at a low resolution (Schaller et al. 2016). We clearly see an agreement between the observed and simulated distribution, as the observed filamentary patterns with overdensities at their junctions are well recovered in the simulation.

[1] http://www.sdss3.org/
[2] 1 pc = 1 parsec ~ 3.26 light-years
[3] http://www.swiftsim.com/

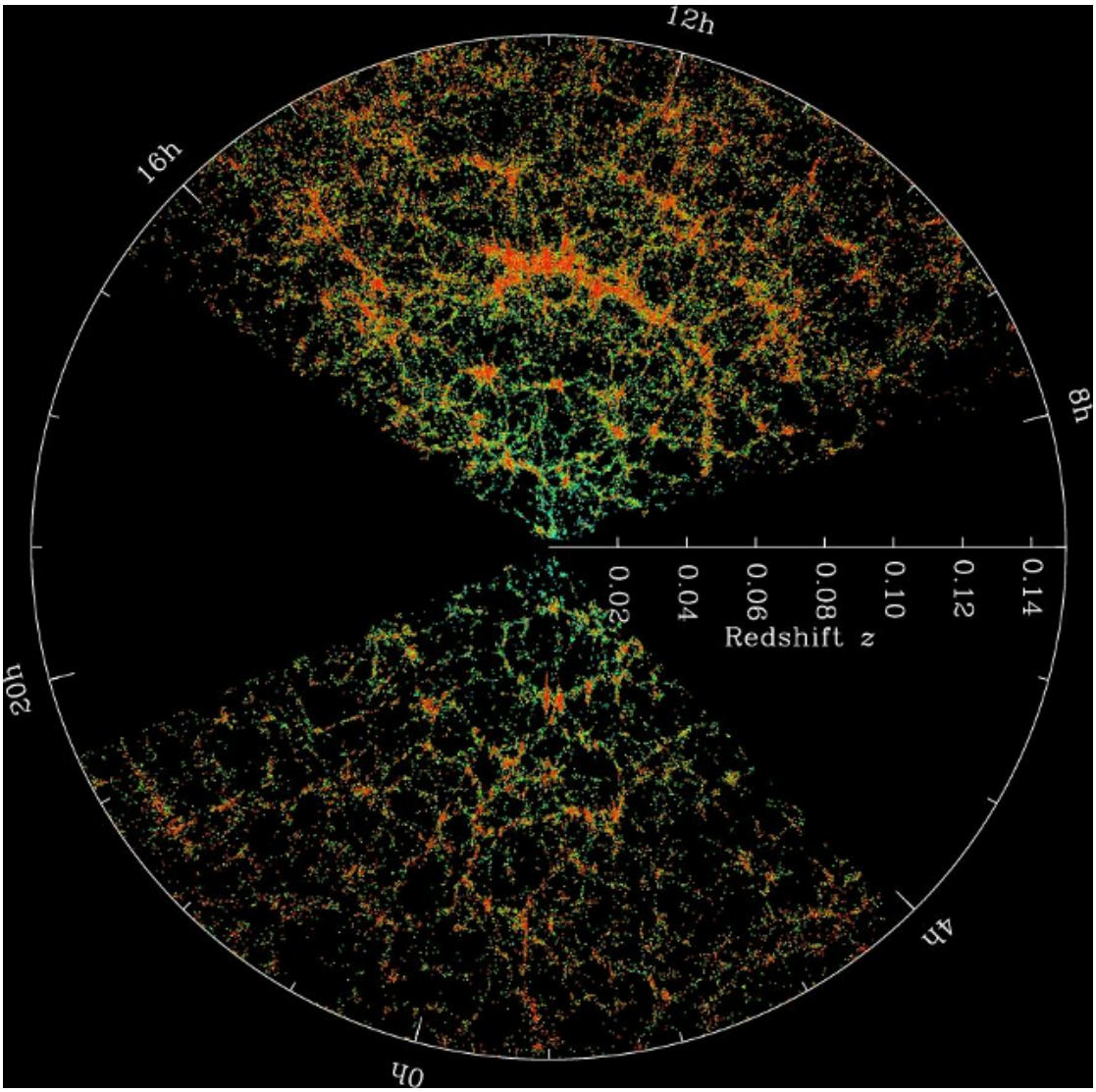

Figure 1.2 – Distribution of the galaxies as a function of redshift and right ascension. This is coming from SDSS observations of the local Universe. The dark wedges correspond to regions obscured by the dust of our own Galaxy. Both slices contain all galaxies within 2.5° in declination. Credit: M. Blanton and the Sloan Digital Sky Survey

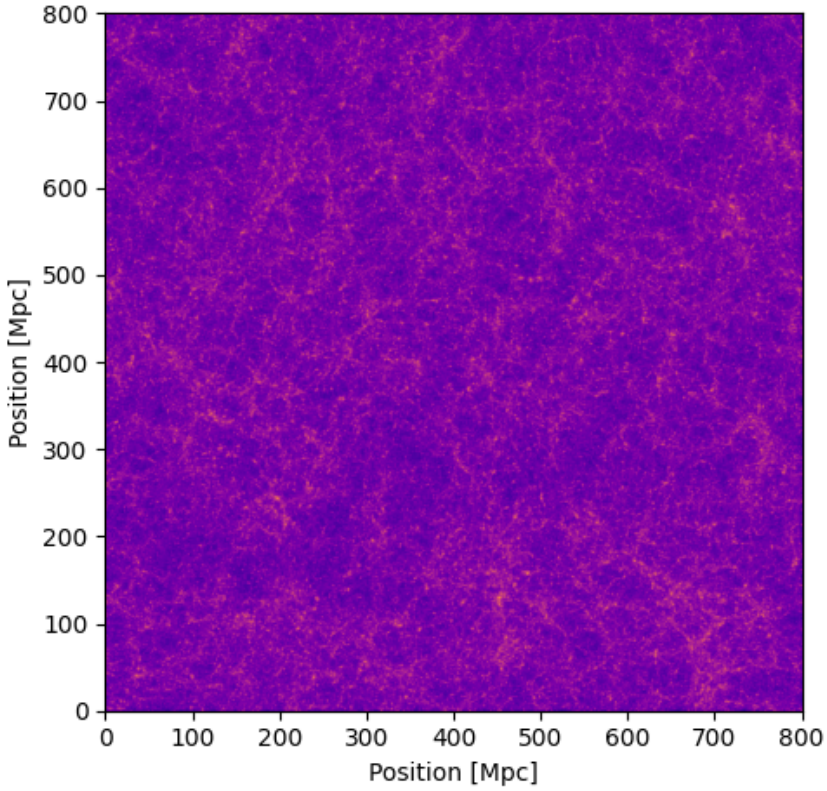

Figure 1.3 – Dark matter density field from the SWIFT simulation (Schaller et al. 2016). It is an homogeneous box of size 800 Mpc^3. It corresponds to a low resolution version of the Millennium simulation. Credit: L. Hausammann and the SWIFT team

1.2 Cold molecular gas

Galaxies are not only made of stars. Most of the mass comes from their dark matter halos, in which the visible matter is trapped (Koopmans & Treu 2003; Hashim et al. 2014). Stars are surrounded by what is called the interstellar medium (ISM). The ISM is primarily composed of hydrogen, in different states (e.g. ionized, atomic, or molecular). Then, we found helium, and, finally, traces of heavier elements such as carbon, oxygen, and nitrogen (Herbst 1995).

This ISM has different components with different properties (e.g. temperature, densities, and hydrogen state). In our galaxy, the Milky Way, the ISM can be broken down in different components (Ferrière 2001). The main component is called the hot ionized medium. It accounts for 30% to 70% of the total volume of the ISM. The temperatures are typically between $\sim 5 \times 10^5$ and 10^7 K. The densities are found to range from about 10^{-4} to 10^{-2} particles per cm^{-3}, and the hydrogen is ionized, (noted H II) as well as the other components. The second component, 20 to 50% in volume, is the warm ionized medium with temperatures close to 8 000 K, with densities between 0.2 and 0.5 particles per cm^{-3}, here again the hydrogen is ionized. The third component is the warm neutral medium, which represents 10 to 20% in volume. It has temperatures between several 10^3 up to 10^4 K. The densities are very similar to those of the warm ionized medium, but the hydrogen is found in its simplest form in this medium: neutral and atomic, and it is denoted H I, as opposed to H II for the ionized hydrogen. H I can be traced via the 21-cm emission line, which is due to a change in the energy state of neutral hydrogen atoms. The cold neutral medium is another component of the ISM. It accounts for less than 5% of the total volume of the ISM. It has temperatures of $\sim$ 100 K and densities between 20 and 50 particles per cm^{-3}. Here again, the hydrogen is found in its neutral and atomic form. The last component, and the one interesting for us, but also making up for less than 1% of the total volume, is made of molecular clouds. In those cold clouds, with T $\sim 10 - 20$ K, the densities are the highest of the ISM with 10^2 to 10^6 particles per cm^{-3}. Those clouds consist of molecular hydrogen H_2, and other molecules constituted of carbon, oxygen or nitrogen (e.g. CO, HCN, HCO).

Stars are born in those cold clouds (Schruba et al. 2011). Hence, looking at the cold molecular gas content of a galaxy gives good insights on its efficiency in forming stars, and subsequently on its star forming activity (Bigiel et al. 2008; Leroy et al. 2008; Schruba et al. 2011). H_2 is the most abundant molecule, with CO, the second one, being four orders of magnitude less abundant. However, H_2 has molecular vibration-rotation lines that require high temperatures to be produced via ultraviolet (UV) excitation or shocks (Geballe et al. 2017). Only then it can be observed and studied in infrared (IR). In the absence of these excitation factors, H_2 is invisible. This is why astronomers require a tracer to be able to observe and study the cold molecular gas. The second most abundant molecule in such clouds, CO, is not a symmetrical molecule. Thus, it does not require special circumstances to be excited. It still requires densities high enough so that the molecules can exist and be protected from photo-dissociative UV radiations thanks to the shielding from the dust and the self-shielding from H_2 (Lequeux 2005). The first ten rotational transitions of CO have different excitation potential, from 5.5 to $\sim$ 305 K, and different critical densities ranging from 2.1×10^3 to 1.1×10^6 cm^{-3} (Carilli & Walter 2013). CO can be observed

in the far-IR regime or radio domain (115.2 to 1 152 GHz), depending on the redshift of the source and the targeted transition.

1.3 Evolution of galaxies in clusters

Galaxy surveys, like SDSS (Strateva et al. 2001), have shown the existence of a strong dichotomy between galaxy populations, in colours, star formation rates (SFR), and morphologies. Galaxies can essentially be described as either red mostly ellipticals with little or no star formation, or blue mainly spirals with active star formation (e.g. Driver et al. 2006; Brammer et al. 2009; Muzzin et al. 2013). It has long been known that there are more galaxies with ellipsoïdal morphologies (e.g. elliptical, or lenticular) in galaxy clusters, than in the field (Dressler 1980; Lewis et al. 2002; Peng et al. 2010). The cold molecular gas content of galaxies is also known to be depleted or at a much lower level in dense environments than in the field, at least in the local Universe (Scott et al. 2013; Boselli et al. 2014).

The main focus of the ongoing research is to understand how and where the quenching (or suppression) of star formation begins and how it works in galaxies. This will eventually lead to understand the growth of the passively evolving galaxy population.

As mentioned, morphology and star formation activity are linked. This implies that, in denser environments, there are physical phenomena that can decrease or even stop the star formation activity of a galaxy, ultimately modifying its morphology. Most of those physical phenomena have been identified: tidal stripping occurring in gravitational interactions and mergers between galaxies (Gnedin 2003); ram-pressure stripping due to the passage through the hot intracluster medium (ICM) (Gunn & Gott 1972; Jachym et al. 2014; Poggianti et al. 2017); thermal evaporation due to interactions between the cold ISM and the hot intergalactic medium (Cowie & Songaila 1977); encounters with other galaxies (‘harassment’, Moore et al. 1996); and the suppression of the diffuse gas reservoir of galaxies (‘strangulation’, Larson et al. 1980; van de Voort et al. 2017; Zhang et al. 2019). Unfortunately, their relative importance, their zone of influence, and their timescales are still debated (Wetzel et al. 2013; Haines et al. 2015; Fillingham et al. 2015; Wagner et al. 2017).

Wetzel et al. (2013) found that there is a long delay between the time of first infall and the time at which a rapid quenching starts for a galaxy infalling onto a cluster. This is the delayed-then-rapid quenching. They found this delay to be between 2 and 4 Gyr after the first infall of the galaxy. But this 2-4 Gyr delay is too long to explain the quenched fraction of galaxies already existing within clusters. By trying to solve this tension, Haines et al. (2015) found that the fraction of star-forming galaxies was lowered as far as 3 virial radii away from the cluster centre, compared to the field, by roughly 19%. This means there is a form of pre-processing taking place in the structures of the cosmic web surrounding the clusters, like the groups or filaments. Moreover, there is ample evidence that the removal of H I gas and, afterwards, the suppression of star formation, happens at large distances from the cluster cores (~2-5 virial radii; Lewis et al. 2002;

Finn et al. 2010; Bahé et al. 2013; Haines et al. 2015; Odekon et al. 2017). It would mean that galaxies are pre-processed over cosmic times before they fall into the cluster cores (e.g. Einasto et al. 2018; Olave-Rojas et al. 2018; Salerno et al. 2020). This pre-processing is thought to take place in the dense structures, like filaments or groups, surrounding the galaxy clusters. Indeed, massive red galaxies have been observed to preferentially lie close to the filament axes (Malavasi et al. 2016; Laigle et al. 2018; Kraljic et al. 2018; Gouin et al. 2020). Another idea is that the hot ICM extends beyond the cluster R_{200} (Zinger et al. 2018), where R_{200} is a good approximation for the cluster virial radius, and is the radius inside which the density is 200 times the critical density of the Universe.

Unfortunately, the cluster infall regions (∼1-5 virial radii) remain poorly studied because of a poor sampling due to the shortage of wide-field deep imaging and accompanying spectroscopy in such extended regions. The first and influential wide-field investigations at intermediate redshift ($z \sim 0.3 - 0.9$) focused on individual very massive clusters ($\sigma \geq 900$ km s^{-1}; e.g. Kodama et al. 2001; Moran et al. 2007; Koyama et al. 2008; Patel et al. 2009; Tanaka et al. 2009; Lemaux et al. 2012). Those surveys highlighted the need for pre-processing well beyond the cluster virial radius.

To date, most studies have focused only on the consequences of quenching (i.e. the properties of the stellar populations). CO observations targeting cluster environments mostly look within R_{200} and at a specific type of galaxies, like in Castignani et al. (2020), where they looked at Luminous Infrared Galaxies (LIRGs) within massive clusters at different redshifts. The effect of the densest environments on the cold molecular gas content of normal star-forming galaxies, which are located within the infall region of a cluster, has never been explored before.

1.4 Our cluster sample

Studies in the local Universe are useful, since they provide direct and detailed observations of galaxies in interaction with their environment. This is simply because these galaxies are close to us and, as a consequence, easier to observe (e.g. Poggianti et al. 2017). However, they only provide a picture of the current state of the galaxies. Their histories cannot be directly recovered. When observing a quiescent galaxy in the local Universe, we do not know where, when, and how the quenching of its star-formation activity took place.

In addition, star formation was much more active in the past. It increased with redshift and peaked at $z = 2$, before decreasing again, as seen on Fig. 1.4, which is taken from Madau & Dickinson (2014). It shows the evolution of the cosmic star formation as a function of redshift and lookback time in Gyr. We can see that the SFR density has been increasing from the young Universe until $z = 2$, at which point, it starts decreasing again. It has decreased by a factor of ~ 4 from $z \sim 0.5$ to $z = 0$. This steady decrease appears to be mainly caused by the decline in the rate of gas accretion onto DM haloes hosting a star-forming galaxy as its central galaxy (e.g. Davé et al. 2012). A central galaxy is the most massive galaxy within the considered DM halo.

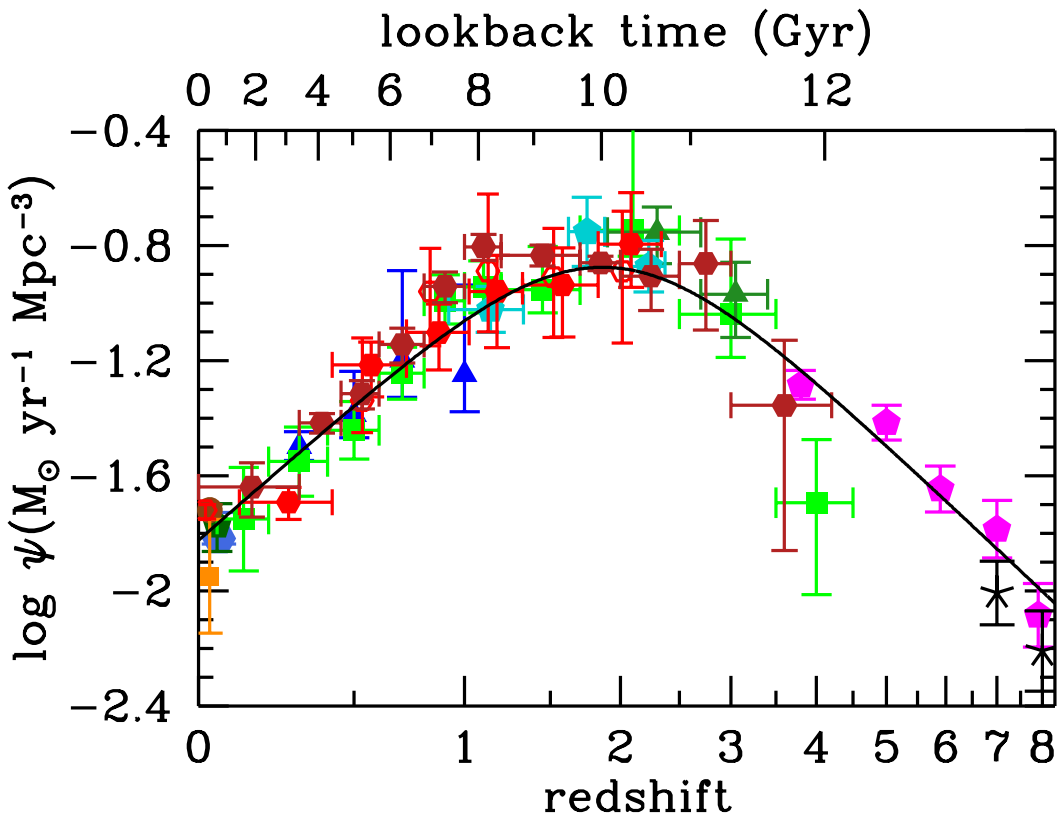

Figure 1.4 – History of the cosmic SFR density from Madau & Dickinson (2014). The peak at $z = 2$ is clearly visible, as well as the rapid decline until today. The rapid decrease by ~ 0.6 dex from $z \sim 0.5$ to $z = 0$, is clearly visible.

Other galaxies within the same DM halo are then called satellites. The rate of star-formation in galaxies is self-regulated and is strongly linked to the rate of gas accretion from its cosmological surroundings, onto the galaxy (e.g. Lilly et al. 2013). Hence, the inevitable quenching once this accretion of fresh gas is cut-off (strangulation).

Moreover, galaxy clusters have substantially increased their masses since $z \sim 1$ (Wechsler et al. 2002; Poggianti et al. 2006) via mergers and accretion of smaller systems.

That means it would be perfect to study clusters between $z = 0$ and 1. This is where the ESO Distant Cluster Survey (EDisCS; White et al. 2005) comes in. It is an ESO large program targeting 26 galaxy clusters spanning line-of-sight velocity dispersions ranging from $\sigma_{\rm cl} = 200$ to 1200 km s^{-1} at intermediate redshift ($z = 0.40$–0.96), each with ~ 20 to 70 spectroscopically confirmed members (Halliday et al. 2004; Milvang-Jensen et al. 2008). Multi-band optical B, V, I, and R photometry and spectroscopy were obtained on the Very Large Telescope (VLT) using the FORS2 instrument, and J and K bands were gathered using SOFI on the New Technology Telescope (NTT). *Spitzer* MIPS 24-micron observations were also conducted in the core of a subset of clusters (Finn et al. 2010).

From this survey, two clusters were selected to be part of a new survey called Spatially Extended EDisCS (SEEDisCS), whose main objective is to study the links between galaxy position in the cosmic web around the same cluster and the evolution status of the galaxy, as well as the status of its cold gas reservoir. Those two clusters are CL1301.7−1139 and CL1411.1−1148 at redshifts $z_{\rm cl} = 0.4828$ and 0.5195, and velocity dispersions $\sigma_{\rm cl} = 681$ and 710 km s^{-1}, respectively. Their intermediate masses make them close analogues to the progenitors of typical local clusters, whose velocity dispersions peak at around 500 km s^{-1} (Milvang-Jensen et al. 2008). Deep u, g, r, i, z and K_s images were taken with the Canada France Hawaii Telescope (CFHT) using the MEGACAM and WIRCam instruments. They cover a region that extends up to $\sim 10 \times R_{200}$. Precise spectroscopic redshifts for galaxies within the field of view (FoV) were obtained using VLT/FORS2, VLT/VIMOS and Hectospec on the Multiple Mirror Telescope (MMT). Robust estimates of spectroscopic redshifts were also obtained for some galaxies via the Low Dispersion Prism (LDP) on the Magellan Telescope.

This thesis relies on previous work done by F. Rerat during his own PhD[4] (Rérat 2015). He performed the data reduction for the photometry, and derived accurate photometric redshifts. He then used those photometric redshifts to create density maps of the clusters and their surroundings. He finally performed the data reduction on the spectroscopy. The selection of the ALMA galaxies relies on the density maps he obtained during his work.

[4] https://infoscience.epfl.ch/record/209267

1.5 Objectives of this thesis

The goal of this thesis is to use the observations of the cold molecular gas content of 49 galaxies inside and around the two SEEDisCS clusters, CL1411.1−1148 and CL1301.7−1139, obtained with the Atacama Large Millimeter Array (ALMA). We are trying to link the galaxy stellar mass build-up and the cosmic evolution of its molecular gas reservoir. We are looking to see if and how the cold molecular gas reservoir of galaxies is modified when star formation is on its way to quenching, and if the position of the galaxy in the CW has an influence on its cold molecular gas content. We applied the following procedure to meet these aims :

1. Obtain ALMA CO observations of carefully selected galaxies in and around the two clusters;
2. Derive accurate CO fluxes from which we obtain the cold molecular gas masses of those galaxies;
3. Retrieve reliable stellar masses and SFRs estimates for those galaxies and all the other galaxies within the MEGACAM FoV;
4. Analyse our results and compare them to other studies.

This thesis is presented as follow. Chapter 2 presents some preliminary and additional work required to be performed on the photometry, an explanation on how we derived and checked the robustness of the stellar masses and SFRs estimates, as well as details about the data acquisition and reduction process of the ALMA observations. Chapter 3 presents the postprint we published about the first results for the CL1411.1−1148 galaxies. Chapter 4 shows the preprint we wrote about results for the CL1301.7−1139 galaxies and the conclusions of the comparison between both clusters. Finally, the conclusions and the future work are summarised in Chapter 5.

All the magnitudes quoted in this thesis are in the AB system. Throughout this thesis, we are using a flat ΛCDM cosmology with cosmological parameters being: $\Omega_m = 0.3$, $\Omega_\Lambda = 0.7$ and $H_0 = 70\,\mathrm{km\,s^{-1}\,Mpc^{-1}}$ (see Riess et al. 2019 and Planck Collaboration 2020), as well as a Chabrier initial mass function (IMF) (Chabrier 2003).

2 Preliminary work and details about data reduction

In this Chapter, we detail some preliminary work that was required before deriving the stellar masses and SFRs of the galaxies, we also explain our method to recover accurate SFRs and stellar masses, and we provide some details about ALMA, the data acquisition, and reduction processes.

2.1 Photometric sample

As stated in Sect. 1.4, the photometry for the SEEDisCS galaxies has been obtained using MEGACAM and WIRCam on the CFHT, and also NEWFIRM on the GEMINI telescope, for $\sim 50\%$ of CL1301.7−1139 MEGACAM FoV. The clusters and their outskirts were observed in 6 filters u, g, r, i, and z, in the optical, as well as K_s in near infrared (NIR). The details about the observations are provided in Table 2.1.

2.2 Photometric corrections

We verified and adjusted the zeropoints of the photometry with the help of the stellar sequence, and we also computed the total magnitudes, via the computation of the aperture corrections.

2.2.1 Stellar sequence

The identification of the stellar sequence has been achieved by Covey et al. (2007). They took the SDSS data and tried to identify the common loci of main sequence stars in the different colours obtained by combining the SDSS filters as a function of the $g - i$ colour. In our case, we selected the stars in both CFHT/MEGACAM fields and plotted different colours: $r - i$, $u - g$, $i - z$ and $g - r$ as a function of $g - i$. The top row of Fig. 2.1 presents the uncorrected stellar sequences for both fields compared to the tabulated sequences, adapted to the CFHT/MEGACAM filterset, from Covey et al. (2007). We clearly see that there are some differences in all cases for CL1411.1−1148 and only in two cases, $u - g$ and $i - z$, for CL1301.7−1139. For CL1411.1−1148,

Table 2.1 – Summary of the already available observations. The magnitude limits $m_{\rm lim}$ is defined as the magnitude integrated in 1" radius apertures for a signal-to-noise ratio of 10 ± 0.1.

Field	Filter	Exp. time (s)	Seeing (")	$m_{\rm lim}$ (mag)
CL1411.1−1148				
	u	14675	1.13	24.68
	g	7720	0.82	24.61
	r	500	0.74	22.58
	i	1440	0.55	22.75
	z	6800	0.70	22.42
	K_s	11000	0.62	21.83
CL1301.7−1139				
	u	2621	0.92	23.04
	g	15120	0.75	24.73
	r	500	0.66	23.07
	i	1620	0.88	23.13
	z	7480	0.68	22.22
	K_s (NEWFIRM)	5580	1.68	20.81

we found that correcting u by 0.25 mag, r by −0.08 mag and z by 0.03 mag put our stellar sequences in line with the Covey et al. (2007) results. For CL1301.7−1139, it was only necessary to modify u by 0.16 mag and z by 0.1 mag to obtain stellar sequences close to the SDSS ones. Bottom row of Fig. 2.1 presents the stellar sequences after the corrections were applied, for each cluster: CL1411.1−1148 on the left and CL1301.7−1139 on the right.

2.2.2 Aperture corrections

The aperture correction consists in the derivation of the evolution of the flux of an unsaturated star as a function of the radius of the aperture from which it is integrated. This is called the curve of growth (COG). This allows to correct the AUTO flux which is derived from the Kron aperture computed by SExractor (Bertin & Arnouts 1996) to get the total flux.

To obtain the curve of growth, we selected unsaturated, bright and isolated stars for which we computed fluxes at different apertures, up to 40 pixels. We normalized them individually and took the median value at each radius to create the composite COG.

Then, we computed the equivalent radius of the AUTO aperture for each galaxy. This equivalent radius was then referenced against the normalized COG to find the amount of flux missing, which is the correction factor to apply to the AUTO flux to recover the TOTAL flux. The correction factors obtained for the photometric cluster members, including the ALMA targets as well as the rest of the spectroscopic members, are visible on Fig. 2.2 for CL1411.1−1148 on the left and CL1301.7−1139 on the right. The aperture corrections we derived for CL1411.1−1148 are comprised between 0.6 and 1 with the median value being 0.918. For CL1301.7−1139, the

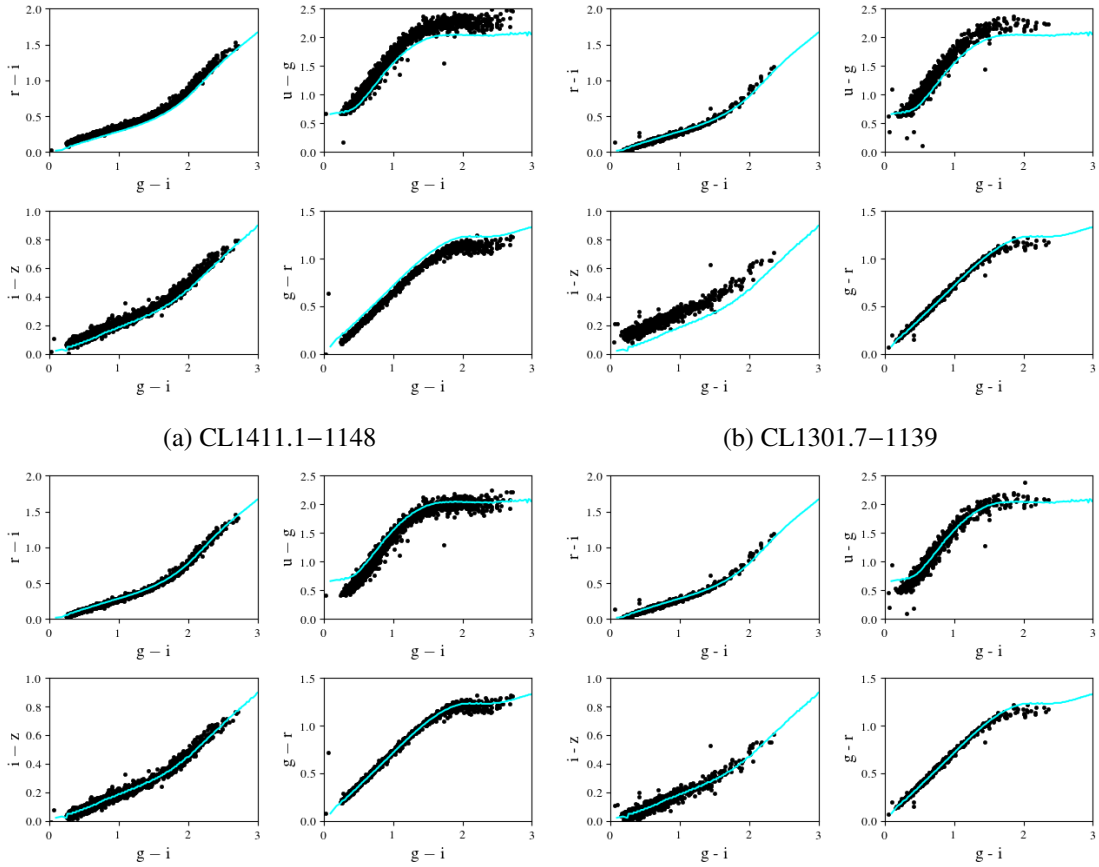

(a) CL1411.1−1148

(b) CL1301.7−1139

(c) CL1411.1−1148

(d) CL1301.7−1139

Figure 2.1 – *Top:* Uncorrected stellar sequences for CL1411.1−1148 (left) and CL1301.7−1139. From left to right and top to bottom, the colour-colour diagram are as follow: $r-i$ vs $g-i$, $u-g$ vs $g-i$, $i-z$ vs $g-i$ and $g-r$ vs $g-i$. The cyan lines correspond to the model stellar sequences (Covey et al. 2007), which are our reference sequences.
Bottom: Corrected stellar sequences for CL1411.1−1148 (left) and CL1301.7−1139 (right). We can see that the stellar sequences for all colours align quite well with the reference sequences.

corrections factors are ranging from 0.55 up to 1 with a median of 0.856. That means that we were missing more than 10% of the flux for a significant portion of our galaxies.

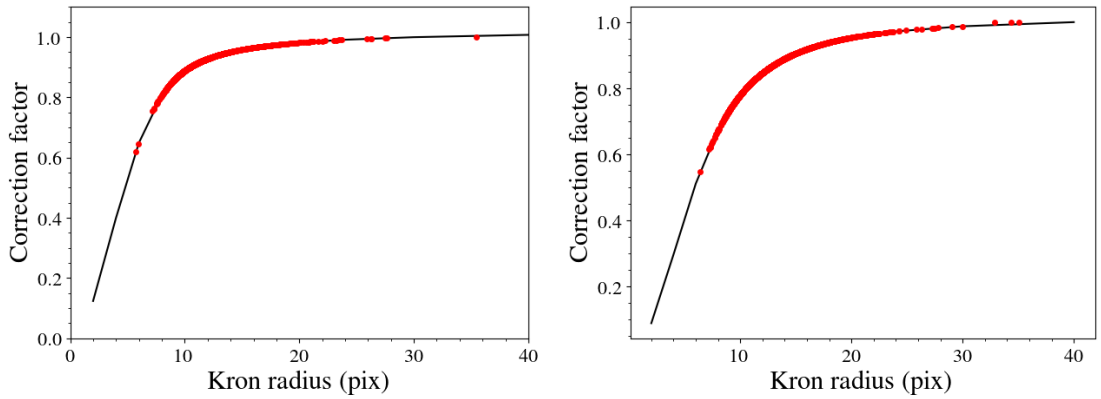

(a) CL1411.1−1148 (b) CL1301.7−1139

Figure 2.2 – Aperture corrections applied to the galaxies within the photometric cluster members, and including the ALMA and spectroscopic cluster members, in red, with the corresponding curve of growth derived from the flux evolution with aperture of bright, unsaturated and isolated stars within the FoV, in black. The majority of our galaxies ends up with aperture correction factor between 0.8 (0.6) and 1 (1) for CL1411.1−1148 (CL1301.7−1139).

Correcting for the stellar sequence and the aperture correction was the first necessary step before we were able to derive reliable stellar masses and SFRs.

2.3 Stellar masses and star formation rates

Deriving accurate stellar masses and SFRs was another challenge during this thesis. Since we only had six bands at our disposal: u, g, r, i, z, and K_s. Computing the SFRs from the IR luminosity is then impossible and we have to rely on another method. We used MAGPHYS[1] to derive the stellar masses and SFRs (da Cunha et al. 2008). MAGPHYS is performing spectral energy distribution (SED) fits, using the observed fluxes (u to Ks, in our case) and provides probability density functions (PDFs) for each fitted parameter (e.g. SFR, M_{star}, dust mass, dust temperature) using different models of stellar populations and dust extinction. The stellar populations and dust extinction models we are using, are those of Bruzual & Charlot (2003) and Charlot & Fall (2000). For each quantity, we have considered the peak value of the PDFs and our uncertainties correspond to the 68% confidence interval of the same PDFs. We are sure we do not have any active galactic nuclei (AGNs) in our sample. Even though the wavelength coverage of our photometric bands does not allow for the identification of AGNs, the analysis of the [OII] to Hβ line ratio indicates that most likely the emission lines in our galaxies are not typical of AGNs (Sánchez-Blázquez et al. 2009). This also is in agreement with the observation that there are less AGNs in clusters (< 3%) than in the field (Miller et al. 2003; Kauffmann et al. 2004; Mishra &

[1] http://www.iap.fr/magphys/index.html

Dai 2020).

In order to check the robustness of our estimates, we needed far-IR flux. Luckily, there are some observations of galaxies in the core of our clusters with *Spitzer*/MIPS at 24 μm from Finn et al. (2010). There are four galaxies in total, two in each cluster. The 24 μm flux (corresponding to $\sim 16\,\mu$m at $z \sim 0.50$) allows us to better constrain the dust emission and judge of its impact on the derived quantities. The two galaxies in the core of CL1301.7−1139 are not included in the ALMA sample for this field but benefit from accurate spectroscopic redshifts obtained with VLT/FORS2. It is worth mentioning that, for CL1301.7−1139, the CFHT/WIRCam K_s observations were not finalized at the time of this thesis so it was necessary for us to find K-band fluxes from other sources. This was made possible thanks to the original EDisCS observations of the cluster cores in K-band from NTT/SOFI as well as some more K_s-band observations at higher distances from the cluster cores using GEMINI/NEWFIRM (catalogue provided by G. Rudnick, and data reduced by T. Desjardins). This ensures that a significant amount of the ALMA targets from CL1301.7−1139 benefit from the same photometric range as the ALMA targets from CL1411.1−1148.

Figure 2.3 presents the SED fits and the corresponding likelihood distribution of M_{star} and SFR for EDCSNJ1411028−1147006, EDCSNJ1411036−1148506, EDCSNJ1301501−1140372 and EDCSNJ1301302−1138188. For all 4 galaxies, M_{star} stays identical with or without the 24 μm flux. As to the SFR, the PDFs of EDCSNJ1411028−1147006 are essentially identical with or without the 24 μm flux point. For the two CL1301 galaxies, the PDFs are almost identical and the median values are close to each other in both cases. For EDCSNJ1411036−1148506, it is different. Its SFR PDF is wider without the 24 μm flux point (peak value at log(SFR) = 0.5) than when it is calculated with the 24 μm point (peak value at log(SFR) = 0.8). The 2 PDFs have medians within 0.3 dex and are highly overlapping, hence the SFR estimates are consistent with each other. EDCSNJ1411036−1148506 is the faintest galaxy of our CL1411.1−1148 sample in the i-band and is probably seen edge-on. Its UV flux is very low, with the deepest restframe 4000 Å break, hence representing the most challenging/dusty case of our sample.

As MIPS 24 μm fluxes were not available for most of our galaxies, we turned towards *Wise*. We looked for our targets in the CatWise2020 catalog (Eisenhardt et al. 2020). Only W1 and W2 fluxes, at 3.4 and 4.6 μm, respectively, were available for most of our targets, including the galaxies we had MIPS fluxes for. At intermediate redshifts ($z \sim 0.5$), the W1 band is probing stellar emission only, while the W2 bands is probing both stellar and dust emissions (Duley & Williams 1981; Leger & Puget 1984; Allamandola et al. 1985). This means they could help us to better constrain the dust emission, hence the extinction and, as a result, the SFRs of our galaxies. We looked at how the Wise fluxes would change, or not, the SED fits of the galaxies, which have 24 μm fluxes available. It turned out that the *Wise* fluxes made our SED fits worse than they were before in most cases, whether we used the 24 μm fluxes or not. Indeed, the chi-square of the fits when *Wise* fluxes are added are either unchanged, for 1 out of the 4 galaxies or multiplied by 3 to 10 for the other 3 galaxies, with the biggest difference arising when W1, W2 and MIPS24 fluxes are used together on top of the other 6 bands (u to K_s). This discrepancy in the fits due to the *Wise*

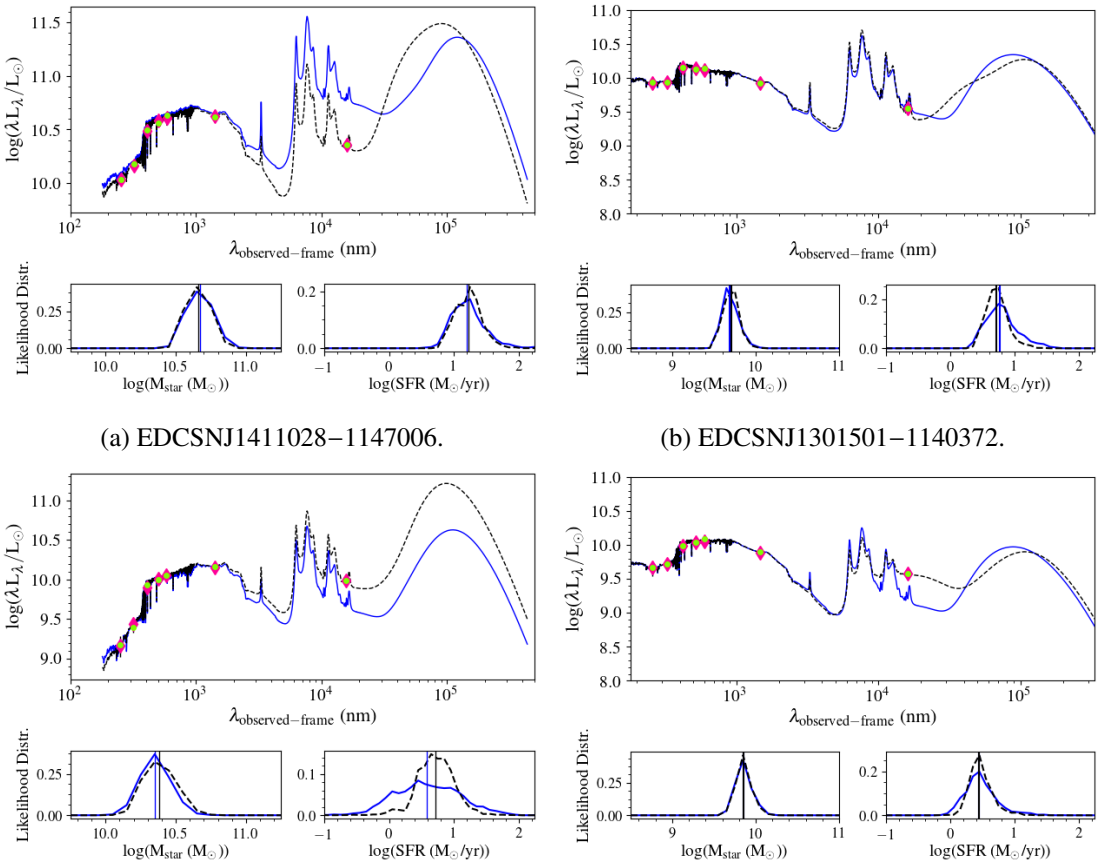

(a) EDCSNJ1411028−1147006.

(b) EDCSNJ1301501−1140372.

(c) EDCSNJ1411036−1148506.

(d) EDCSNJ1301302−1138188.

Figure 2.3 – SEDs and likelihood distributions for the 4 *Spitzer*-observed galaxies: EDCSNJ1411028−1147006 (a), EDCSNJ1301501−1140372 (b), EDCSNJ1411036−1148506 (c), and EDCSNJ1301302−1138188 (d). The blue curves are without the MIPS 24 μm fluxes and the black dashed ones are with the MIPS 24 μm fluxes. The top panel of all figures show the fitted SEDs in black and blue as well as the observed fluxes, in green and the model fluxes in pink. The 2 bottom panels of each figure show the likelihood distributions for M_{star} and SFR, and the medians for the M_{star} and SFR, as the blue and black vertical lines, derived with MAGPHYS.

fluxes also has an impact on our galactic parameter estimates, like SFR. The addition of Wise fluxes tend to modify the SFR by about 50%. Stellar masses on the other hand are left unaltered. Moreover, for the sources for which we know extinction is high, the SED fits performed by MAGPHYS when we add the Wise fluxes, give us galaxies with no or very low dust content. Hence, the SED fits find that the galaxies have no or very low extinction, which is not agreeing with the observations. For these reasons, we decided to not use Wise fluxes for our SED fits as they seem to degrade the quality of our estimates.

In summary, our stellar mass estimates are robustly derived from u to K_s photometry. As for the SFRs, missing the *Spitzer* 24 μm flux could lead to underestimated values, but our error bars are realistic enough to take this possibility into account.

2.4 Observational setup

The targets we selected were observed using ALMA (see Chapters 3 and 4 for the selection criteria). ALMA is an array of 66 antennas: 54 of those are 12 m in diameter, while the rest, 12, are 7 m in diameter. It is located in the Atacama Desert at 5000 metres above sea level on the Chajnantor plateau in Chile. Those antennas provide a range of operation at wavelengths between 3.6 and 0.32 mm (31 to 1 000 GHz). The baselines (distance between 2 antennas) can range from 150 m to 16 km. Fig. 2.4 shows an aerial view of the centre of ALMA with both types of antennas visible.

In our case, we are interested in the third, $J = 3 \rightarrow 2$, rotational transition of the CO molecule, which happens at 345.796 GHz (0.867 mm) at rest and at 230.530 GHz (1.3 mm) at $z = 0.5$. We decided to use this transition because it is tracing hotter and denser clouds than $J = 1 \rightarrow 0$ or $J = 2 \rightarrow 1$, and no other transitions were reachable at the time of observations, due to corresponding frequency bands not being available. Indeed, the $J = 1$ and $J = 2$ states are only 5.5 and 17 K above ground level, while $J = 3$ is at 33 K, and consequently traces a component of higher excitation. But also, the critical density for the third level is $\sim 10^5\,\mathrm{cm}^{-3}$, while it is $\sim 10^3$ and $\sim 10^4$ for the two lower rotational transitions. CO(3-2) may not be present in large quantities in galactic disks, but is particularly present in central regions of galaxies, where the star formation activity is the last to stop, and where the environmental effects are the least perceived. The CO(3-2) emission line at $z \sim 0.5$ falls right into the bandwidth of the Band 6 detector of ALMA. This band covers a frequency range of 64 GHz between 211 and 275 GHz (1.4 to 1.1 mm).

Our observations were obtained during two cycles. The first batch of data was obtained during Cycle 3 of ALMA, where 18 fields for CL1411.1−1148 were observed. The second batch was acquired during Cycle 5. This last cycle allowed us to get data for the 14 remaining CL1411.1−1148 fields and for all of the 24 CL1301.7−1139 fields. Table 2.2 presents a summary of the ALMA observations. We are reporting detections for 14 fields out of the 18 targeted during Cycle 3, which corresponds to a 77.8% detection rate. Those 4 non-detections are either

Figure 2.4 – Aerial view of the centre of ALMA. The 7-m antennas are visible on the left in a compact configuration. The 12-m antennas are all pointing in the same direction.

due to a wrong z_{spec} estimate from LDP, or to a genuine non-detection. For Cycle 5, out of the 14 fields targeted around CL1411.1−1148, 1 led to a non-detection, which is due to a wrong LDP estimate, and for the other one, the primary target was not detected, but a secondary one was, located a few arcseconds below. This gives us a 92.9% detection rate for this second batch of observations. For CL1301.7−1139, 24 fields were observed, and 20 targets were observed. We report 3 non-detections as upper limits, including 2 within the same field. The last two non-detections are due to wrong estimates of z_{spec} from LDP. This gives us an 83.3% detection rate for CL1301.7−1139. All in all, we report a total detection rate of 83.9%, which can be compared to the 90.2% detection rate of PHIBSS2 (Freundlich et al. 2019), when removing marginal detections. The PHIBSS2 very high detection rate is probably due to the selection criteria they used on their galaxies. The effects of such criteria are discussed in both papers, in Chap. 3 and 4.

Table 2.2 – Summary of the ALMA observations.

Program ID	Date	Cluster	Configuration	Nb antennas	RMS (mJy/beam)	Resolution
2015.1.01324.S	Apr 2016	CL1411.1−1148	C36-2 & C36-3	38 - 42	0.074 - 0.15	0.9"
2017.1.00257.S	Jun 2018	CL1411.1−1148	C43-2	45 - 50	0.073 - 1.39	1.1"
	Jul 2018	CL1301.7−1139	C43-2	43 - 46	0.029 - 0.084	1.1"

2.5 Data reduction

The ALMA data reduction process is standardized through the use of a self-calibration process that enables users to check for any discrepancies in the data, e.g. badly behaving antennas and/or detectors, and incomplete runs. Those discrepancies are then flagged and the self-calibration pipeline is rerun without the flagged data.

Once this first process is performed, we use CASA (McMullin et al. 2007), which is a package of routines to get images and spectra from self-calibrated ALMA observations. As our targets have been observed together in different sessions, we have to split and join all the data for each and every source. At this point, we are still working with the raw output, called visibilities. Those visibilities correspond to the Fourier transform of the sky brightness distribution. To obtain images and be able to work with the data, we need to perform the reverse Fourier transform on the visibilities. This second step issues data-cubes for each of our sources containing the spatial and spectral information for each pixel. Then, the continuum is fitted over the entire spectral range, except for the channels corresponding to the emission line, and subtracted. The next step consists of the correction of the images for the primary beams, i.e. deconvolving the images by minimizing distortions induced by secondary features from the primary beam. During this step, one can adapt the spectral resolution by binning or not the spectral channels.

The final continuum-subtracted primary-beam-corrected data-cubes were then used to derive the molecular gas masses (M_{H_2}) of our galaxies.

The data-cubes have been exported to be analysed using GILDAS[2]. GILDAS is a collection of routines oriented toward (sub-)millimetre radio-astronomical applications. In our case, we are using the GREG suite, included in GILDAS, which allows us to display and work with our data-cubes.

Fluxes, $S_{CO}\,\Delta V$, have been extracted by selecting the velocity window centred on the CO(3-2) peak emission and maximizing the flux over it and the spatial extent of the source. An example for galaxy SEDCSJ1410463−1145508 is shown on Fig. 2.5, where the spatial extent and the velocity window used to compute the flux are shown on the bottom left and bottom right panels as a black circle and a yellow zone, respectively.

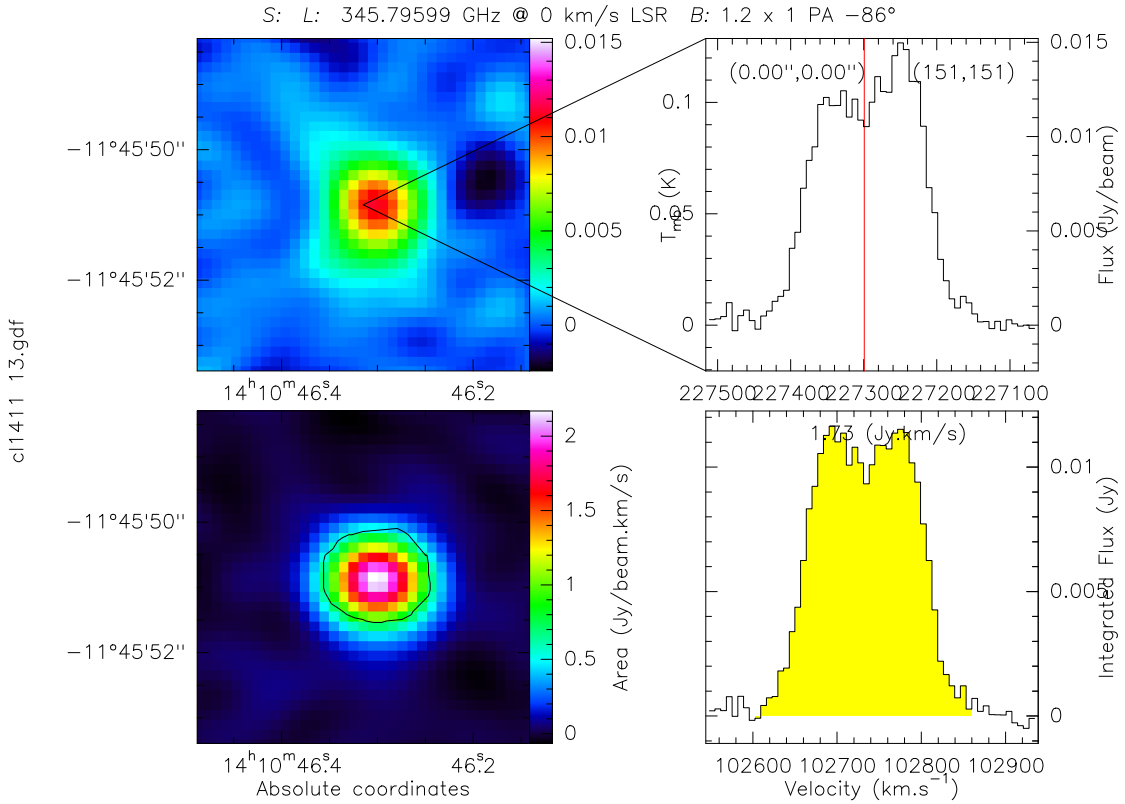

Figure 2.5 – Example of the GREG UI used to derive the CO(3-2) flux for SEDCSJ1410463−1145508. Top left panel shows the emission map at the selected frequency (red line on top right panel), while the top right one shows the spectrum of the selected pixel. Bottom row shows integrated emission map (left panel) over the range of frequencies selected on the right panel (yellow zone). The lower right panel shows the spectrum integrated over the polygon drawn on the lower left panel. The value on top of this panel is the flux as computed by GILDAS, and the value used for the M_{H_2} calculations.

[2]http://www.iram.fr/IRAMFR/GILDAS

3 Paper I : ALMA results for CL1411.1−1148

This Chapter presents the postprint[1] we published in Astronomy & Astrophysics about the results we obtained for our first SEEDisCS cluster CL1411.1−1148.

We report the observation and the analysis of the first sample of CO detections performed around the same cluster environment at intermediate redshift. We also notice that some galaxies, even if they are normal star-forming galaxies, had low cold gas content, for their stellar mass. Such galaxies represent 37% of our 27 ALMA galaxies and their distribution is deviant from the expected tail of a Gaussian distribution and reveals a new population that was absent from other surveys. This new population of low-μ_{H_2} galaxies does not have lowered SFRs compared to field galaxies at the same stellar mass. This suggests that their cold molecular gas reservoir changes, either in mass or properties, before the SF activity does. No correspondence has been identified between the low gas content of our galaxies and the cluster-centric distance nor the local density.

[1] https://doi.org/10.1051/0004-6361/202038904

Astronomy & Astrophysics manuscript no. CL1411_CO_reref_corr_vfinal
March 29, 2021

SEEDisCS I. Molecular gas in galaxy clusters and their large-scale structure

The case of CL1411.1−1148 at $z \sim 0.5$

D. Spérone-Longin[1,⋆], P. Jablonka[1,2], F. Combes[3,4], G. Castignani[1], M. Krips[5], G. Rudnick[6], D. Zaritsky[7], R. A. Finn[8], G. De Lucia[9], and V. Desai[10]

[1] Laboratoire d'astrophysique, École Polytechnique Fédérale de Lausanne (EPFL), Observatoire de Sauverny, 1290 Versoix, Switzerland
[2] GEPI, Observatoire de Paris, PSL University, CNRS, 5 Place Jules Janssen, 92190 Meudon, France
[3] Observatoire de Paris, LERMA, CNRS, Sorbonne University, PSL Research University, 75014 Paris, France
[4] Collège de France, 11 Place Marcelin Berthelot, 75231 Paris, France
[5] IRAM, Domaine Universitaire, 300 rue de la Piscine, 38406 Saint-Martin-d'Hères, France
[6] Department of Physics and Astronomy, The University of Kansas, Lawrence, KS, USA
[7] Steward Observatory and Department of Astronomy, University of Arizona, Tucson, AZ, USA
[8] Department of Physics and Astronomy, Siena College, Loudonville, NY, USA
[9] INAF – Osservatorio Astronomico di Trieste, Via G. B. Tiepolo 11, 34143 Trieste, Italy
[10] IPAC, Mail Code 100-22, Caltech, 1200 E. California Boulevard, Pasadena, CA, USA

ABSTRACT

We investigate how the galaxy reservoirs of molecular gas fuelling star formation are transformed while the host galaxies infall onto galaxy cluster cores. As part of the Spatially Extended ESO Distant Cluster Survey (SEEDisCS), we present CO(3-2) observations of 27 star-forming galaxies obtained with the Atacama Large Millimeter Array (ALMA). These sources are located inside and around CL1411.1−1148 at $z = 0.5195$, within five times the cluster virial radius. These targets were selected to have stellar masses (M_{star}), colours, and magnitudes similar to those of a field comparison sample at similar redshift drawn from the Plateau de Bure high-z Blue Sequence Survey (PHIBSS2). We compare the cold gas fraction ($\mu_{H_2} = M_{H_2}/M_{star}$), specific star formation rates (SFR/M_{star}) and depletion timescales ($t_{depl} = M_{H_2}/SFR$) of our main-sequence galaxies to the PHIBSS2 subsample. While the most of our galaxies (63%) are consistent with PHIBSS2, the remainder fall below the relation between μ_{H_2} and M_{star} of the PHIBSS2 galaxies at $z \sim 0.5$. These low-μ_{H_2} galaxies are not compatible with the tail of a Gaussian distribution, hence they correspond to a new population of galaxies with normal SFRs but low gas content and low depletion times ($\lesssim 1$ Gyr), absent from previous surveys. We suggest that the star formation activity of these galaxies has not yet been diminished by their low fraction of cold molecular gas.

Key words. galaxies: evolution – galaxies: clusters: general – submillimeter: galaxies

1. Introduction

Galaxy surveys have revealed a strong bimodality of the galaxy population in colour, star formation rates (SFRs), and morphology (e.g., SDSS, Strateva et al. 2001). Galaxies can indeed be broadly described as either red predominantly early-type galaxies with little or no star formation or blue predominantly late-type galaxies with active star formation (e.g. Driver et al. 2006; Brammer et al. 2009; Muzzin et al. 2013). A major thrust of the ongoing research is to understand how the quenching of star formation starts and works in galaxies, which leads ultimately to the build-up of the passively evolving population. The fraction of star-forming galaxies is the lowest inside galaxy clusters, while at the same time the fraction of early-type morphologies (lenticulars, ellipticals) is the lowest in the field (Dressler 1980; Blanton & Moustakas 2009). There is no shortage of proposed physical mechanisms to explain how galaxies stop forming stars at a higher frequency in clusters relative to the field: tidal stripping (Gnedin 2003), ram-pressure stripping (Gunn & Gott 1972), thermal evaporation (Cowie & Songaila 1977), encounters with other satellites ('harassment', Moore et al. 1996), and removal of the diffuse gas reservoir of galaxies ('strangulation', Larson et al. 1980; Zhang et al. 2019). However, we are still lacking the observational evidence that will distinguish between the relative importance of the different mechanisms put forward and set their sphere of influence.

Interestingly, the removal of HI gas and suppression of star formation seems to occur at large distances from the cluster cores (∼2-4 virial radii; Solanes et al. 2002; Gomez et al. 2003; Haines et al. 2015). The implication is that galaxies are possibly pre-processed over cosmic time before they fall into the cluster cores (e.g. Einasto et al. 2018; Olave-Rojas et al. 2018; Salerno et al. 2020); our current understanding is that the largest gravitationally bound overdensities in the initial Λ cold dark matter (ΛCDM) density field collapse and gradually merge to form increasingly more massive clusters connected by filaments (Springel et al. 2018). This network of matter, called the cosmic web, is observed up to a redshift of $z \sim 1$ (Pimbblet et al. 2004; Kitaura et al. 2009; Guzzo et al. 2018) and is a potential site for pre-processing. One piece of evidence for this is that massive

⋆ e-mail: damien.sperone-longin@epfl.ch

red galaxies have preferentially been found close to the filament axes (Malavasi et al. 2016; Laigle et al. 2018; Kraljic et al. 2018; Gouin et al. 2020). Another possibility is that the cluster environment, and in particular the hot intracluster medium, actually extends beyond the cluster virial radius (Zinger et al. 2018).

Unfortunately, the cluster infall regions still remain poorly explored around galaxy clusters due to the dearth of deep imaging and accompanying spectroscopy in these extended regions. The first and seminal wide-field investigations at intermediate redshift ($z \sim 0.3-0.9$) focused on individual very massive systems ($\sigma \geq 900$ km s^{-1}; e.g. Kodama et al. 2001; Moran et al. 2007; Koyama et al. 2008; Patel et al. 2009; Tanaka et al. 2009), or even superclusters (Lemaux et al. 2012). They highlighted the need for a variety of physical quenching processes acting well beyond the cluster virial radii. Larger surveys followed such as the CLASH-VLT survey (Biviano et al. 2013), the ORELSE survey(Lubin et al. 2009), the PRIMUS survey (Berti et al. 2019), and the IMACS cluster building survey (Dressler et al. 2013), leading to improved sampling of datasets and analyses.

To date most studies have focused only on the consequences of quenching (i.e. the properties of the stellar populations). The gas that fuels star formation, which is ultimately what must be affected to stop star formation, has barely been explored in dense environments. We have undertaken a new approach, which has the significant advantage of allowing us to link the galaxy stellar mass build-up and the cosmic evolution of the galaxy molecular gas reservoir. In other words, it allows us to establish how molecular gas is fuelling star formation, and how it is modified when star formation is on its way to quenching (e.g. Castignani et al. 2020).

In order to shed light on the above issues, we are conducting a survey of the large-scale structures (LSS) around two spectroscopically well-characterised, intermediate-redshift, medium-mass clusters. They are selected from the ESO Distant Cluster Survey (EDisCS; White et al. 2005). This paper presents our results for CL1411.1−1148 and the analysis of our ALMA dataset. It is organised as follows. In Sect. 2 we present the sample selection and the observations with the Atacama Large Millimeter Array (ALMA). In Sect. 3, we present our results and make a comparison with the field population. We discuss our results in Sect. 4, and summarise our conclusions in Sect. 5. In the following we assume a flat ΛCDM cosmology with $\Omega_m = 0.3$, $\Omega_\Lambda = 0.7$ and $H_0 = 70$ km s^{-1} Mpc^{-1} (see Riess et al. 2019; Planck Collaboration 2020), and we use a Chabrier initial mass function (IMF) (Chabrier 2003). All magnitudes are in the AB system.

2. Sample and observations

EDisCS contains 18 systems at $0.4 < z < 0.8$ spanning the mass range from groups to massive clusters (velocity dispersions between ∼200 and 1200 km s^{-1}), each with ∼20 to 70 spectroscopically confirmed members (Halliday et al. 2004; Milvang-Jensen et al. 2008). Multi-band optical B, V, I, and R photometry and spectroscopy were obtained with VLT/FORS2 and J, and K_s bands gathered with the SOFI instrument on the NTT. *Spitzer* MIPS 24-micron observations were also obtained for a subset of clusters (Finn et al. 2010).

The Spatially Extended EDisCS survey (SEEDisCS) focuses on CL1301.7−1139 and CL1411.1−1148 at redshifts $z_{cl} = 0.4828$ and 0.5195 and velocity dispersions $\sigma_{cl} = 681$ and 710 km s^{-1}, respectively. Their intermediate masses make them close analogues to the progenitors of typical local clusters, whose velocity dispersions peak at around 500 km s^{-1} (Milvang-Jensen et al. 2008). Deep u, g, r, i, z and K_s images were taken with CFHT/MEGACAM and WIRCam. They cover a region that extends up to $\sim 10\times R_{200}$, with R_{200} corresponding to the cluster virial radius. Our observational strategy follows three main steps: ***i)*** identifying the LSS around the two clusters using accurate photometric redshifts (normalised median absolute deviation $\sigma_{NMAD} = 0.036$; Rerat et al. in prep.); ***ii)*** spectroscopically following up these LSS to characterise them precisely and to study the properties of the galaxy stellar populations; ***iii)*** using ALMA CO observations to reveal the status of the galaxy cold gas reservoirs.

2.1. Sample selection

Our ALMA targets were selected in the LSS around CL1411.1−1148 and using three criteria. First, targets were chosen to fall within three times the cluster velocity dispersion ($3\times\sigma_{cl}$), corresponding to a redshift interval $\Delta z = \pm 0.010$ around the cluster redshift. This is measured from the galaxy spectroscopic redshifts obtained with VLT/FORS2, VLT/VIMOS, or MMT/Hectospec, or from a robust redshift estimate from the IMACS Low Dispersion Prism (LDP). Second and with only one exception, the selected targets are located at a projected cluster centric distance smaller than $5\times R_{200}$. Third, the targets span the same range of stellar masses; u, g and i magnitudes; and colours from the combination of these bands as our initial comparison sample of normal star-forming field galaxies with CO information, the Plateau de Bure high-z Blue Sequence Survey 2 (PHIBSS2; Freundlich et al. 2019). This means that stellar masses were between $\log(M_{star}/M_\odot)$=10 and 11, $i \leq 22$, $g-i$ between ∼1 and 2.2, and $u-g$ between ∼0.6 and 1.5. Two galaxies from the original EDisCS spectroscopic sample were detected by *Spitzer* at 24 μm in the central $\sim 1.8 \times 1.8$ Mpc region of CL1411.1−1148 ($R_{200} = 1.27$ Mpc), above the 97 μJy 80% completeness flux limit of the EDisCS Spitzer observations (Finn et al. 2010). They are identified by a bold black circle in all figures.

Figure 1 shows the galaxy density map in the 1°×1° region centred on CL1411.1−1148. Densities are calculated within a photometric redshift slice of $\pm(1+z_{cl})\times\sigma_{NMAD} = 0.0547$ around the cluster redshift. Within this photometric redshift slice, we use a 'nearest neighbour' approach, in which for any point (x, y) the distance $r_N(x, y)$ to the Nth nearest neighbour is estimated. The galaxy density is thus the ratio between N (fixed) and the surface defined by the adaptive distance: $\rho_N(x, y) = \frac{N}{\pi r_N^2(x,y)}$. We chose $N = 10$, which corresponds to an average spatial scale (i.e. the mean distance between the ten galaxies) of about 0.8 Mpc, with 90% of the values being smaller than ∼1.5 Mpc. We selected 27 star-forming galaxies, satisfying the three criteria detailed above, and mapping the variety of local densities encountered inside and around the cluster as they appear from the photometric redshift estimates.

Figure 2 provides another 2D view of the spatial distribution of our ALMA targets over the same 1°×1° MEGACAM field of view. The galaxy positions are calculated relative to the position of the brightest cluster galaxy (BCG) in redshift and right ascension (RA). The galaxy relative position in redshift, Δd_{cl}, is computed by taking the difference between the comoving distances of the galaxy and the BCG. The relative position in RA, ΔRA, is obtained by transforming the angular separation between the BCG and the galaxy into a distance, using the angular distance at the redshift of the galaxy. Our full spectroscopic sample within $\pm 3\times\sigma_{cl}$ of z_{cl} is presented, as are the photometric redshift cluster

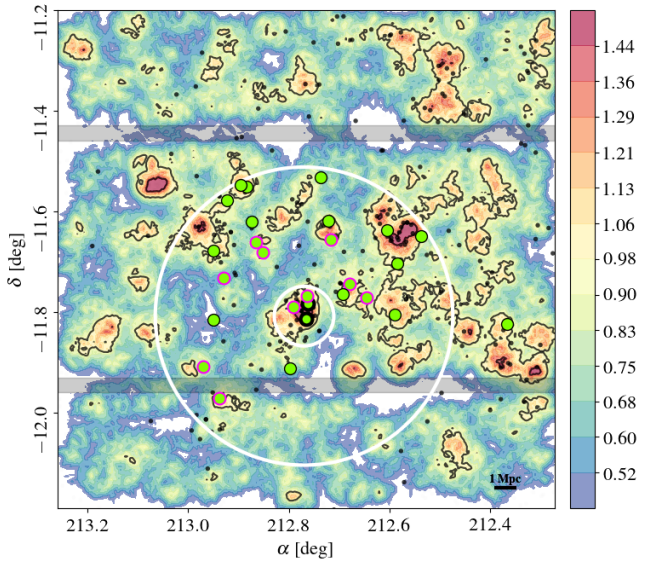

Fig. 1: Density map of the CFHT/MEGACAM 1°×1° field around CL1411.1−1148. The colour-coding indicates the $\log_{10}$ of the density of galaxies averaged over the ten nearest neighbours. Black contours are at 1 and 3σ above the field mean density. The grey points identify all galaxies with a $z_{\rm spec}$ within 5$\sigma_{\rm cl}$ of the cluster redshift. The inner and outer white circles are positioned at R_{200} and $5R_{200}$ radius, respectively. The grey bands indicate the gaps between the MEGACAM CCDs. The green circles show our ALMA targets. The thick black outline identifies the two cluster members detected at 24 μm by *Spitzer*. The pink outer rings show the position of the galaxies with low gas fraction (see Fig. 9 and Sect. 4.2).

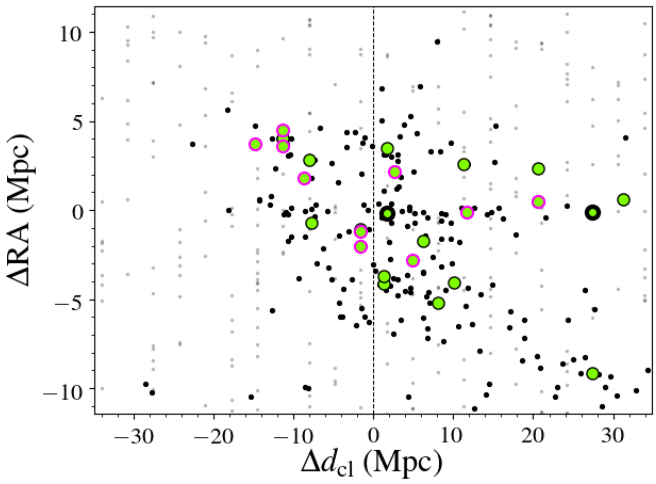

Fig. 2: Light cone centred on $z_{\rm cl}$ = 0.5195 and extending to ±3$\sigma_{\rm cl}$ in redshift. In right ascension, 1° is covered. The vertical line corresponds to the cluster redshift. The grey points indicate the galaxies with a photometric redshift. Galaxies with spectroscopic redshifts are in black. Our sample is in green, lower $\mu_{\rm H_2}$ galaxies (see Sect. 4.2) are outlined in pink, and *Spitzer* observed galaxies are outlined in thick black. Distances are expressed relative to the brightest cluster galaxy (BCG).

member candidates. The finger-of-God structure due to the relative velocities of the CL1411.1−1148 galaxies is clearly seen along the $\Delta d_{\rm cl}$-axis. Many of our targets are located in LSS related to CL1411.1−1148, such as the one extending westward from the cluster centre and up to 30 Mpc behind it; a few are in more isolated (lower density) regions. The information on our targets are summarised in Table 1.

PHIBSS2 encompasses 60 galaxies with CO(2-1) detections at $0.49 \leq z \leq 0.8$, with stellar masses ($M_{\rm star}$) higher than $10^{10.1}$ $M_\odot$ and SFRs above 3.5 $M_\odot yr^{-1}$ selected from the COSMOS, AEGIS and GOODS-North deep fields. A subsample of 19 systems falls at $0.49 \leq z \leq 0.6$ and is used as comparison sample for our study.

Figure 3 presents the distribution of the $0.49 \leq z \leq 0.6$ PHIBSS2 field galaxies and our ALMA sample in the $g-i$ versus i colour–magnitude diagram (CMD). The position of the red sequence of CL1411.1−1148 is derived by considering the initial galaxy sample of EDisCS in the centre of CL1411.1−1148, for which we have V- and I- as well as g- and i-band photometry. We first identify the passive galaxies in the (V, I) CMD from De Lucia et al. (2007). This provides us with their positions in the (g, i) plane and allows us to fit the corresponding mean locus of the red sequence, and place its ±0.3 mag dispersion.

The g- and i-band photometry for the PHIBSS2 galaxies comes from the original CFHT Legacy survey catalogue for the COSMOS and AEGIS fields (Erben et al. 2009), while they were derived from B, V, and I for the galaxies in the GOODS-North field from the 3D-HST catalogues (Capak et al. 2004). The latter may suffer from some uncertainties as no proper photometric calibration between these bands and g and i exists for galaxies.

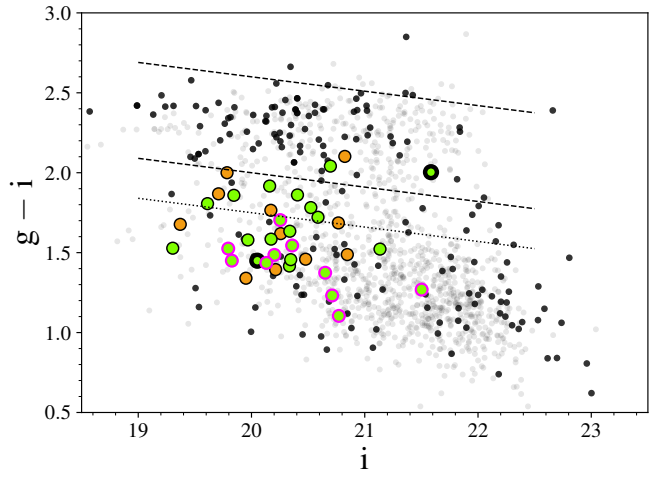

Fig. 3: Observed colour–magnitude diagram, $g-i$ as a function of i for the CL1411 galaxies. Our ALMA sample is in green. The dots with the thick black borders are our *Spitzer*-observed galaxies, and those with the pink borders are our low-$\mu_{\rm H_2}$ sample (see Sect. 4.3). The orange dots are the PHIBSS2 galaxies. The grey points are the photometric redshift members. The small black dots are the spectroscopic redshift galaxies, within 3$\sigma_{\rm cl}$ of the cluster redshift. The dashed lines delimit the red sequence and its ±0.3 mag dispersion. The dotted line delimits the transition zone between the blue clump and the red sequence, 0.25 mag below the lower boundary of the red sequence.

Figure 4 presents the rest-frame $U-V$ versus $V-J$ colour–colour diagram (CCD) that helps discriminate between passive

and star-forming galaxies (Williams et al. 2009). The rest-frame colours were derived with EAZY (Brammer et al. 2008). We used the Johnson-Cousins U and V bands, and the 2MASS J band (Skrutskie et al. 2006), together with a set of six templates: five main component templates obtained following the Blanton & Roweis (2007) algorithm and one for dusty galaxies (Brammer et al. 2008).

As expected, most of our targets fall in the star-forming region. Two systems, SEDCSJ1410249−1138157 and SEDCSJ1410518−1139195, are formally located within the passive region, however close to the boundary between the two regimes. None of them is located in the red sequence in Fig. 3, but rather in or close to the green valley, hence they are most likely transitioning to a quenched regime. On the other hand, the CO targets within the red sequences of the (g, i) CMD in Fig. 3 are not located in the passive region of the UVJ plane, meaning that they are dusty.

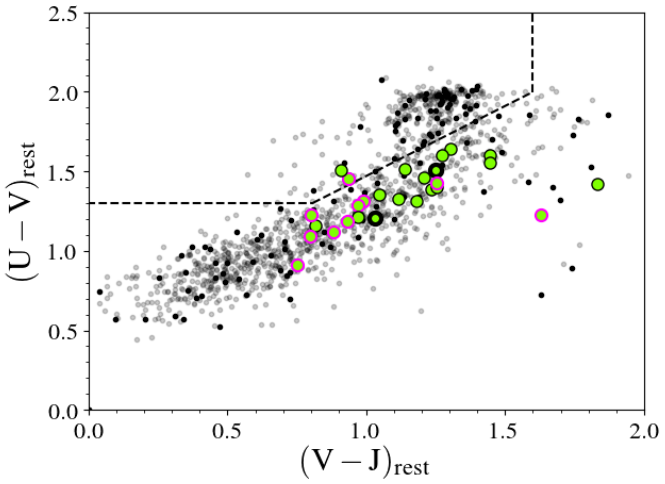

Fig. 4: Rest-frame UVJ colour–colour diagram. The dashed lines separate passive galaxies, in the upper part, from star-forming galaxies (Williams et al. 2009). Colours and symbols are the same as in Fig. 3

2.2. ALMA observations

Fluxes in the CO(3-2) line, falling at ∼226 GHz in the ALMA Band 6 for $z \sim 0.52$, were acquired during the ALMA Cycles 3 and 5 (programs 2015.1.01324.S, 2017.1.00257.S). The observations were conducted in the compact configurations C36−2 and C36−3, with 38 to 42 antennas, and C43−2, with 45 to 50 antennas, in Cycle 3 and 5, respectively. This led to beam sizes of 0.94″× 0.89″ and 1.2″× 0.95″ for Cycle 3 and 5, respectively. The integration times were of 7.5 hours (11 hours with overheads) in the 225.51–228.86 GHz spectral window. The resulting rms noise ranges from 0.09 to 0.25 mJy/beam in both cycles, and the spectral resolution is 50.7 km s^{-1} for Cycle 3 and between 10.3 and 41 km s^{-1} for Cycle 5, depending on the binning applied to reach sufficient signal-to-noise ratio.

A standard data reduction was performed with the CASA ALMA Science Pipeline (McMullin et al. 2007).The problematic antennas and runs were flagged. The continuum was fitted over the entire spectral window, except for the channels corresponding to the CO line, and subtracted. The final datacubes were created with the `tclean` routine using a Briggs weighting and a robustness parameter of 0.5, which is a trade-off between uniform and natural weighting. Finally we performed a primary beam correction, with the `impbcor` routine to obtain an astronomically correct image of the sky.

The final continuum-subtracted and primary-beam-corrected maps were exported to be analysed using GILDAS[1]. The i-band images of our targets, the CO maps and spectra are shown in Fig. A.1.

3. Derived parameters

3.1. CO flux and molecular gas mass

Fluxes, $S_{\rm CO}\,\Delta V$, were obtained by selecting the velocity window centred on the peak emission and maximising the flux over it and the spatial extent of the source.

Following Lamperti et al. (2020), the error on the flux is defined as

$$\epsilon_{\rm CO} = \frac{\sigma_{\rm CO}\Delta V}{\sqrt{\Delta V \Delta w_{ch}^{-1}}}, \tag{1}$$

where $\sigma_{\rm CO}$ is the rms noise (in Jy) calculated in units of spectral resolution Δw_{ch}, and ΔV (in km s^{-1}) is the width of the spectral window in which the line flux is calculated, $\Delta w_{ch} = 50.7$ km s^{-1} for Cycle 3 and $\Delta w_{ch} = \{10.3; 20.6; 41\}$ km s^{-1}, depending on the binning applied to the spectrum, for Cycle 5. All intensity maps and integrated spectra are shown in Fig A.1 of the Appendix. A few of our targets show double-peaked emission lines, which is an indication of rotation. This will be analysed in a forthcoming paper.

The intrinsic CO luminosity associated with a transition between the levels J and $J-1$ is expressed as

$$L'_{\rm CO(J\to J-1)} = 3.25\times10^7 S_{\rm CO(J\to J-1)}\Delta V\, \nu_{\rm obs}^{-2}\, D_{\rm L}^2\,(1+z)^{-3}, \tag{2}$$

where $L'_{\rm CO(J\to J-1)}$ is the line luminosity expressed in units of K km s^{-1}pc^2; $S_{\rm CO(J\to J-1)}\Delta V$ is the velocity-integrated flux in Jy km s^{-1}; $\nu_{\rm obs}$ is the observed frequency in GHz; $D_{\rm L}$ is the luminosity distance in Mpc; and z is the redshift of the observed galaxy (Solomon et al. 1997; Solomon & Vanden Bout 2005).

The total cold molecular gas mass ($M_{\rm H_2}$) is then estimated as

$$M_{\rm H_2} = \alpha_{\rm CO}\frac{L'_{\rm CO(J\to J-1)}}{r_{J1}}, \tag{3}$$

where $\alpha_{\rm CO}$ is the CO(1-0) luminosity-to-molecular-gas-mass conversion factor, considering a 36% correction to account for interstellar helium, and $r_{J1} = L'_{\rm CO(J\to J-1)}/L'_{\rm CO(1-0)}$ the corresponding line luminosity ratio.

The $\alpha_{\rm CO}$ factor depends on different parameters: the average cloud density, the Rayleigh-Jeans brightness temperature of the CO transition, and the metallicity of the giant molecular clouds (GMCs) of the galaxy (Leroy et al. 2011; Genzel et al. 2012; Bolatto et al. 2013; Sandstrom et al. 2013). In the Milky Way, in nearby main-sequence (MS) star-forming galaxies, and in low-metallicity galaxies different methods are used to estimate this conversion factor. They converge to $\alpha_{\rm CO} = 4.36 \pm 0.9\, M_\odot\,(\mathrm{K\,km\,s^{-1}\,pc^2})^{-1}$, including the correction for helium, as a good estimate for normal star-forming galaxies (Dame et al. 2001; Grenier et al. 2005; Abdo et al. 2010; Leroy et al. 2011; Bolatto et al. 2013; Carleton et al. 2017).

[1] http://www.iram.fr/IRAMFR/GILDAS

Table 1: Sample properties: Galaxy ID, coordinates, optical spectroscopic redshift, and SED-based estimates of the galaxy M_{star} and SFRs

IDs	R.A. (J2000)	Dec (J2000)	z_{spec}	M_{star} (10^{10} $M_\odot$)	SFR_{SED} ($M_\odot$ yr^{-1})
SEDCSJ1409277−1149267	14:09:27.7553	−11:49:26.734	0.5275	$7.08^{+1.47}_{-1.47}$	$19.14^{+10.58}_{-11.90}$
SEDCSJ1410089−1138578	14:10:08.9192	−11:38:57.846	0.5217	$2.95^{+0.61}_{-0.68}$	$5.09^{+3.81}_{-3.52}$
SEDCSJ1410204−1142155	14:10:20.3750	−11:42:15.477	0.5199	$14.13^{+2.93}_{-3.58}$	$10.52^{+2.18}_{-7.63}$
SEDCSJ1410214−1148167	14:10:21.4016	−11:48:16.687	0.5226	$12.02^{+2.49}_{-2.21}$	$18.92^{+3.92}_{-9.59}$
SEDCSJ1410249−1138157	14:10:24.9817	−11:38:15.703	0.5199	$5.62^{+1.68}_{-2.07}$	$3.82^{+1.14}_{-2.99}$
SEDCSJ1410349−1146140†	14:10:34.9274	−11:46:14.071	0.5210	$3.09^{+0.64}_{-0.64}$	$5.71^{+2.70}_{-2.89}$
SEDCSJ1410429−1144385†	14:10:42.8737	−11:44:38.509	0.5308	$5.89^{+1.08}_{-1.08}$	$9.82^{+5.99}_{-4.18}$
SEDCSJ1410463−1145508	14:10:46.3146	−11:45:50.845	0.5214	$13.8^{+3.18}_{-2.22}$	$44.87^{+10.33}_{-40.30}$
SEDCSJ1410518−1139195†	14:10:51.8133	−11:39:19.548	0.5185	$4.9^{+0.79}_{-0.90}$	$3.33^{+1.65}_{-1.57}$
SEDCSJ1410532−1137091	14:10:53.2482	−11:37:09.091	0.5193	$4.68^{+0.97}_{-0.86}$	$15.38^{+10.63}_{-11.16}$
SEDCSJ1410568−1131594	14:10:56.8242	−11:31:59.398	0.5171	$5.5^{+1.64}_{-1.52}$	$6.27^{+1.88}_{-3.68}$
EDCSNJ1411028−1147006⋆	14:11:02.8248	−11:47:01.302	0.5202	$4.79^{+1.10}_{-0.99}$	$15.92^{+6.60}_{-7.88}$
SEDCSJ1411033−1146028†	14:11:03.2799	−11:46:02.789	0.5231	$1.82^{+0.50}_{-0.42}$	$4.59^{+1.27}_{-2.27}$
EDCSNJ1411036−1148506⋆	14:11:03.5909	−11:48:50.573	0.5282	$2.29^{+0.63}_{-0.58}$	$5.58^{+3.41}_{-3.28}$
SEDCSJ1411096−1147245†	14:11:09.6219	−11:47:24.523	0.5002[a]	$0.74^{+0.22}_{-0.21}$	$2.86^{+0.84}_{-1.42}$
SEDCSJ1411112−1154452	14:11:11.2342	−11:54:45.236	0.5292	$10.72^{+2.22}_{-2.22}$	$16.29^{+3.38}_{-11.82}$
SEDCSJ1411243−1140510†	14:11:24.3255	−11:40:51.064	0.5171	$1.15^{+0.32}_{-0.27}$	$5.71^{+1.58}_{-1.84}$
SEDCSJ1411275−1139433†	14:11:27.5630	−11:39:43.290	0.5203	$3.39^{+0.70}_{-0.70}$	$10.89^{+2.26}_{-4.51}$
SEDCSJ1411296−1137130	14:11:29.6609	−11:37:13.061	0.5259	$5.5^{+1.39}_{-1.64}$	$4.65^{+1.18}_{-4.22}$
SEDCSJ1411319−1133048	14:11:31.9412	−11:33:04.781	0.5231	$3.31^{+0.76}_{-0.61}$	$7.62^{+4.30}_{-3.33}$
SEDCSJ1411348−1132522	14:11:34.7740	−11:32:52.216	0.5172	$4.9^{+1.01}_{-0.90}$	$8.85^{+8.66}_{-7.54}$
SEDCSJ1411416−1134421	14:11:41.6397	−11:34:42.092	0.5198	$5.13^{+0.94}_{-1.06}$	$7.53^{+4.94}_{-3.56}$
SEDCSJ1411431−1143589†	14:11:43.0675	−11:43:58.969	0.5156	$1.82^{+0.42}_{-0.34}$	$6.19^{+1.43}_{-2.71}$
SEDCSJ1411449−1158184†	14:11:44.9883	−11:58:18.447	0.5149	$5.75^{+1.59}_{-1.72}$	$12.79^{+3.54}_{-7.51}$
SEDCSJ1411478−1140389	14:11:47.7871	−11:40:38.956	0.5159	$2.51^{+0.46}_{-0.35}$	$10.64^{+10.78}_{-6.98}$
SEDCSJ1411480−1148562	14:11:47.9664	−11:48:56.199	0.5156	$11.22^{+2.07}_{-2.33}$	$9.38^{+8.1}_{-5.5}$
SEDCSJ1411528−1154286†	14:11:52.8004	−11:54:28.643	0.5160	$3.63^{+0.75}_{-0.67}$	$6.12^{+4.23}_{-2.96}$

Notes. Central galaxies detected by *Spitzer* are indicated with⋆. Galaxies with low μ_{H_2} are identified with †. [(a)] Galaxy with z_{LDP} as z_{spec}.

The values of r_{31} have been measured in a number of ways in nearby galaxies, and range from ∼ 0.2 to 2 (rarely reached however) (Mauersberger et al. 1999; Mao et al. 2010; Wilson et al. 2012). Dumke et al. (2001) found that r_{31} could vary within a galaxy from r_{31} ∼ 0.8 in the bulge to r_{31} ∼ 0.4 in the disk for local galaxies without enhanced star formation. More recently Lamperti et al. (2020) identified a trend of r_{31} with star formation efficiency, from ∼ 0.2 to 1.2 (with a mean value around 0.5), and inferred from modelling that the gas density is the main parameter responsible for this variation. At intermediate (z ∼ 0.5) and high redshifts (z ∼ 1.5), several studies assumed $r_{31} = 0.5 \pm 0.05$, as we do here as a fair compromise between all studies (Bauermeister et al. 2013b; Genzel et al. 2015; Chapman et al. 2015; Carleton et al. 2017; Tacconi et al. 2018). We discuss the impact of the choice of α_{CO} and r_{31} on the cold molecular gas masses of our galaxies in Sect. 4.4.

The full widths at half maximum (FWHMs) are derived from single or double Gaussian fits of the CO emission lines. We obtain a median FWHM of 224 km s^{-1} with a standard deviation of 101 km s^{-1} for our entire ALMA sample, similarly to what is found for our range of stellar masses by Freundlich et al. (2019).

The intrinsic CO(3-2) luminosity $L'_{CO(3-2)}$, the line FWHM, the cold molecular gas mass M_{H_2}, the corresponding gas-to-stellar-mass ratio $\mu_{H_2} = M_{H_2}/M_{star}$, and the redshift of the CO emission of our sample galaxies are listed in Table 2. One galaxy, SEDCSJ1411096−1147245, exhibits a large difference between its optical and CO redshifts. This is due to its optical redshift being estimated from IMACS-LDP, with a precision $\sigma_z = 0.007$ (Just et al. 2015). SEDCSJ1411096−1147245 was not in our initial list of targets for ALMA. It turned out that while our primary target was not detected (SEDCSJ1411098−1147242 at $z_{spec} = 0.5260$), its companion galaxy within 3″, SEDCSJ1411096−1147245 was. This is shown in Fig. A.1 in the *i*-band image; the original target is shown on the left.

3.2. Stellar masses and star formation rates

The stellar masses and SFRs were derived with MAGPHYS[2] (da Cunha et al. 2008) using the *u*, *g*, *r*, *i*, *z*, and *Ks* bands, as well as the 24 μm flux when available. The stellar populations and dust extinction models are those of Bruzual & Charlot (2003) and Charlot & Fall (2000). MAGPHYS provides probability density functions (PDFs) for each parameter (i.e. SFR, M_{star}, dust mass, dust temperature). For each quantity, we considered the peak value of the PDFs and our uncertainties cor-

[2] http://www.iap.fr/magphys/index.html

Table 2: CO redshift, line-integrated flux, line width, luminosity of the CO(3-2) emission, cold molecular gas masses and cold molecular gas-to-stellar mass ratios of the ALMA targets.

IDs	z_{CO}	$S_{CO(3-2)}\Delta V$ (Jy km s^{-1})	FWHM (km s^{-1})	$L'_{CO(3-2)}$ (10^8 L$_\odot$)	M_{H_2} (10^9 M$_\odot$)	μ_{H_2}
SEDCSJ1409277−1149267	0.5287	0.943 ± 0.052	568 ± 45	15.36 ± 0.853	13.39 ± 3.16	$0.189^{+0.084}_{-0.084}$
SEDCSJ1410089−1138578	0.5227	0.494 ± 0.029	236 ± 19	7.859 ± 0.457	6.85 ± 1.62	$0.232^{+0.103}_{-0.108}$
SEDCSJ1410204−1142155	0.5200	0.655 ± 0.021	110 ± 45	10.326 ± 0.329	9.0 ± 2.09	$0.064^{+0.028}_{-0.031}$
SEDCSJ1410214−1148167	0.5226	0.500 ± 0.008	93 ± 2	7.966 ± 0.132	6.95 ± 1.6	$0.058^{+0.025}_{-0.024}$
SEDCSJ1410249−1138157	0.5199	0.327 ± 0.015	262 ± 10	5.154 ± 0.243	4.49 ± 1.05	$0.08^{+0.043}_{-0.048}$
SEDCSJ1410349−1146140†	0.5213	0.164 ± 0.014	224 ± 21	2.597 ± 0.225	2.26 ± 0.56	$0.073^{+0.033}_{-0.033}$
SEDCSJ1410429−1144385†	0.5220	0.214 ± 0.018	118 ± 20	3.374 ± 0.288	2.94 ± 0.72	$0.050^{+0.021}_{-0.021}$
SEDCSJ1410463−1145508	0.5215	2.150 ± 0.010	206 ± 2	34.094 ± 0.199	29.73 ± 6.82	$0.215^{+0.099}_{-0.084}$
SEDCSJ1410518−1139195†	0.5193	0.175 ± 0.025	166 ± 31	2.750 ± 0.400	2.4 ± 0.65	$0.049^{+0.021}_{-0.022}$
SEDCSJ1410532−1137091	0.5213	1.398 ± 0.038	404 ± 12	22.03 ± 0.596	19.21 ± 4.44	$0.411^{+0.18}_{-0.17}$
SEDCSJ1410568−1131594	0.5172	0.483 ± 0.014	273 ± 9	7.53 ± 0.225	6.57 ± 1.52	$0.119^{+0.063}_{-0.061}$
EDCSNJ1411028−1147006	0.5207	0.884 ± 0.020	148 ± 6	13.95 ± 0.325	12.17 ± 2.80	$0.254^{+0.117}_{-0.111}$
SEDCSJ1411033−1146028†	0.5231	0.108 ± 0.010	243 ± 22	1.724 ± 0.155	1.5 ± 0.37	$0.083^{+0.043}_{-0.039}$
EDCSNJ1411036−1148506	0.5287	0.436 ± 0.049	148 ± 13	7.102 ± 0.799	6.19 ± 1.58	$0.270^{+0.144}_{-0.138}$
SEDCSJ1411096−1147245†	0.5259[a]	0.144 ± 0.017	272 ± 72	2.306 ± 0.278	2.01 ± 0.52	$0.270^{+0.150}_{-0.145}$
SEDCSJ1411112−1154452	0.5292	0.602 ± 0.014	183 ± 11	9.843 ± 0.237	8.58 ± 1.98	$0.080^{+0.035}_{-0.035}$
SEDCSJ1411243−1140510†	0.5168	0.106 ± 0.006	183 ± 14	1.65 ± 0.098	1.44 ± 0.34	$0.125^{+0.064}_{-0.059}$
SEDCSJ1411275−1139433†	0.5203	0.154 ± 0.006	127 ± 5	2.431 ± 0.101	2.12 ± 0.49	$0.063^{+0.028}_{-0.028}$
SEDCSJ1411296−1137130	0.5259	0.411 ± 0.016	243 ± 27	6.634 ± 0.255	5.78 ± 1.35	$0.105^{+0.051}_{-0.056}$
SEDCSJ1411319−1133048	0.5233	0.736 ± 0.024	266 ± 13	11.75 ± 0.390	10.25 ± 2.37	$0.309^{+0.143}_{-0.129}$
SEDCSJ1411348−1132522	0.5173	0.645 ± 0.034	306 ± 27	10.05 ± 0.525	8.77 ± 2.06	$0.179^{+0.079}_{-0.075}$
SEDCSJ1411416−1134421	0.5200	0.759 ± 0.027	163 ± 6	11.97 ± 0.424	10.44 ± 2.42	$0.203^{+0.085}_{-0.089}$
SEDCSJ1411431−1143589†	0.5166	0.198 ± 0.008	124 ± 8	3.075 ± 0.124	2.68 ± 0.62	$0.147^{+0.068}_{-0.061}$
SEDCSJ1411449−1158184†	0.5149	0.259 ± 0.012	361 ± 17	4.002 ± 0.189	3.49 ± 0.82	$0.061^{+0.031}_{-0.032}$
SEDCSJ1411478−1140389	0.5160	0.450 ± 0.020	259 ± 29	6.984 ± 0.312	6.09 ± 1.42	$0.242^{+0.101}_{-0.090}$
SEDCSJ1411480−1148562	0.5160	0.388 ± 0.024	265 ± 34	6.021 ± 0.378	5.25 ± 1.25	$0.047^{+0.020}_{-0.021}$
SEDCSJ1411528−1154286†	0.5166	0.102 ± 0.023	166 ± 58	1.584 ± 0.362	1.38 ± 0.45	$0.038^{+0.020}_{-0.019}$

Notes. Galaxies with low μ_{H_2} are identified with †. [(a)] Galaxy with z_{LDP} as z_{spec}.

respond to the 68% confidence interval of the same PDFs. The wavelength coverage of our photometric bands does not allow the identification of AGNs, which could affect the SFR and M_{star} estimates. However, the analysis of the [OII]-to-Hβ line ratio indicates that most likely the emission lines in our galaxy spectra are not typical of AGNs (Sánchez-Blázquez et al. 2009). This adds to our current understanding that there is a smaller percentage of AGNs in clusters (less than 3%) than in the field (Miller et al. 2003; Kauffmann et al. 2004; Mishra & Dai 2020).

We used the two galaxies in the core of CL1411.1−1148 which were detected by *Spitzer* at 24 μm to evaluate the robustness of our stellar mass and SFR estimates. The 24 μm flux (corresponding to ∼15μm at $z \sim 0.52$) allows us to better constrain the dust emission and judge its impact on the derived quantities. Figure 5 presents the spectral energy distribution (SED) fits and the corresponding likelihood distribution of M_{star} and SFR for EDCSNJ1411028−1147006 and EDCSNJ1411036−1148506. For both galaxies, M_{star} stays identical with or without the 24 μm flux. As to the SFR, the PDFs of EDCSNJ1411028−1147006 are essentially identical with or without the 24 μm flux point. The case of EDCSNJ1411036−1148506 is different. Its SFR PDF is wider without the 24 μm flux point (peak value at log(SFR) = 0.5) than when calculated with the 24 μm point (peak value at log(SFR) = 0.8). The two PDFs have medians within 0.3 dex and are highly overlapping, hence the SFR estimates are consistent with each other. EDCSNJ1411036−1148506 is the faintest galaxy in our sample in the *i* band (> 21.5, Fig. 3) and is probably observed edge-on, as seen in Fig. A.1. Its UV flux is very low, with the deepest rest-frame 4000 Å break, hence representing the most challenging and dusty case in our sample.

In summary, our stellar mass estimates are robustly derived from *u* to K_s photometry. As for the SFRs, missing the *Spitzer* 24 μm flux could lead to underestimated values, but our error bars are realistic enough to take this possibility into account.

Figure 6 presents the position of our sample galaxies relative to the MS of normal star-forming galaxies at the same redshift (Speagle et al. 2014), corrected for a Chabrier IMF. Our spectroscopic and photometric datasets are both displayed. More than three-quarters (78%) of our ALMA targets fall within the ± 0.3 dex dispersion of the MS. Three of our ALMA targets are located just below the −0.3 dex limit; however, they are still compatible with the MS considering the uncertainties on the SFRs. Three systems fall in between the MS and the red sequence. These are systems in the transition region between star-forming and passive systems. Mancini et al. (2019) show that this region of the stellar mass–SFR plane contains galaxies that are quenching, but also galaxies that are undergoing a rejuvenation of star

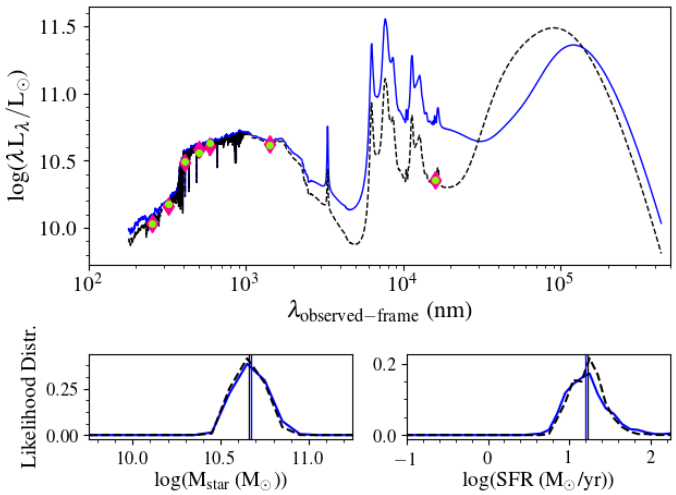

(a) EDCSNJ1411028−1147006.

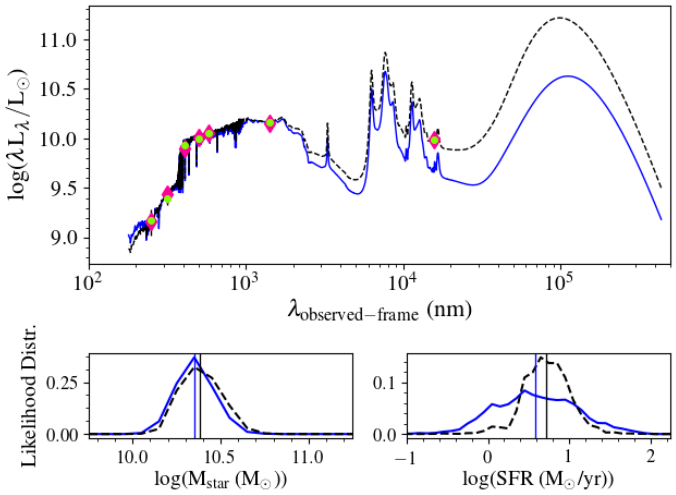

(b) EDCSNJ1411036−1148506.

Fig. 5: SEDs and likelihood distributions for the two *Spitzer*-observed galaxies: EDCSNJ1411028−1147006 (a) and EDCSNJ1411036−1148506 (b). The blue curves are without the MIPS 24 μm fluxes and the black dashed curves are with the MIPS 24 μm fluxes. The top panels show the fitted SEDs in black and blue, the observed fluxes in green, and the model fluxes in pink. The bottom panels of (a) and (b) show the likelihood distributions for M_{star} and SFR, and the medians for the M_{star} and SFR, as the blue and black vertical lines, derived with MAGPHYS.

formation. With the exception of three PHIBSS2 galaxies, which stand clearly above the MS, PHIBSS2 $z \sim 0.55$ systems and our ALMA targets cover the same SFR–M_{star} space. Their cold gas reservoirs can therefore be compared.

4. Discussion

4.1. Comparison sample

To place our results in a global context, our datasets are compared to the other CO-line observations available to date. They are listed below in order of increasing redshift.

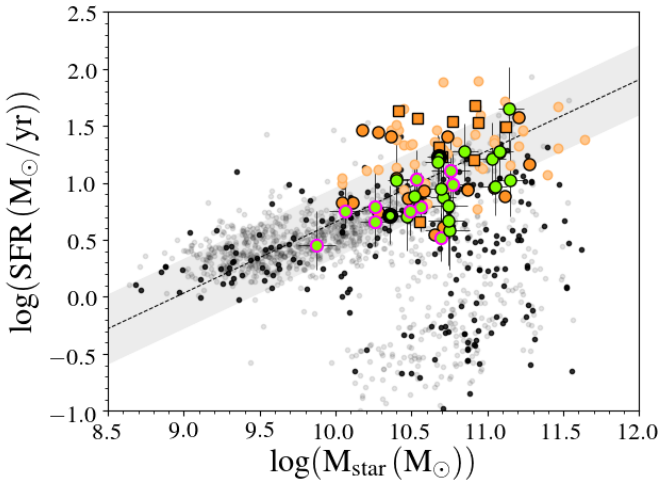

Fig. 6: Location of the CL1411 (grey) and ALMA (green) galaxies in the stellar mass–SFR plane. The dots with thick black borders represent the *Spitzer*-observed galaxies and those with the pink outline indicate the low-μ_{H_2} galaxies. Galaxies in black and grey are the rest of the spectroscopic and photometric samples, respectively, at the cluster redshift. The plain orange circles are the PHIBSS2 galaxies with $0.49 \leq z \leq 0.6$, while the light orange circles trace the PHIBSS2 sample at $0.6 < z \leq 0.8$; the orange squares show the cluster LIRGs of Castignani et al. (2020) at $z \sim 0.54$. The dashed black line is the Speagle et al. (2014) MS corrected for a Chabrier IMF, at our cluster redshift with the corresponding ±0.3dex scatter as the grey shaded area.

1. 53 detections of CO(1-0) for local ($0.001 < z < 0.05$) IR luminous galaxies (Gao & Solomon 2004);
2. 19 detections of CO(1-0) for LIRGs with $z \sim 0.01$ (García-Burillo et al. 2012);
3. 333 detections of CO(1-0) for galaxies from xCOLD GASS (Saintonge et al. 2017) with $M_{star} > 10^{10} M_\odot$ and z between 0.01 and 0.05;
4. 46 detections of CO(3-2) for galaxies selected from the BASS survey (Baumgartner et al. 2013) with $z < 0.04$ and studied in Lamperti et al. (2020);
5. 27 detections of CO(1-0) and CO(3-2) for star-forming galaxies with z from 0.06 to 0.3 from the EGNoG survey (Bauermeister et al. 2013a,b);
6. 8 detections of CO(1-0) emission for galaxies selected based on their 4000 Å emission strength with redshifts from 0.1 to 0.23 (Morokuma-Matsui et al. 2015);
7. 9 detections of CO(1-0) for star-forming galaxies inside and in the foreground and background of two Abell clusters, A2192 and A963, with z between 0.13 and 0.23, from the COOL BUDHIES survey (Cybulski et al. 2016);
8. 8 CO(1-0) and 12 CO(2-1) observations of LIRGs inside clusters with redshift between 0.21 and 0.56 (Castignani et al. 2020);
9. 2 CO(2-1) and 1 CO(1-0) detections of LIRGS inside two clusters at $z = 0.397$ and 0.489 (Jablonka et al. 2013);
10. 5 CO(1-0) detections from 24μm-selected galaxies at $z = 0.4$ (Geach et al. 2009, 2011);
11. 46 detections of CO(2-1) for star-forming galaxies with $0.5 \leq z \leq 0.8$, as part of the PHIBSS2 survey (Tacconi et al. 2018; Freundlich et al. 2019);
12. 4 CO(2-1) detections for massive and passive galaxies from the LEGA-C survey with $0.6 \leq z \leq 0.73$ (Spilker et al. 2018);

13. 52 detections of CO(3-2) for star-forming galaxies with redshifts ranging from 1 to 2.3, as part of the PHIBSS1 survey (Tacconi et al. 2010, 2013);
14. 17 CO(2-1) detections of main-sequence galaxies inside the XMMXCS J2215.9−1738 cluster at $z = 1.46$ (Hayashi et al. 2018);
15. 5 detections of CO(2-1) for near-IR selected galaxies at $z \sim 1.5$ from Daddi et al. (2010);
16. 11 detections of CO(2-1) emission for cluster galaxies at $z \sim 1.6$ from Noble et al. (2017, 2019);
17. 2 detections of CO(1-0) emission of massive cluster galaxies at $z \sim 1.62$ from Rudnick et al. (2017)

It is noteworthy that most of these datasets are made of field galaxies, with the exception of Geach et al. (2009, 2011), Jablonka et al. (2013), Cybulski et al. (2016), Noble et al. (2017, 2019) and Castignani et al. (2020). Depending on the focus of the discussions below, we include all or only parts of this comparison sample. The PHIBSS2 galaxies at $0.49 \leq z \leq 0.60$ are the best field counterparts to our study in terms of redshift range, and even more importantly because most of the galaxies are forming stars at a normal rate for their stellar masses. The ten galaxies of the MACS J0717.5+3745 cluster observed by Castignani et al. (2020) are, in redshift, the closest cluster galaxy counterparts to our study. However, they were selected differently, specifically as LIRGs, and consequently probe on average higher specific SFRs (sSFR = SFR/M_{star}) than our sample, and do not extend down to the lowest values as our sample does, as can be seen in Fig. 7. The three field PHIBSS2 galaxies with the highest gas fraction are systems very clearly above the MS, hence they do not have counterparts in our dataset. They are nonetheless included in our analysis.

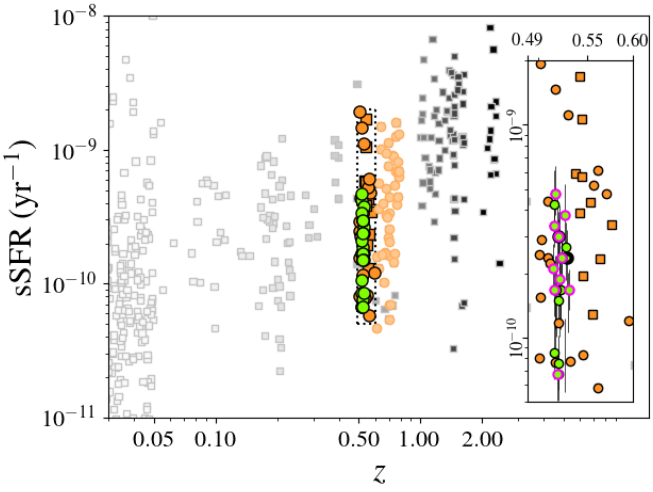

Fig. 7: Specific star formation rates as a function of redshift. The green dots identify our ALMA targets; dots with the thick black borders are the galaxies detected at 24 μm, and dots with the pink outlines galaxies with low gas fraction. The orange circles stand for the PHIBSS2 galaxies, with the darker shade for the systems at $0.49 \leq z \leq 0.6$ and the lighter for the galaxies at $0.6 < z \leq 0.8$. The orange squares indicate the M0717 LIRGs. The symbols in shades of grey are for the samples we pulled from the literature at different redshifts. We provide a zoom-in of the region delineated by the dotted lines (see inset), around the redshift of CL1411.1−1148. While three of the PHIBSS2 sources have sSFRs well above those of our ALMA targets, the sSFRs of the rest of the PHIBSS2 sources are in perfect agreement with those from our sample.

4.2. Gas fractions

Figure 8 shows the variation of the galaxy gas fraction, $\mu_{H_2} = M_{H_2}/M_{star}$, with redshift for both our targets and other CO-line measurements published to date. Our sample is the largest sample of galaxies with direct cold gas measurements at a single intermediate redshift ($0.5000 < z < 0.5375$) and the only one with galaxies in interconnected cosmic structures around a given galaxy cluster. The cluster galaxy sample of Castignani et al. (2020) at $z \sim 0.54$ extends to ~ 1.6 times the virial radius of M0717, hence stays closer to the cluster centre than the present study.

We probe a wide range of μ_{H_2} values, from ~0.04 to 0.30; 44% of our galaxies have μ_{H_2} lower than 0.1. This contrasts with the bulk of other datasets at $z > 0.05$. Of these, only the PHIBSS2 sample at $0.49 \leq z \leq 0.8$ has gas fractions that are as low as ours, and even then only ~ 20% of the coeval PHIBSS2 galaxies have μ_{H_2} below 0.1. The low gas fractions we see in our sample compared to those in the field cannot simply be due to cosmic evolution in μ_{H_2}, as samples at both lower and higher redshift have increased gas fractions. It is more likely linked to how we selected our galaxies as many early CO studies that dominate the literature values tended to select LIRGs rather than normal star-forming galaxies. This could impact the derivation of the scaling relations using different studies covering a wide range of redshifts (e.g. Tacconi et al. 2018).

Figure 9 presents the galaxy cold gas fractions as a function of their stellar masses. It constitutes the main result of our analysis. At redshifts similar to those of our sample, $0.49 \leq z \leq 0.6$, the relation between μ_{H_2} and M_{star} for the PHIBSS2 subsample has a slope of ~ -0.82 and a variance $\sigma_{H_2} = 0.37$ dex. A

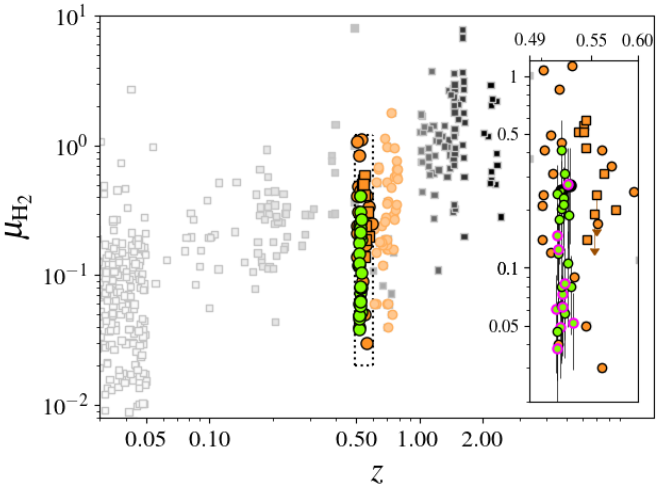

Fig. 8: Molecular gas-to-stellar mass ratio as a function of redshift. The colour-coding is as in Fig. 7. We provide a zoom-in of the region delineated by the dotted lines (see inset), around the redshift of CL1411.1−1148.

significant fraction of our targets fall below this $1 \times \sigma_{H_2}$ line of the M_{star}–μ_{H_2} relation for the field galaxies. This means that while 63% of the galaxies in the LSS of CL1411.1−1148 have gas mass fractions comparable to their field counterparts, 37% lie below the locus defined by field galaxies at the same stellar mass. We refer to these ten galaxies as low-μ_{H_2} systems. In or-

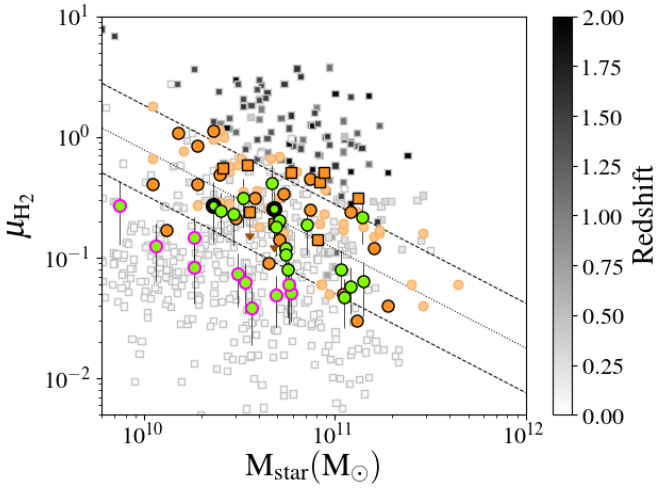

Fig. 9: Fraction of cold molecular gas as a function of the galaxy stellar masses. The colours and shapes of the symbols are the same as in Fig. 7. The dotted line is the fit of the M_{star}–μ_{H_2} relation for the PHIBSS2 galaxies at $0.49 < z \leq 0.6$, with its variance being represented by the two dashed lines. The pink outlined green symbols are for our low-μ_{H_2} galaxies, which are located below the $1\times\ \sigma_{H_2}$ line of the M_{star}–μ_{H_2} relation for the PHIBSS2 field galaxies.

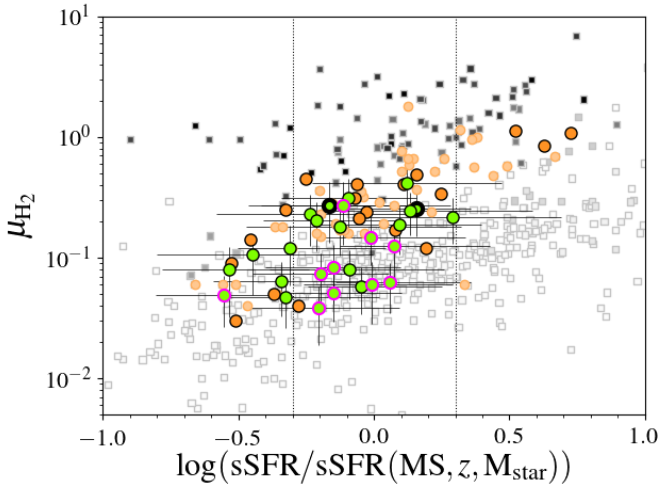

Fig. 10: Fraction of cold molecular gas as a function of the normalised specific star formation rates. The colours and shapes of the symbols are the same as in Fig. 7. The dotted lines represent the ±0.3 dex scatter of the MS.

der to quantify the significance of this low-μ_{H_2} population, we randomly extracted, 100 000 times, 27 galaxies from a normal distribution of sources with the same mean μ_{H_2} and same standard deviation as PHIBSS2. The probability of getting 37% of the galaxies below 1σ is less than 1%. Therefore, this excess to one side of the field relation deviates significantly from the expected tail of sources for a Gaussian distribution, and reveals a population that was absent from previous surveys. These galaxies are identified with the dagger symbol (†) in the tables and they are highlighted in pink in all figures. Combining our sample with the comparison field PHIBSS2 subsample with $z \leq 0.6$, the relation between μ_{H_2} and M_{star} becomes slightly shallower, with a slope of −0.51.

Interestingly, the SFRs of all but one (SEDCSJ1410518−1139195) of the low-μ_{H_2} galaxies are normal for their stellar masses, indicating that their molecular gas reservoir, either in mass or in physical properties, is modified before their star formation activity is impacted. This possibility was also suggested by Jablonka et al. (2013) for LIRGs in clusters and by Alatalo et al. (2015) for local elliptical galaxies, who find that their diffuse gas reservoir could potentially be stripped before the dense gas, which is more closely related to star formation. This disconnection between μ_{H_2} and SFR is further illustrated in Fig. 10 which presents μ_{H_2} as a function of the galaxy sSFR, normalised to their position on the MS, following Genzel et al. (2015).

Although our galaxies have normal SFRs for their stellar masses, they have a significantly different distribution of gas fractions than the field samples. Our low-μ_{H_2} targets populate a region that to date has remained uncovered at similar redshift, and reveal that there is a much larger scatter in μ_{H_2} at fixed sSFR (nearly twice as much) than previously encountered in other studies at similar redshifts. To quantify this result, we performed an Anderson–Darling (A-D) test (Scholz & Stephens 1987) between the μ_{H_2} distributions of PHIBSS2 galaxies and ALMA targets, both within the MS. The A-D test is more sensitive to differences in the tails of the distributions than a Kolmogorov–Smirnov test. When all MS galaxies are considered, the A-D test results in p = 0.027, meaning that there is only a 2.7% chance that the two samples come from the same distribution in μ_{H_2}. When we restrict the comparison to the low-μ_{H_2} MS galaxies only and the full MS PHIBSS2 galaxies, we find $p = 1.3 \times 10^{-3}$, which clearly shows that this low-μ_{H_2} tail of the ALMA sample comes from a significantly different μ_{H_2} distribution (>99%) from that of the PHIBSS2 MS galaxies.

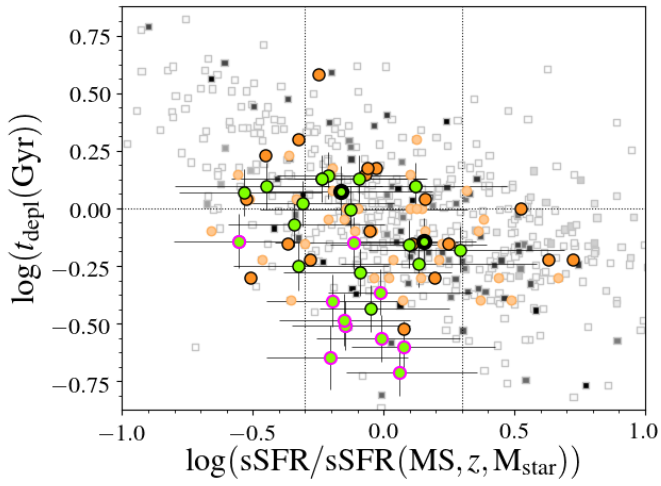

Fig. 11: Dependence of the depletion timescale (in Gyr) as a function of the normalised specific star formation rates. The colours and shapes of the markers are the same as in Fig. 7. The horizontal dotted line is located at 1 Gyr and the vertical dotted lines represent the ± 0.3 dex scatter of the MS.

Figure 11 shows the depletion timescales (M_{gas}/SFR) as a function of the normalised sSFR. Our low-μ_{H_2} galaxies have short depletion times ∼ 300 Myr compared to the bulk of the population known so far. This implies that they should consume their gas and quench more rapidly.

4.3. Link with local density

As a first attempt to link the spatial location of our sample galaxies and their gas masses, we searched for a possible correlations between the galaxy gas fraction and cluster-centric distance, but did not find any.

We then looked into the possibility that low gas fractions correlate with local (over)densities. Figures 1 and 2 suggest that while the low-μ_{H_2} galaxies are embedded in coherent LSS, their relation with a local and/or small-scale environment does not stand out. Hence, there must be more than one parameter explaining the status of the galaxy gas reservoir that we are witnessing.

Similarly, we have looked into the environment of the PHIBSS2 galaxies. For the galaxies in the COSMOS field, we used the G10-COSMOS catalogue (Davies et al. 2015) for their position and redshift, and the zCOSMOS 20k group catalogue (Knobel et al. 2012). The 3D-HST survey catalogue (Brammer et al. 2012; Skelton et al. 2014; Momcheva et al. 2015) was used for the PHIBSS2 galaxies within the AEGIS and GOODS-North fields. We used the DEEP2 group catalogue (Gerke et al. 2012) for AEGIS. No equivalent group catalogue was found for GOODS-North. Among the 19 PHIBSS2 galaxies, only 5 belong to a group or are close to one. However, we did not find any correlation between their gas content and the density of their local environment.

4.4. Caveats

The derivation of cold gas masses involves two parameters, α_{CO} and r_{31}. This raises the question of whether the low-μ_{H_2} galaxies could arise from our choices of these parameters.

The PHIBSS2 CO conversion factor, α_{CO}, decreases with increasing metallicity, from 4.7 down to 3.8 $M_\odot\,(\mathrm{K\,km\,s^{-1}\,pc^2})^{-1}$. Applying the same definition and estimating the metallicity from its relation with the galaxy stellar mass as in Genzel et al. (2012), α_{CO} could in principle vary from $\alpha_{CO} = 3.76$ to 4.91 $M_\odot\,(\mathrm{K\,km\,s^{-1}\,pc^2})^{-1}$ over our range of masses. This would increase by 12% the cold molecular gas mass of the two lowest mass galaxies ($M_{star} \lesssim 10^{10}\,M_\odot$) in our sample, keep galaxies at $M_{star} \sim 10^{10}\,M_\odot$ at the same positions, and decrease by 13% the gas masses of the most massive of our target. None of these shifts would change the identification of the low-μ_{H_2} galaxies.

As to the flux ratios, the observations of PHIBSS2 were conducted in CO(2-1), with $r_{21} = 0.77$ as a trade off between the values found in earlier studies, which range from 1 to 0.6 (Freundlich et al. 2019). As seen from Eq. 3, increasing r_{31} decreases the galaxy gas mass, hence increasing the gas mass in our low-μ_{H_2} galaxies is not an option. As shown in previous studies of nearby galaxies (Mauersberger et al. 1999; Mao et al. 2010; Lamperti et al. 2020), there is a large scatter in r_{31} (∼0.1) with any fixed parameter involving the galaxy SFRs. It should be noted, however, that these nearby samples are mostly composed of galaxies above the main sequence unlike our targets. The value of r_{31} would need to be decreased by at least a factor 2 in order to reconcile our sample with the PHIBSS2 galaxies in Fig. 9. At the lowest tail of the distribution $r_{31} = 0.2$ is rarely encountered (Mao et al. 2010). Moreover, if r_{31} does vary from one galaxy to another, some normal systems could have r_{31} higher than 0.5. Hence, they would potentially move into the low-μ_{H_2} region. This issue definitely needs further observations directly in CO(1-0).

5. Conclusion

We have presented the CO(3-2) emission line fluxes obtained with ALMA for a sample of 27 galaxies located within $5{\times}R_{200}$ of the centre of the EDisCS cluster CL1411.1−1148 at $z = 0.5195$. This constitutes the largest sample of galaxies with direct cold gas measurements at a single intermediate redshift ($0.5000 < z < 0.5375$), and the only sample of galaxies in interconnected cosmic structures around a galaxy cluster.

Unlike most of the previous studies which targeted galaxies based on their SFRs, our selection is based on stellar masses and on ground-based photometry in the u, g, and i bands only, with the requirement that galaxies are in the blue cloud of the cluster colour–magnitude diagrams, and have available spectroscopic redshifts. The derivation of the galaxy stellar masses and star formation rates placed all but two of our targets on the MS of the normal star-forming galaxies, with stellar masses between $\log(M_{star}/M_\odot) = 9.8$ and 11.2, and SFRs ranging from $\log(SFR/(M_\odot yr^{-1})) = 0.3$ up to 1.7. Two galaxies fall within the passive region of the rest-frame UVJ colour–colour diagram. They still are very close to the star-forming sequence, which suggests that these systems are transitioning to a quenched state.

Our sample covers a wide range of cold molecular gas masses, from 1.38×10^9 up to 3×10^{10} $M_\odot$. The low tail of this gas mass distribution probes lower values than most other studies of CO at $z > 0.05$. We have compared our results to the PHIBSS2 survey (Freundlich et al. 2019), which is the best field counterpart to our study at $z \sim 0.5$. Looking at the link between galaxy gas fraction and stellar mass, we find that while 63% of our galaxies follow the same trend between μ_{H_2} and M_{star} as field galaxies, 37% of our targets fall below the 1σ variance of the relation derived for the field galaxies. This excess to one side of the field relation deviates significantly from the expected tail of sources for a Gaussian distribution and reveals a population that was absent from other surveys. Our cold molecular gas mass estimates depend on our choice of the CO conversion factor, α_{CO}, and the line ratio, r_{31}. But our results remain the same for all reasonable values of these parameters. Nevertheless direct observation of the CO(1-0) transition should help shed definitive light on this issue.

Interestingly, the SFRs of the low-μ_{H_2} galaxies are normal for their stellar masses. This indicates that their molecular gas reservoir changes, either in mass or properties, before the galaxy SF activity is impacted. Our sample displays a much larger scatter in μ_{H_2} than previously encountered in other studies at similar redshifts (at least two times larger). This is the case at fixed SF activity and stellar mass, as represented by the specific SFR normalised to the position of the galaxies on the mass sequence.

Although our galaxies have been selected in the vicinity of a galaxy cluster, we have not identified any correspondence between the low gas fraction of the galaxies and the local density of their environment.

Acknowledgements. We thank the anonymous referee whose detailed comments helped to improve the presentation of the paper. This paper makes use of the following ALMA data: ADS/JAO.ALMA#2015.1.01324.S and ADS/JAO.ALMA#2017.1.00257.S. ALMA is a partnership of ESO (representing its member states), NSF (USA) and NINS (Japan), together with NRC (Canada), MOST and ASIAA (Taiwan), and KASI (Republic of Korea), in cooperation with the Republic of Chile. The Joint ALMA Observatory is operated by ESO, AUI/NRAO and NAOJ. The authors are indebted to the *International Space Science Institute* (ISSI), Bern, Switzerland, for supporting and funding the international team "The Effect of Dense Environments on Gas in Galaxies over 10 Billion Years of Cosmic Time". We are grateful to the `Numpy` (Oliphant 2006; Van Der Walt et al. 2011), `SciPy` (Virtanen et al. 2020), `Matplotlib` (Hunter 2007), `IPython` (Pérez & Granger 2007) and `Astropy` (Robitaille et al. 2013;

Price-Whelan et al. 2018) teams for providing the scientific community with essential Python tools.

References

Abdo, A. A., Ackermann, M., Ajello, M., et al. 2010, ApJ, 710, 133
Alatalo, K., Crocker, A. F., Aalto, S., et al. 2015, MNRAS, 450, 3874
Bauermeister, A., Blitz, L., Bolatto, A. D., et al. 2013a, ApJ, 768, 132
Bauermeister, A., Blitz, L., Bolatto, A. D., et al. 2013b, ApJ, 763, 64
Baumgartner, W. H., Tueller, J., Markwardt, C. B., et al. 2013, ApJS, 207, 19
Berti, A. M., Coil, A. L., Hearin, A. P., & Moustakas, J. 2019, ApJ, 884, 76
Biviano, A., Rosati, P., Balestra, I., et al. 2013, A&A, 558, A1
Blanton, M. R. & Moustakas, J. 2009, ARA&A, 47, 159
Blanton, M. R. & Roweis, S. 2007, AJ, 133, 734
Bolatto, A. D., Wolfire, M., & Leroy, A. K. 2013, ARA&A, 51, 207
Brammer, G. B., van Dokkum, P. G., & Coppi, P. 2008, ApJ, 686, 1503
Brammer, G. B., Van Dokkum, P. G., Franx, M., et al. 2012, ApJS, 200, 13
Brammer, G. B., Whitaker, K. E., Van Dokkum, P. G., et al. 2009, ApJ, 706, L173
Bruzual, G. & Charlot, S. 2003, MNRAS, 344, 1000
Capak, P., Cowie, L. L., Hu, E. M., et al. 2004, AJ, 127, 180
Carleton, T., Cooper, M. C., Bolatto, A. D., et al. 2017, MNRAS, 467, 4886
Castignani, G., Jablonka, P., Combes, F., et al. 2020, A&A, 640, A64
Chabrier, G. 2003, PASP, 115, 763
Chapman, S. C., Bertoldi, F., Smail, I., et al. 2015, MNRAS Lett., 449, L68
Charlot, S. & Fall, S. M. 2000, ApJ, 539, 718
Cowie, L. L. & Songaila, A. 1977, Nature, 266, 501
Cybulski, R., Yun, M. S., Erickson, N., et al. 2016, MNRAS, 459, 3287
da Cunha, E., Charlot, S., & Elbaz, D. 2008, MNRAS, 388, 1595
Daddi, E., Bournaud, F., Walter, F., et al. 2010, ApJ, 713, 686
Dame, T. M., Hartmann, D., & Thaddeus, P. 2001, ApJ, 547, 792
Davies, L. J., Driver, S. P., Robotham, A. S., et al. 2015, MNRAS, 447, 1014
De Lucia, G., Poggianti, B. M., Aragón-Salamanca, A., et al. 2007, MNRAS, 374, 809
Dressler, A. 1980, ApJ, 236, 351
Dressler, A., Oemler, A., Poggianti, B. M., et al. 2013, ApJ, 770, 62
Driver, S. P., Allen, P. D., Graham, A. W., et al. 2006, MNRAS, 368, 414
Dumke, M., Nieten, C., Thuma, G., Wielebinski, R., & Walsh, W. 2001, A&A, 373, 853
Einasto, M., Deshev, B., Lietzen, H., et al. 2018, A&A, 610, A82
Erben, T., Hildebrandt, H., Lerchster, M., et al. 2009, A&A, 493, 1197
Finn, R. A., Desai, V., Rudnick, G., et al. 2010, ApJ, 720, 87
Freundlich, J., Combes, F., Tacconi, L. J., et al. 2019, A&A, 622, A105
Gao, Y. & Solomon, P. M. 2004, ApJS, 152, 63
García-Burillo, S., Usero, A., Alonso-Herrero, A., et al. 2012, A&A, 539, A8
Geach, J. E., Smail, I., Moran, S. M., et al. 2011, ApJL, 730, L19
Geach, J. E., Smail, I., Moran, S. M., Treu, T., & Ellis, R. S. 2009, ApJ, 691, 783
Genzel, R., Tacconi, L. J., Combes, F., et al. 2012, ApJ, 746, 69
Genzel, R., Tacconi, L. J., Lutz, D., et al. 2015, ApJ, 800, 20
Gerke, B. F., Newman, J. A., Davis, M., et al. 2012, ApJ, 751, 50
Gnedin, O. Y. 2003, ApJ, 582, 141
Gomez, P. L., Nichol, R. C., Miller, C. J., et al. 2003, ApJ, 584, 210
Gouin, C., Aghanim, N., Bonjean, V., & Douspis, M. 2020, A&A, 635, A195
Grenier, I. A., Casandjian, J. M., & Terrier, R. 2005, Sci., 307, 1292
Gunn, J. E. & Gott, J. R. I. 1972, Apj, 176, 1
Guzzo, L., Bel, J., Bianchi, D., et al. 2018, arXiv e-prints [arXiv:1803.10814]
Haines, C. P., Pereira, M. J., Smith, G. P., et al. 2015, ApJ, 806, 101
Halliday, C., Milvang-Jensen, B., Poirier, S., et al. 2004, A&A, 427, 397
Hayashi, M., Tadaki, K.-I., Kodama, T., et al. 2018, ApJ, 856, 118
Hunter, J. D. 2007, Computing in Science & Engineering, 9, 90
Jablonka, P., Combes, F., Rines, K., Finn, R., & Welch, T. 2013, A&A, 557, 8
Just, D. W., Zaritsky, D., Rudnick, G., et al. 2015, ApJ [arXiv:1506.02051]
Kauffmann, G., White, S. D., Heckman, T. M., et al. 2004, MNRAS, 353, 713
Kitaura, F. S., Jasche, J., Li, C., et al. 2009, MNRAS, 400, 183
Knobel, C., Lilly, S. J., Iovino, A., et al. 2012, ApJ, 753, 121
Kodama, T., Smail, I., Nakata, F., Okamura, S., & Bower, R. G. 2001, ApJ, 562, L9
Koyama, Y., Kodama, T., Shimasaku, K., et al. 2008, MNRAS, 391, 1758
Kraljic, K., Arnouts, S., Pichon, C., et al. 2018, MNRAS, 474, 547
Laigle, C., Pichon, C., Arnouts, S., et al. 2018, MNRAS, 474, 5437
Lamperti, I., Saintonge, A., Koss, M., et al. 2020, ApJ, 889, 103
Larson, R. B., Tinsley, B. M., & Caldwell, C. N. 1980, ApJ, 237, 692
Lemaux, B. C., Gal, R. R., Lubin, L. M., et al. 2012, ApJ, 745, 106
Leroy, A. K., Bolatto, A., Gordon, K., et al. 2011, ApJ, 737, 12
Lubin, L. M., Gal, R. R., Lemaux, B. C., Kocevski, D. D., & Squires, G. K. 2009, AJ, 137, 4867
Malavasi, N., Pozzetti, L., Cucciati, O., Bardelli, S., & Cimatti, A. 2016, A&A, 585, A116
Mancini, C., Daddi, E., Juneau, S., et al. 2019, MNRAS, 489, 1265
Mao, R. Q., Schulz, A., Henkel, C., et al. 2010, ApJ, 724, 1336
Mauersberger, R., Henkel, C., Walsh, W., & Schulz, A. 1999, A&A, 341, 256
McMullin, J. P., Waters, B., Schiebel, D., Young, W., & Golap, K. 2007, Astron. Soc. Pacific Conf. Ser., 376, 127
Miller, C. J., Nichol, R. C., Gomez, P. L., Hopkins, A. M., & Bernardi, M. 2003, ApJ, 597, 142
Milvang-Jensen, B., Noll, S., Halliday, C., et al. 2008, A&A, 482, 419
Mishra, H. D. & Dai, X. 2020, AJ, 159, 69
Momcheva, I. G., Brammer, G. B., van Dokkum, P. G., et al. 2015, ApJS, 225, 27
Moore, B., Katz, N., Lake, G., Dressler, A., & Oemler, A. 1996, Nature, 379, 613
Moran, S. M., Ellis, R. S., Treu, T., et al. 2007, ApJ, 671, 1503
Morokuma-Matsui, K., Baba, J., Sorai, K., & Kuno, N. 2015, PASJ, 67, 36
Muzzin, A., Wilson, G., Demarco, R., et al. 2013, ApJ, 767, 39
Noble, A. G., McDonald, M., Muzzin, A., et al. 2017, ApJL, 842, L21
Noble, A. G., Muzzin, A., McDonald, M., et al. 2019, ApJ, 870, 56
Olave-Rojas, D., Cerulo, P., Demarco, R., et al. 2018, MNRAS, 479, 2328
Oliphant, T. E. 2006, A guide to NumPy, Vol. 1 (Trelgol Publishing USA)
Patel, S. G., Kelson, D. D., Holden, B. P., et al. 2009, ApJ, 694, 1349
Pérez, F. & Granger, B. E. 2007, Computing in Science and Engineering, 9, 21
Pimbblet, K. A., Drinkwater, M. J., & Hawkrigg, M. C. 2004, MNRAS, 354, L61
Planck Collaboration. 2020, A&A, 641, A6
Price-Whelan, A. M., Sipőcz, B. M., Günther, H. M., et al. 2018, AJ, 156, 123
Riess, A. G., Casertano, S., Yuan, W., Macri, L. M., & Scolnic, D. 2019, ApJ, 876, 85
Robitaille, T. P., Tollerud, E. J., Greenfield, P., et al. 2013, A&A, 558, A33
Rudnick, G., Jablonka, P., Moustakas, J., et al. 2017, ApJ, 850, 181
Saintonge, A., Catinella, B., Tacconi, L. J., et al. 2017, ApJS, 233, 22
Salerno, J. M., Martínez, H. J., Muriel, H., et al. 2020, MNRAS, 493, 4950
Sánchez-Blázquez, P., Jablonka, P., Noll, S., et al. 2009, A&A, 499, 47
Sandstrom, K. M., Leroy, A. K., Walter, F., et al. 2013, ApJ, 777, 5
Scholz, F. W. & Stephens, M. A. 1987, J. Am. Stat. Assoc., 82, 918
Skelton, R. E., Whitaker, K. E., Momcheva, I. G., et al. 2014, ApJS, 214, 24
Skrutskie, M. F., Cutri, R. M., Stiening, R., et al. 2006, AJ, 131, 1163
Solanes, J. M., Sanchis, T., Salvador-Solé, E., Giovanelli, R., & Haynes, M. P. 2002, AJ, 124, 2440
Solomon, P. & Vanden Bout, P. 2005, ARA&A, 43, 677
Solomon, P. M., Downes, D., Radford, S. J. E., & Barrett, J. W. 1997, ApJ, 478, 144
Speagle, J. S., Steinhardt, C. L., Capak, P. L., & Silverman, J. D. 2014, ApJS, 214, 15
Spilker, J., Bezanson, R., Barišić, I., et al. 2018, ApJ, 860, 103
Springel, V., Pakmor, R., Pillepich, A., et al. 2018, MNRAS, 475, 676
Strateva, I., Ivezić, Ž., Knapp, G. R., et al. 2001, AJ, 122, 1861
Tacconi, L. J., Genzel, R., Neri, R., et al. 2010, Nature, 463, 781
Tacconi, L. J., Genzel, R., Saintonge, A., et al. 2018, ApJ, 853, 179
Tacconi, L. J., Neri, R., Genzel, R., et al. 2013, ApJ, 768 [arXiv:1211.5743]
Tanaka, M., Lidman, C., Bower, R. G., et al. 2009, A&A, 507, 671
Van Der Walt, S., Colbert, S. C., & Varoquaux, G. 2011, Computing in Science & Engineering, 13, 22
Virtanen, P., Gommers, R., Oliphant, T. E., et al. 2020, Nature Methods, 17, 261
White, S. D., Clowe, D. I., Simard, L., et al. 2005, A&A, 444, 365
Williams, R. J., Quadri, R. F., Franx, M., Van Dokkum, P., & Labbé, I. 2009, ApJ, 691, 1879
Wilson, C. D., Warren, B. E., Israel, F. P., et al. 2012, MNRAS, 424, 3050
Zhang, H., Zaritsky, D., Behroozi, P., & Werk, J. 2019, ApJ, 880, 28
Zinger, E., Dekel, A., Kravtsov, A. V., & Nagai, D. 2018, MNRAS, 475, 3654

Appendix A: ALMA maps and spectra of our galaxies

In this appendix we present the *i*-band images, the ALMA intensity maps, and the spectra of all of our targets. The low-μ_{H_2} targets are indicated as such by a label at the bottom left of the *i*-band image.

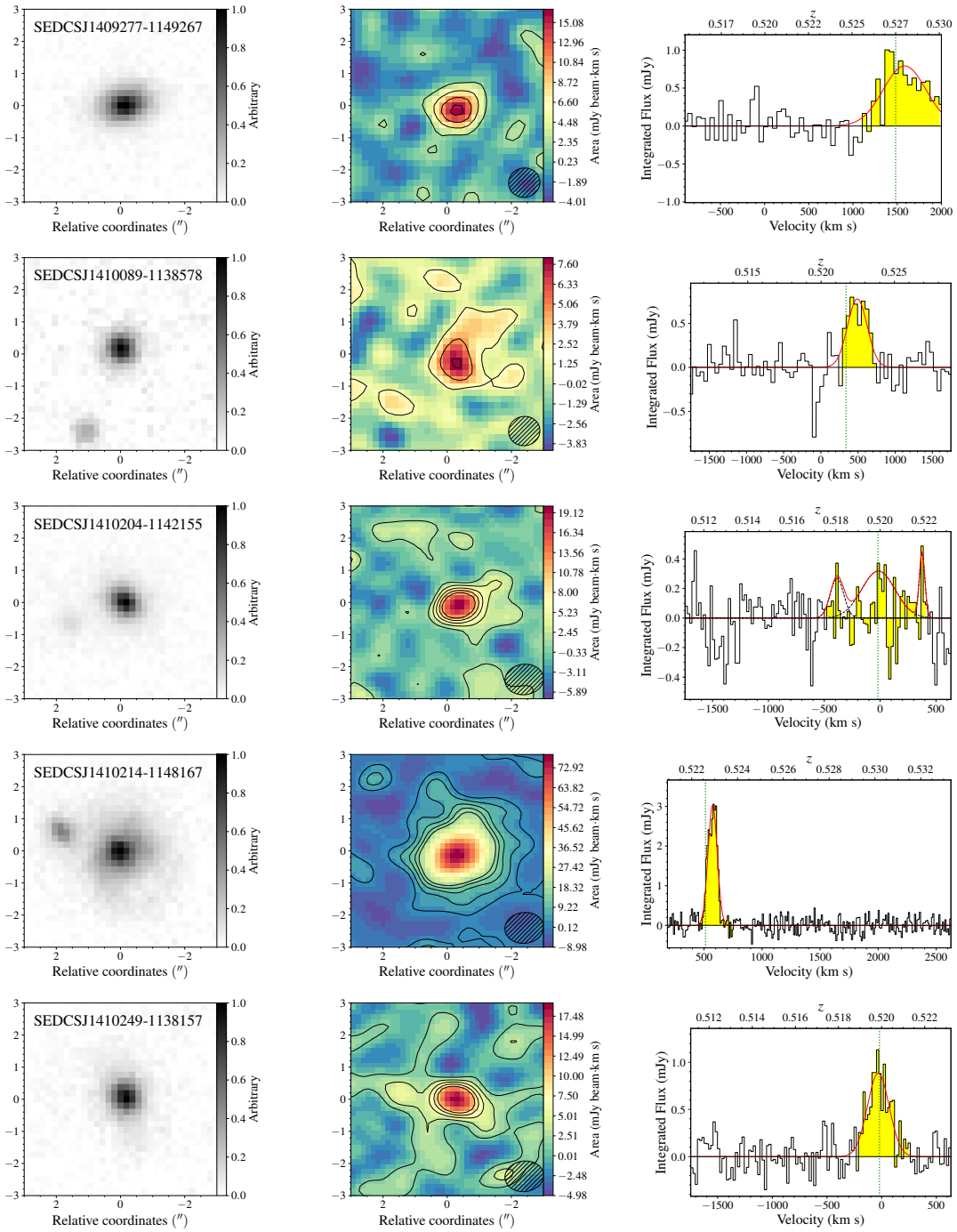

Fig. A.1: *Left*: CFHT/MEGACAM *i*-band images of our galaxies, unless stated otherwise, in a 6″ × 6″ snapshot, centred on the galaxies coordinates. *Middle*: ALMA map of the CO(3-2) emission around our galaxies. Spatial scale is the same as in the left panel. The colour wedge of the intensity map is in mJy/beam km s^{-1}. The contours are defined such that they are spaced by 2 times the rms starting at 1 time above the rms. In the bottom right corner is the beam size. *Right*: The spectrum shows the flux, $S_{\rm CO}$, spatially integrated as indicated in Sect. 2.2, of the source in mJy in function of the velocity in km s^{-1}, with respect to a fixed frequency. The Gaussian profiles are fits of the emission lines from which we derived our FWHMs. The yellow filled zones correspond to the spectral extent of the emissions. The green vertical line corresponds to the spectroscopic redshift.

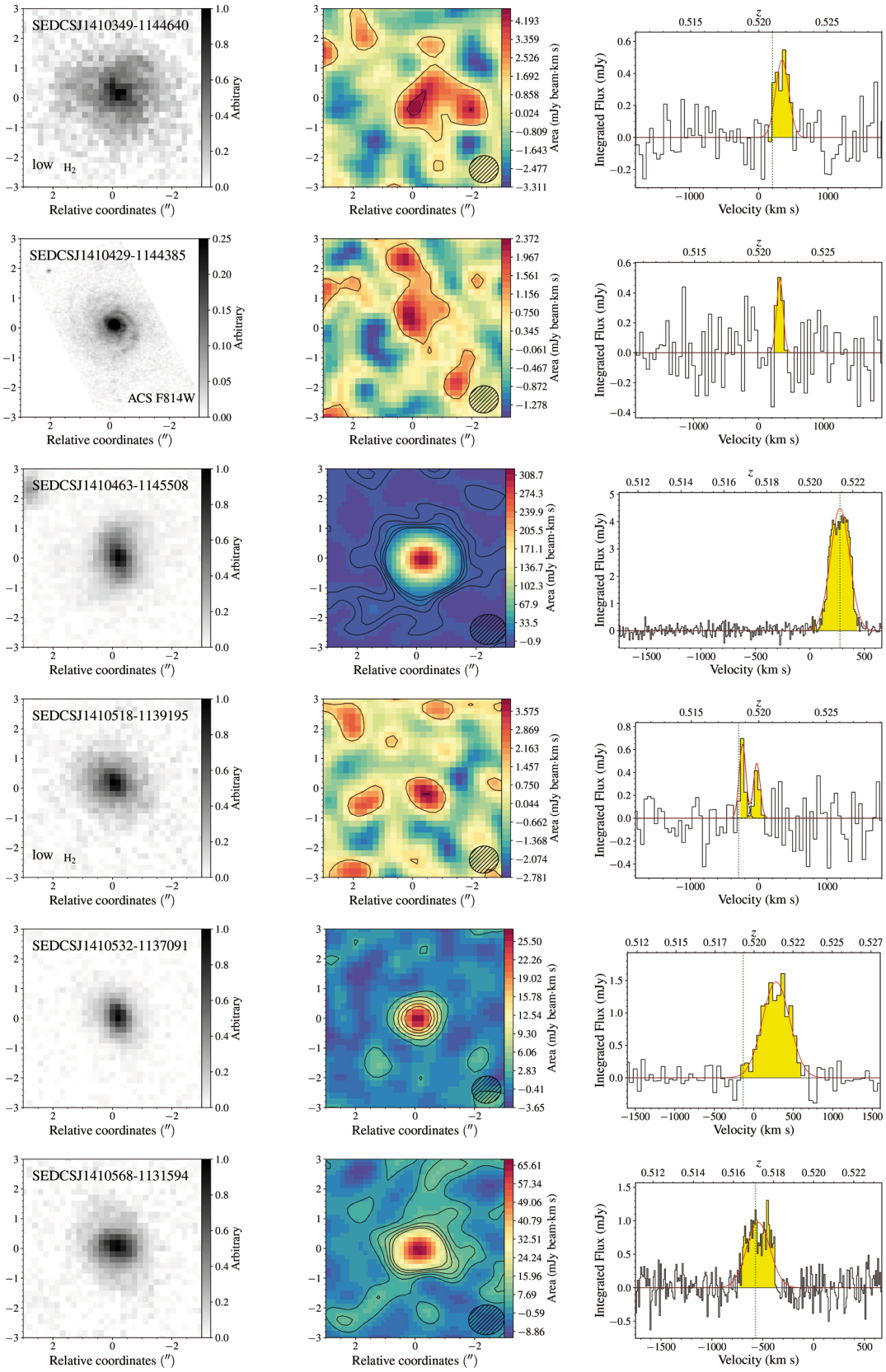

Fig. A.1: Continued.

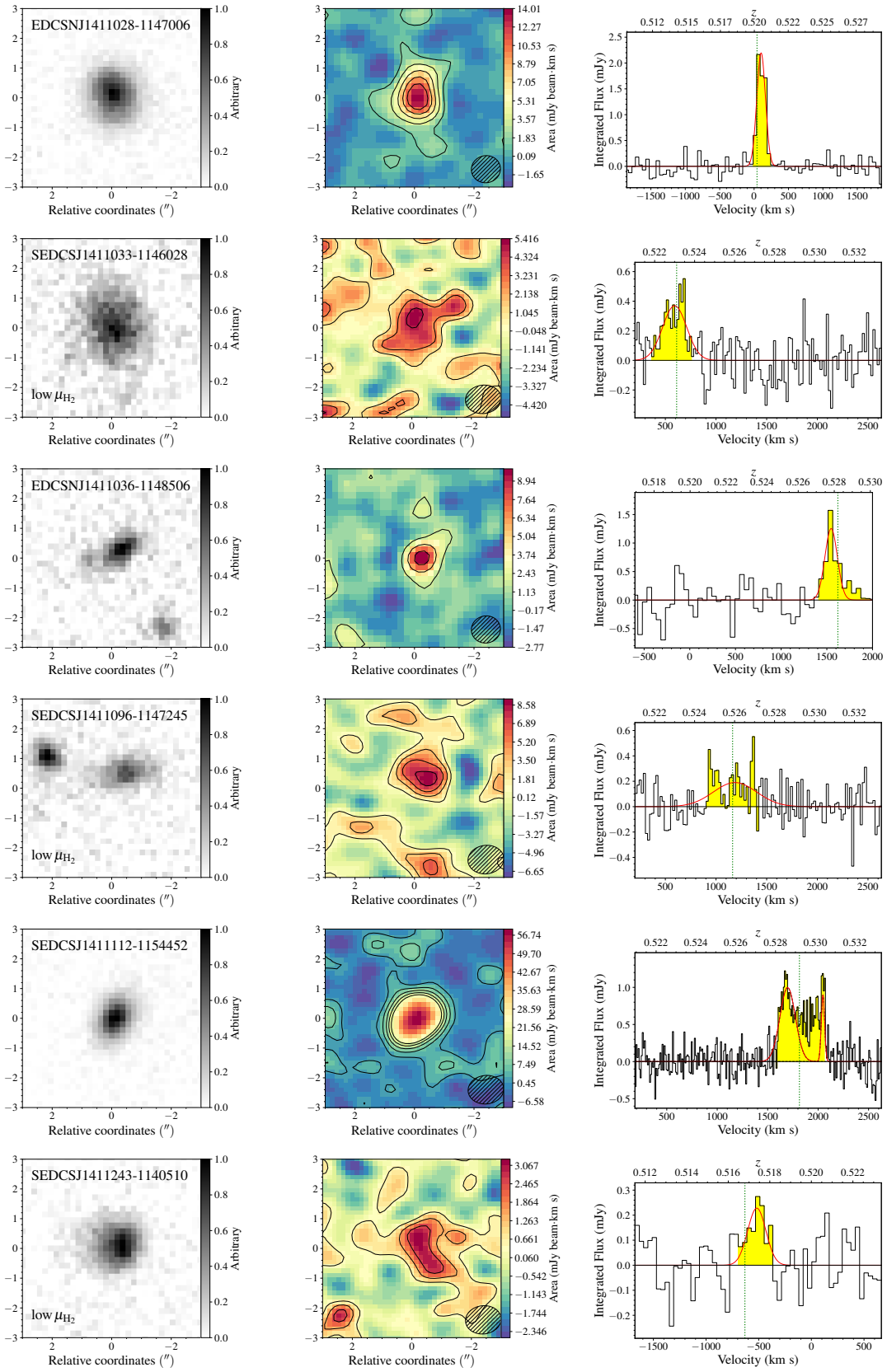

Fig. A.1: Continued.

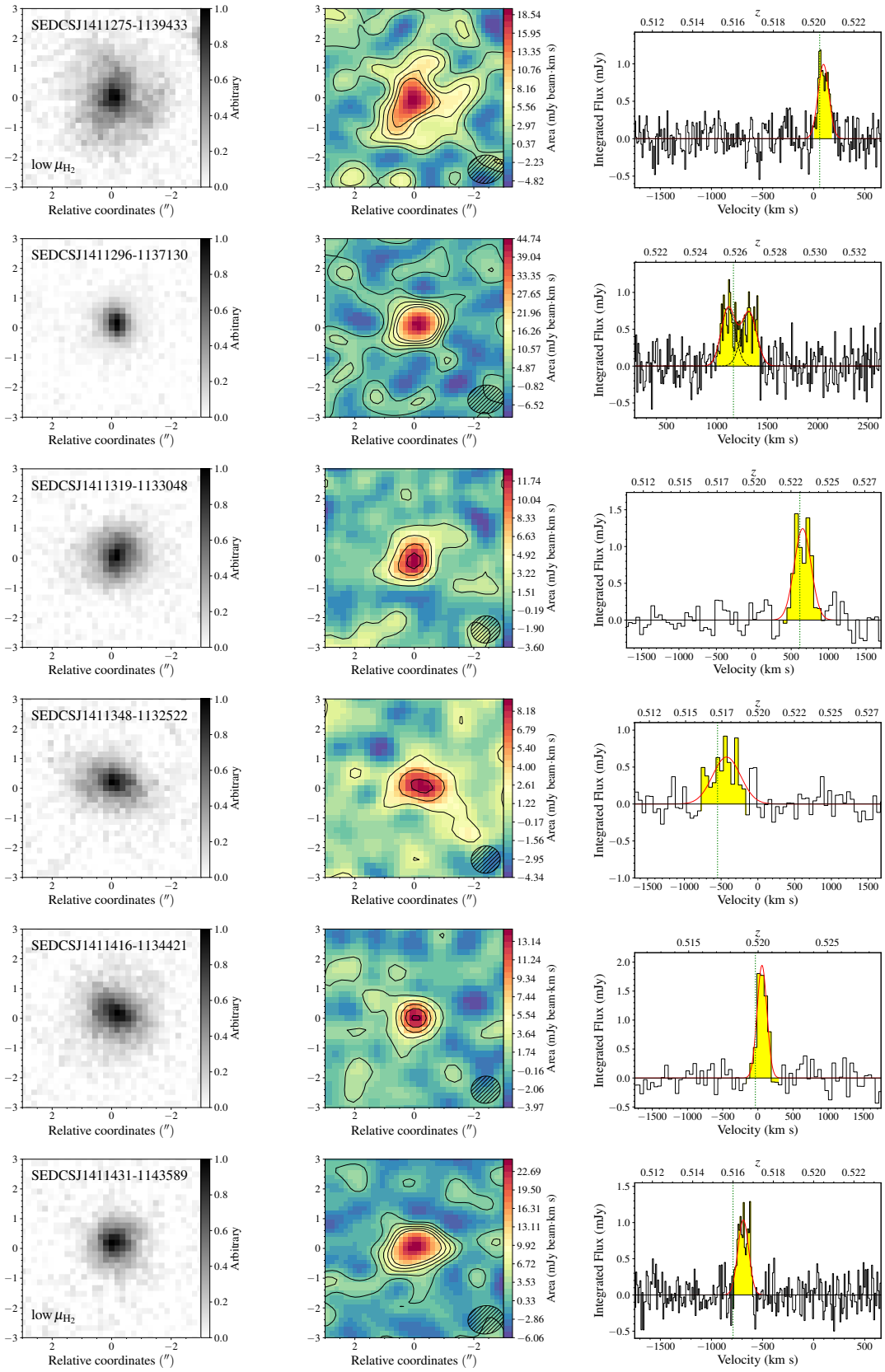

Fig. A.1: Continued.

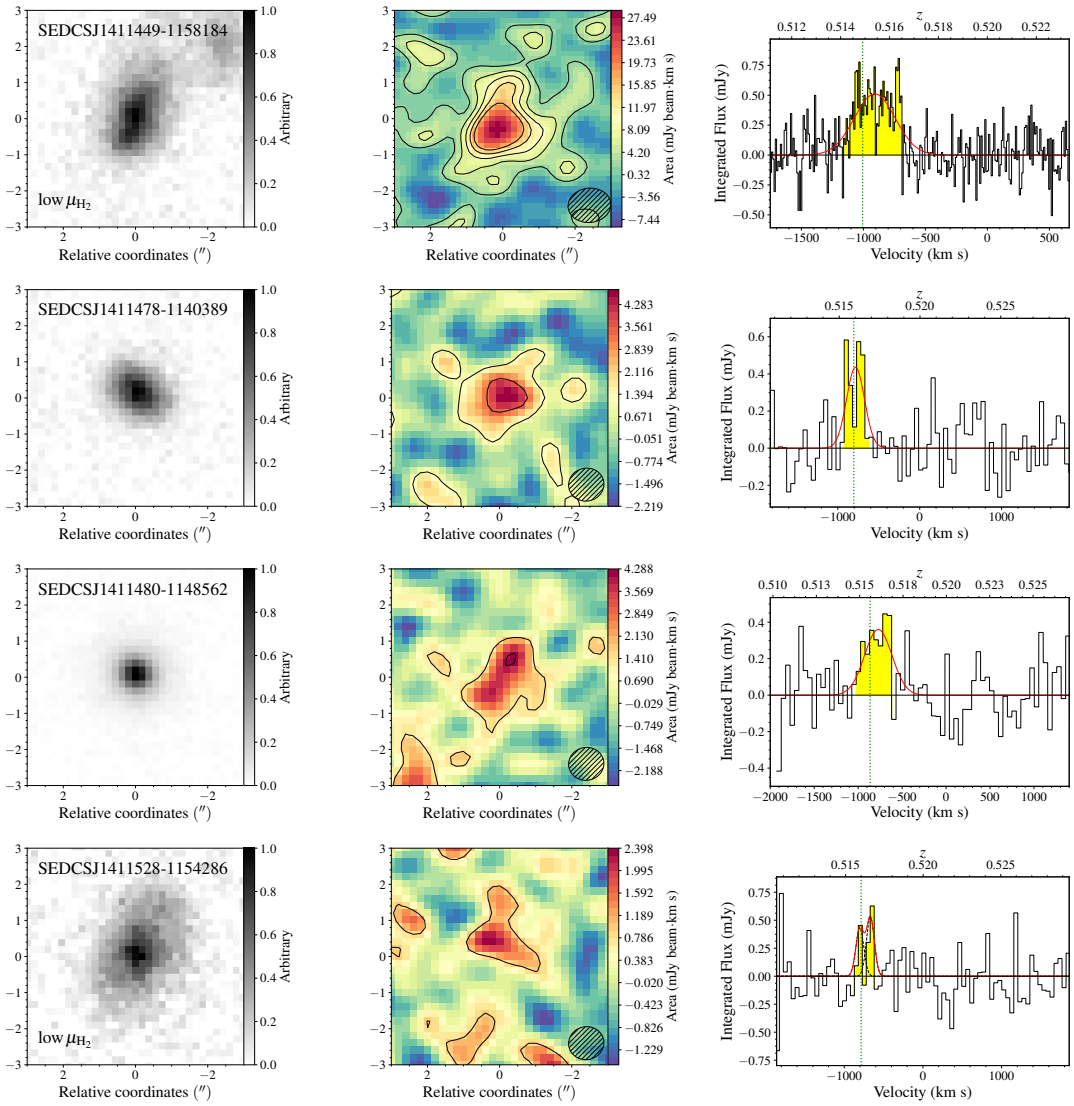

Fig. A.1: Continued.

4 Paper II : ALMA results for CL1301.7−1139

In this chapter, we show the pre-print submitted to A&A and still under refereeing process at the time of writing this thesis. It is about the ALMA results for CL1301.7−1139 and the comparison between both clusters.

We present the observation and analysis of the second sample of CO detections performed within the same cluster environment, up to $6 \times R_{200}$ away from CL1411.1−1148. Just like in Paper I, our sample selection did not impose a minimum star formation rate or detection in FIR. It delivers by itself an unbiased view of the gas content of normal star-forming galaxies at $z \sim 0.45$. Here again, our observations revealed a number of star forming galaxies with lower gas fractions, compared to other galaxies at the same stellar mass, that previous surveys did not detect. Our 16% ratio (3 galaxies out of 22) of low-μ_{H_2} galaxies for this cluster is more than two times lower than the one for CL1301.7−1139 (36%), but still is significant. More galaxies in this sample are legitimate cluster members, 8, than those from CL1411.1−1148 sample. But only 2 of those have decreased cold gas fractions, with one still on within the main sequence, while the third low-μ_{H_2} galaxy is transitioning towards the passive sequence. This study highlights the assortment of paths to star formation suppression, as well as the variety of physical properties of the galaxy cold gas reservoir.

Astronomy & Astrophysics manuscript no. CL1301_CO_draft
March 30, 2021

SEEDisCS

II. Molecular gas in galaxy clusters and their large scale structure: the case of CL1301.7−1139

D. Spérone-Longin[1], P. Jablonka[1,2], F. Combes[3,4], G. Castignani[1,5], M. Krips[6], G. Rudnick[7], T. Desjardins[7], D. Zaritsky[8], R. A. Finn[9], G. De Lucia[10], and V. Desai[11]

[1] Institute of Physics, Laboratory of Astrophysics, École Polytechnique Fédérale de Lausanne (EPFL), Observatoire de Sauverny, CH-1290 Versoix, Switzerland
[2] GEPI, Observatoire de Paris, PSL University, CNRS, 5 Place Jules Janssen, 92190 Meudon, France
[3] Observatoire de Paris, LERMA, CNRS, Sorbonne University, PSL Research Universty, 75014 Paris, France
[4] Collège de France, 11 Place Marcelin Berthelot, 75231 Paris, France
[5] Dipartimento di Fisica e Astronomia, Alma Mater Studiorum Università di Bologna, Via Gobetti 93/2, I-40129 Bologna, Italy
[6] IRAM, Domaine Universitaire, 300 rue de la Piscine, 38406 Saint-Martin-d'Hères, France
[7] Department of Physics and Astronomy, The University of Kansas, Lawrence, KS, USA
[8] Steward Observatory and Department of Astronomy, University of Arizona, Tucson, AZ, USA
[9] Department of Physics and Astronomy, Siena College, Loudonville, NY, USA
[10] INAF – Osservatorio Astronomico di Trieste, Via G. B. Tiepolo 11, 34143 Trieste, Italy
[11] IPAC, Mail Code 100-22, Caltech, 1200 E. California Boulevard, Pasadena, CA, USA

March 30, 2021

ABSTRACT

This paper is the second of a series that tackles the properties of molecular gas in galaxies residing in clusters and their related large-scale structures. We report on the observation of 22 galaxies in the CO(3-2) line gathered with the Atacama Large Millimeter Array (ALMA). These galaxies are either bona fide members of the CL1301.7−1139 cluster ($z = 0.4828$, $\sigma_{cl} = 681\,\mathrm{km\,s^{-1}}$), or located within $\sim 7\times R_{200}$, its virial radius. They have been selected to sample the range of photometric local densities around CL1301.7−1139, with stellar masses above $\log(M_{\mathrm{star}}) = 10$, and to be located in the blue clump of star forming galaxies derived from the u, g, and i photometric bands. Unlike previous works, our sample selection does not impose a minimum star formation rate or detection in the far infrared. As such and as much as possible, it delivers an unbiased view of the gas content of normal star forming galaxies at $z \sim 0.5$. Our study highlights the variety of paths to star formation quenching, and most likely the variety of physical properties (i.e. temperature, density) of the corresponding galaxy cold molecular gas. Just as in the case of CL1411.1−1148, although to a smaller extent, we identify a number of galaxies with lower gas fraction than classically found in other surveys. These galaxies can still be on the star forming main sequence. When these galaxies are not inside the cluster virialized region, we provide hints that they are linked to their infall regions within $\sim 4 \times R_{200}$.

Key words. galaxies: evolution – galaxies: clusters: general – submillimeter: galaxies

1. Introduction

It is long established that the fraction of ellipsoidal and passive galaxies is dramatically increased in galaxy clusters in comparison with the field (Dressler 1980; Smith et al. 2005). There is now a growing body of evidence, from both observations and numerical simulations, that the related decrease in galaxy star formation activity begins already much beyond the cluster centres (r ≥ 2–4 virial radii; Gomez et al. 2003; Bahé et al. 2013; Haines et al. 2015; Gouin et al. 2020), possibly in groups, which are later accreted (Balogh et al. 2004; McGee et al. 2009; Bianconi et al. 2018).

We have entered a precision era in which the interplay between the growth of the cosmic structures and galaxy evolution can be investigated in detail. The most massive or quiescent galaxies are found the closest to the filament axes (Malavasi et al. 2016; Laigle et al. 2018). This large scale colour-density relation is seen even at z∼1 (e.g., Guzzo et al. 2018). However, quenching can not be related to density in a simple way. As a matter of fact, star-forming galaxies exist in environments that span 4 orders of magnitude in local density (Peng et al. 2010). Song et al. (2021) have looked into the relative influence of local density and proximity to filaments. They conclude that the high vorticity of the filament plays an important role in star formation quenching, by impeding gas transfer to the galaxies.

Identifying how and where cold gas is abundant or missing, where its properties can change, is at the heart of our understanding of the nature and operation modes of star formation at galactic scales (Bigiel et al. 2008; Leroy et al. 2008; Schruba et al. 2011). Molecular gas is unlikely to be as easily stripped as H I, because it is denser and more centrally concentrated. Nevertheless, there are a number of spectacular examples of ram pressure stripping of molecular gas in the local universe, such as, for example, in the Coma and Virgo clusters (Scott et al. 2015; Jachym et al. 2014, 2017). Yet, it is impossible to ascertain that these examples reveal the general mechanism responsible for the suppression of star formation in dense environments. There is no

established consensus on the possible dependence of the galaxy cold gas content and its environment (e.g., Boselli et al. 2014; Koyama et al. 2017). Lee et al. (2017) suggest that one should instead investigate whether the gas properties (density, temperature) are modified.

So far studies of the cold molecular gas content of galaxies have mostly focused on distinct environments, isolating the field (Gao & Solomon 2004; Abdo et al. 2010; Daddi et al. 2010; Tacconi et al. 2010, 2013; García-Burillo et al. 2012; Baumgartner et al. 2013; Bauermeister et al. 2013b,a; Morokuma-Matsui et al. 2015; Saintonge et al. 2017; Hayashi et al. 2018; Spilker et al. 2018; Freundlich et al. 2019; Lamperti et al. 2020), from groups (Boselli et al. 1996; Martinez-Badenes et al. 2012; Lisenfeld et al. 2017) and clusters (Geach et al. 2009, 2011; Jablonka et al. 2013; Rudnick et al. 2017a; Noble et al. 2017, 2019; Castignani et al. 2020). From the latter, rare are those which extend beyond the cluster virial radii on purpose (e.g., Morokuma-Matsui et al. 2021; Castignani et al. 2021).

This paper is the second of a series that tackles the properties of molecular gas in galaxies residing in clusters and their related large-scale structures. This survey concentrates on two spectroscopically well-characterised, intermediate-redshift, medium-mass clusters selected from the ESO Distant Cluster Survey (EDisCS, White et al. 2005). The first results of the Spatially Extended EDisCS survey (SEEDisCS) were presented in Spérone-Longin et al. (2021, hereafter Paper I).

This paper reports on the observations in CO(3-2) with the Atacama Large Millimeter Array (ALMA) of 22 galaxies in and around the second SEEDisCS galaxy cluster, CL1301.7−1139, at $z = 0.4828$, and with a velocity dispersion of $\sigma_{cl} = 681\,\mathrm{km\,s^{-1}}$. It is organized as follow: Section 2 details our selection of the sample and presents its observation with ALMA. In Sect. 3 we present our results and our derivation of the galaxy parameters. We discuss our results in Sect. 4, and we give our conclusions in Sect. 5.

In the following, we assume a flat ΛCDM cosmology with $\Omega_m = 0.3$, $\Omega_\Lambda = 0.7$ and $H_0 = 70\,\mathrm{km\,s^{-1}\,Mpc^{-1}}$ (see Riess et al. 2019; Aghanim et al. 2020), and we use a Chabrier initial mass function (IMF) (Chabrier 2003). All magnitudes are in the AB system.

2. Sample and observations

2.1. Sample selection

The 22 targets presented in this work are located inside CL1301.7−1139 and in its large-scale structures (Milvang-Jensen et al. 2008). CL1301.7−1139 was chosen from EDisCS (White et al. 2005)) because, at its intermediate redshift, environmentally induced galaxy transformation was in its heyday, and because its medium mass makes it a valid representative of the progenitors of typical nearby galaxy clusters (Milvang-Jensen et al. 2008). We have first assembled CFHT/MEGACAM u, g, r, i, and z, deep imaging over a 1 deg^2 field of view, i.e. covering a region of radius r ∼ 10 Mpc around the cluster center. K_s deep imaging from GEMINI/NEWFIRM was obtained over an area of 0.24 deg^2, covering 5 cluster virial radii (R_{200}). Photometric redshifts, z_{phot} were obtained with EAZY (Brammer et al. 2008) and are very accurate, with a normalized median absolute deviation $\sigma_{NMAD} \sim 0.036$. They have enabled the identification of the filamentary structures and infalling groups around CL1301.7−1139 (see Fig. 1).

The targets for the ALMA follow-up were selected on four criteria: ***i)*** they have spectroscopic redshifts from ESO/FORS2 or MMT/Hectospec, or at least a robust estimate from the IMACS Low Dispersion Prism ($\sigma_z = 0.007$, Just et al. (2019)), all falling within $3\sigma_{cl}$; ***ii)*** they are located within $7 \times R_{200}$[1], sampling the range of photometric local densities encountered around CL1301.7−1139 (see Fig.1); ***iii)*** they have stellar masses above $\log(M_{star}) = 10$; ***iv)*** they cover the same sequence in $u - g$ versus $g - i$ typical of star forming galaxies as in CL1411.1−1148 at $z = 0.5195$ (Paper I).

Table 1 provides the coordinates and optical redshifts of our targets, together with their stellar masses (M_{star}) and star formation rates (SFRs).

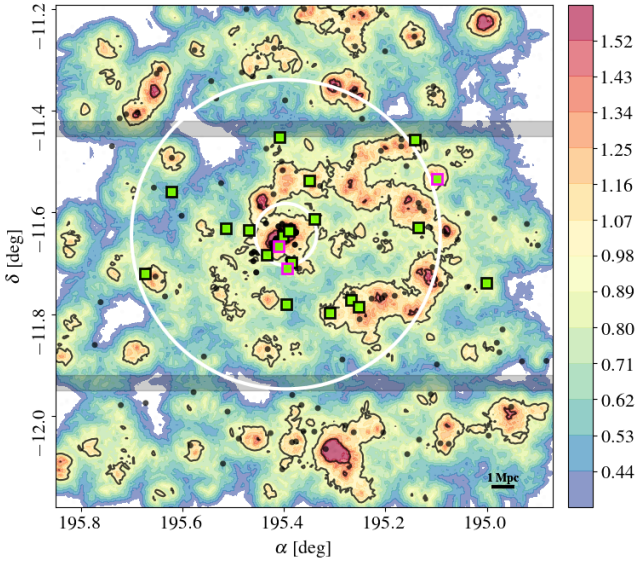

Fig. 1: Density map, based on u, g, r, i, and z images, of the CFHT/MEGACAM 1°×1° field around CL1301.7−1139. The colour-coding indicates the $\log_{10}$ of the density of galaxies averaged over the ten nearest neighbours. Black contours are at 1 and 3σ above the field mean density. The grey points identify all galaxies with a z_{spec} within $5\sigma_{cl}$ of the cluster redshift. The inner and outer white circles are positioned at a R_{200} and $5R_{200}$ radius, respectively. The grey bands indicate the gaps between the MEGACAM CCDs. The green squares show our ALMA targets. The pink outline shows the position of the star forming galaxies with low gas fractions (see Fig. 8 and Sect. 4.1).

Figure 1 presents the position of our targets in the global photometric density map, as calculated from the u, g, r, i, and z images, in the 1°×1° region centred on CL1301.7−1139. Densities are calculated within a photometric slice of $\pm 1\delta_{cl} = (1+z_{cl})\times \sigma_{NMAD} = 0.0533$ around the cluster redshift. Within this photometric redshift slice, we use a 'nearest neighbour' approach, in which for any point (x, y) one estimates the distance $r_N(x, y)$ to the Nth nearest neighbour. The density is thus the ratio between the (fixed) N and the surface defined by the adaptive distance: $\rho_N(x, y) = \frac{N}{\pi r_N^2(x,y)}$. We choose $N = 10$, which corresponds to an average scale of about 0.8 Mpc and with 90% of the values being smaller than ∼ 1.5 Mpc.

Figure 2 provides another view of the spatial distribution of our ALMA targets, keeping the same 1°×1° MEGACAM field of view. The galaxy positions are calculated relative to the position of the brightest cluster galaxy (BCG) in redshift and right

[1] For consistency with previous EDisCS works, R_{200} is calculated from the cluster line-of-sight velocity dispersion as in Finn et al. (2005)

ascension (RA) (White et al. 2005). The galaxy relative position in redshift, $\Delta d_{\rm cl}$, is computed by taking the difference between the comoving distances of the galaxy and of the BCG. The relative position in RA, ΔRA, is obtained by transforming the angular separation between the BCG and the galaxy into a distance, using the angular distance at the redshift of the galaxy. Our full spectroscopic sample within $\pm 3 \times \sigma_{\rm cl}$ of $z_{\rm cl}$ is presented as well as the photometric membership candidates. The finger-of-God structure due to the relative velocities of the galaxies in CL1301.7−1139 is clearly seen along the $\Delta d_{\rm cl}$-axis. Eight of our targets are genuine cluster members, within or at the cluster virial radius, and with $v/\sigma_{cl} \lesssim 1$. They are identified in Table 1 by their original EDisCS names. Three galaxies, namely, SEDCSJ1301144−1147490, SEDCSJ1301044−1146232, and SEDCSJ1301007−1147075, fall on the South-West photometric overdensity at RA ∼ 195.3 ($\Delta d_{\rm cl}$ ∼ 20 Mpc, ΔRA ∼ −3). They have a mean redshift of 0.488 with a standard deviation of $\sigma_z = 9.8{\times}10^{-4}$. Two other galaxies, with spectroscopic redshifts, however without CO observations, fall in this redshift interval as well, suggesting that these three ALMA targets indeed belong to a group with $\sigma_{\rm g}$ ∼150–200 km s^{-1}. The rest of our ALMA sample is either located in low density regions or photometric overdensities, which remain to be spectroscopically confirmed.

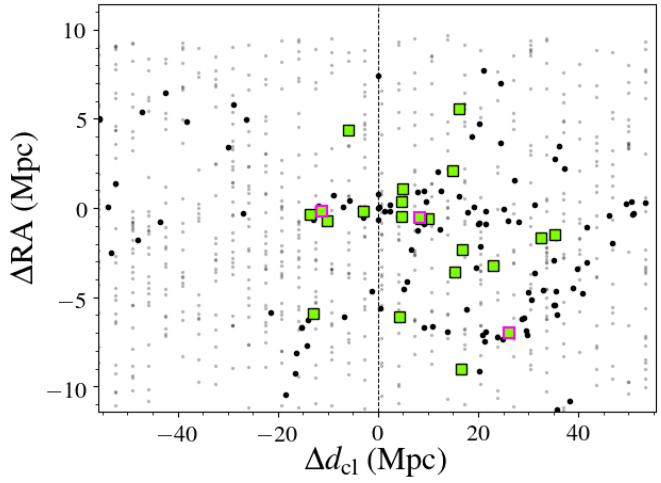

Fig. 2: Light cone centred on $z_{\rm clus} = 0.4828$ and extending to $\pm 1\delta_{\rm cl}$ in redshift. In right ascension, 1° is covered. The vertical line is located at the cluster redshift, $z_{\rm cl} = 0.4828$. The grey points are for the galaxies with a photometric redshift. Galaxies with spectroscopic redshifts are in black. Our sample is in green, and lower $\mu_{\rm H_2}$ (see Sect. 4.1) galaxies are outlined in pink. Distances are expressed relative to the brightest cluster galaxy (BCG).

Figure 3 displays the distribution of our targets in the $g - i$ vs $u - g$ colour–colour diagram, using total magnitudes. The ALMA targets in and around CL1301.7−1139 as well as those in and around CL1411.1−1148, for comparison, are shown. The CL1301.7−1139 galaxies span most of the blue clump, extending into the lower $g - i$ boundary of the red sequence. Three systems fall well below the red sequence, however are red in $u - g$.

Figure 4 presents the rest-frame $U - V$ vs $V - J$ colour–colour diagram that further helps discriminate between passive and star-forming galaxies (Williams et al. 2009). The rest-frame colours were derived with EAZY (Brammer et al. 2008). We

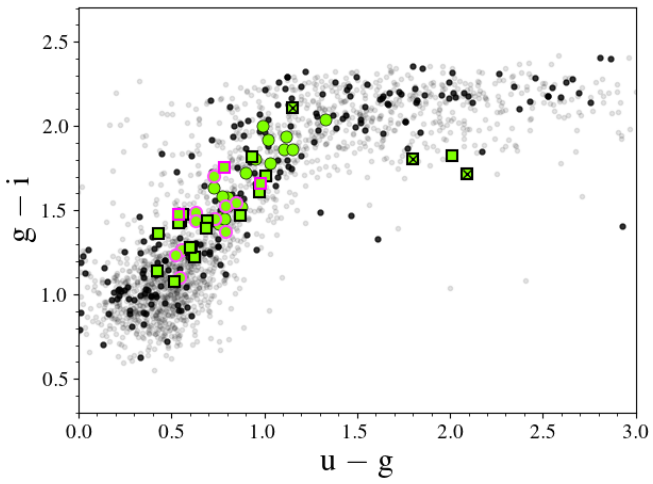

Fig. 3: Observed colour–colour diagram, $g - i$ as a function of $u - g$ for the galaxies in the CL1301.7−1139 region. Our ALMA sample is shown in green, with squares for CL1301.7−1139 and with circles for CL1411.1−1148. In both cases, pink borders indicate star forming galaxies that have low gas fractions for their stellar masses (see Sect. 4.1). The small black dots show galaxies with spectroscopic redshifts within $3 \times \sigma_{\rm cl}$ of the CL1301.7−1139 redshift. Galaxies that were not detected in CO are indicated with a cross.

used the Johnson-Cousins U and V bands, and the 2MASS J band (Skrutskie et al. 2006), together with a set of six templates: five main component templates obtained following the Blanton & Roweis (2007) algorithm and one for dusty galaxies (Brammer et al. 2008). From the four galaxies which were photometrically falling in the green valley as inferred from the u, g, and i bands, three turn out to be located in the UVJ region of passive systems. Two of them, namely EDCSNJ1301336−1138071 and EDCSNJ1301336−1138090, were falling in the same ALMA field of view. EDCSNJ1301336−1138071 was our primary target. Both are cluster members. The rest of our targets follow the UVJ star-forming sequence, including EDCSNJ1301441−1140589 which was red in $u - g$ and at the blue $g - i$ border of the red sequence.

2.2. ALMA observations

The observations were conducted in the CO(3-2) line (233 GHz at $z \sim 0.48$), falling in the ALMA Band 6, in compact configurations C43−2, for a beam size of $1.2'' \times 0.95''$ during the Cycle 5 (program 2017.1.00257.S). The integration time on targets was of 6.75 hours, 11h with overheads. The rms noise ranges from 29 to 84 μJy/beam for a spectral resolution of 50.7 km s^{-1}.

The same data reduction procedure as for the CL1411.1−1148 (Paper I) has been applied, with the CASA ALMA Science Pipeline (McMullin et al. 2007). Problems with antennas and runs were flagged (< 3%), the continuum was subtracted, while excluding the spectral channels of the line emission during the fit of the continuum – as we only focus on the CO line – and the primary beam has been corrected in order to form an astronomically correct image of the sky. The final continuum-subtracted and primary-beam-corrected maps were

Table 1: Galaxy ID, coordinates, optical spectroscopic redshifts and SED-based estimates of the $M_{\rm star}$ and SFRs of our galaxy sample observed with ALMA.

IDs	R.A. (J2000)	Dec (J2000)	$z_{\rm spec}$	$M_{\rm star}$ (10^{10} M$_\odot$)	SFR$_{SED}$ (M$_\odot$ yr^{-1})
SEDCSJ1300003−1144203	13:00:00.3688	−11:44:20.346	0.4878	$4.68^{+1.83}_{-1.29}$	$6.64^{+9.63}_{-4.59}$
SEDCSJ1300234−1132052†	13:00:23.4345	−11:32:05.222	0.4907	$7.41^{+2.05}_{-2.22}$	$8.85^{+9.78}_{-7.85}$
SEDCSJ1300324−1137445	13:00:32.4211	−11:37:44.584	0.4841	$3.63^{+1.34}_{-1.09}$	$16.48^{+14.42}_{-6.45}$
SEDCSJ1300340−1127269	13:00:34.0731	−11:27:26.913	0.4789	$3.98^{+1.19}_{-1.1}$	$8.07^{+5.48}_{-4.65}$
SEDCSJ1301007−1147075	13:01:00.7272	−11:47:07.522	0.4770^{a}	$2.63^{+0.61}_{-0.67}$	$4.86^{+2.91}_{-2.46}$
SEDCSJ1301044−1146232	13:01:04.4539	−11:46:23.263	0.4880^{a}	$1.91^{+0.44}_{-0.39}$	$10.76^{+7.06}_{-3.96}$
SEDCSJ1301144−1147490	13:01:14.4426	−11:47:49.051	0.4879	$2.82^{+0.84}_{-0.65}$	$7.80^{+5.84}_{-4.31}$
SEDCSJ1301216−1136480	13:01:21.6371	−11:36:48.027	0.4927	$5.13^{+1.06}_{-1.06}$	$12.22^{+7.6}_{-6.05}$
SEDCSJ1301240−1132137	13:01:24.0810	−11:32:13.735	0.4790^{a}	$4.07^{+0.94}_{-0.75}$	$14.86^{+9.58}_{-5.65}$
EDCSNJ1301323−1141558	13:01:32.3246	−11:41:55.846	0.4797	$3.80^{+0.79}_{-0.70}$	$10.52^{+5.57}_{-4.36}$
EDCSNJ1301336−1138071*	13:01:33.6127	−11:38:07.126	0.4858	$3.63^{+1.50}_{-0.50}$	$0.36^{+0.24}_{-0.36}$
EDCSNJ1301336−1138090*	13:01:33.6420	−11:38:09.025	0.4854	$8.32^{+1.72}_{-2.49}$	$0.52^{+0.46}_{-0.48}$
EDCSNJ1301344−1142380†	13:01:34.4495	−11:42:38.039	0.4853	$1.82^{+0.38}_{-0.42}$	$1.44^{+0.93}_{-0.81}$
SEDCSJ1301349−1146512	13:01:34.9086	−11:46:51.222	0.4842	$7.41^{+1.54}_{-2.05}$	$4.09^{+3.3}_{-2.73}$
EDCSNJ1301363−1138495	13:01:36.3447	−11:38:49.502	0.4787	$3.47^{+0.64}_{-0.80}$	$4.00^{+3.45}_{-2.62}$
SEDCSJ1301380−1127055	13:01:38.0353	−11:27:05.546	0.4819	$7.59^{+2.10}_{-2.10}$	$11.27^{+12.07}_{-10.12}$
EDCSNJ1301383−1140011†	13:01:38.3445	-11:40:01.197	0.4794	$3.63^{+0.67}_{-0.75}$	$5.09^{+2.75}_{-2.58}$
EDCSNJ1301441−1140589	13:01:44.1493	−11:40:58.995	0.4842	$3.98^{+0.83}_{-1.28}$	$1.89^{+1.44}_{-1.13}$
EDCSNJ1301524−1138043	13:01:52.4694	−11:38:04.391	0.4843	$5.13^{+1.54}_{-1.42}$	$6.41^{+5.09}_{-3.54}$
SEDCSJ1302036−1137519*	13:02:03.6095	-11:37:51.978	0.4873	$3.09^{+0.64}_{-1.00}$	$0.66^{+0.51}_{-0.53}$
SEDCSJ1302292−1133316	13:02:29.2680	−11:33:31.606	0.4810	$5.50^{+1.64}_{-1.52}$	$14.86^{+8.38}_{-7.36}$
SEDCSJ1302415−1143157	13:02:41.5765	−11:43:15.746	0.4877	$4.37^{+1.91}_{-1.51}$	$10.76^{+22.42}_{-6.32}$

Notes. Galaxies with low $\mu_{\rm H_2}$ are identified with †. Galaxies with CO upper-limits are identified with *. $^{(a)}$ Galaxy with $z_{\rm LDP}$ as $z_{\rm spec}$.

exported to be analysed using GILDAS[2]. The *i*-band images of our targets, the CO maps and spectra are shown in Fig. A.1.

3. Derived parameters

3.1. CO flux and molecular gas mass

Fluxes, $S_{\rm CO}\,\Delta V$, were extracted by integrating the CO(3-2) emission over the full spatial extent of the source using circular apertures with radii between 0.8″and 1.4″depending on the size of the galaxy. Following Lamperti et al. (2020), the error on the flux is defined as

$$\epsilon_{\rm CO} = \frac{\sigma_{\rm CO}\Delta V}{\sqrt{\Delta V \Delta w_{ch}^{-1}}}, \quad (1)$$

where $\sigma_{\rm CO}$ is the rms noise (in Jy) calculated in unit of spectral resolution Δw_{ch}, and ΔV (in km s^{-1}) is the width of the spectral window in which the line flux is calculated, $\Delta w_{ch} = 50.7$ km s^{-1}. All intensity maps and integrated spectra are shown in Fig A.1 of the Appendix. The full widths at half maximum (FWHM) are derived from single Gaussian fits of the emission lines. We obtain a median FWHM of 220 km s^{-1} with a standard deviation of 96 km s^{-1}, which is compatible with the type of massive galaxies we are studying (Freundlich et al. 2019).

Even if the targets are just slightly more extended than the beam size, a few of them show double peaked emission line, which is an indication of rotation. This will be analysed in a forthcoming paper.

The intrinsic CO luminosity associated to a transition between the levels J and $J-1$ is expressed as

$$L'_{\rm CO(J\rightarrow J-1)} = 3.25\times10^{7} S_{\rm CO(J\rightarrow J-1)}\Delta V\, \nu_{\rm obs}^{-2}\, D_{\rm L}^{2}\,(1+z)^{-3}, \quad (2)$$

where $L'_{\rm CO(J\rightarrow J-1)}$ is the line luminosity expressed in units of K km s^{-1}pc^2; $S_{\rm CO(J\rightarrow J-1)}\Delta V$ is the velocity-integrated flux in Jy km s^{-1}; $\nu_{\rm obs}$ is the observed frequency in GHz; $D_{\rm L}$ is the luminosity distance in Mpc; and z is the redshift of the observed galaxy (Solomon et al. 1997; Solomon & Vanden Bout 2005). The flux for our upper limit detections are defined as $3\times\epsilon_{\rm CO}$, with $\Delta V = 220$ km s^{-1}, the median value of our sample.

The total cold molecular gas mass ($M_{\rm H_2}$) is then estimated as

$$M_{\rm H_2} = \alpha_{\rm CO}\frac{L'_{\rm CO(J\rightarrow J-1)}}{r_{J1}}, \quad (3)$$

where $\alpha_{\rm CO}$ is the CO(1-0) luminosity-to-molecular-gas-mass conversion factor, considering a 36% correction to account for interstellar helium, and $r_{J1} = L'_{\rm CO(J\rightarrow J-1)}/L'_{\rm CO(1-0)}$ is the corresponding line luminosity ratio.

Just as in Paper I and for the sake of reliable comparison, we have considered $\alpha_{\rm CO} = 4.36\pm0.9\,M_\odot\,({\rm K\,km\,s^{-1}\,pc^2})^{-1}$, including the correction for helium, as a good estimate for normal star-forming galaxies (Dame et al. 2001; Grenier et al. 2005; Abdo et al. 2010; Leroy et al. 2011; Bolatto et al. 2013; Carleton et al. 2017). For the same reason, we assume $r_{31} = 0.5\pm0.05$ similarly to other intermediate to high-z studies (Bauermeister et al.

[2] http://www.iram.fr/IRAMFR/GILDAS

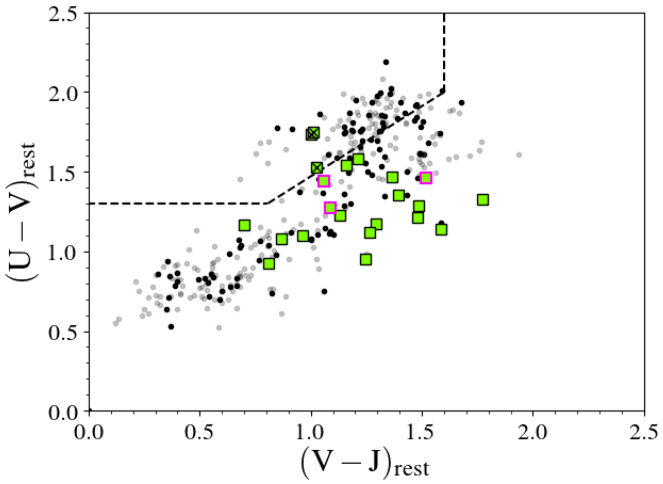

Fig. 4: Rest-frame UVJ colour–colour diagram. The dashed lines separate passive galaxies from star-forming ones (Williams et al. 2009). Our ALMA sample is in green. The black crosses mark the galaxies with CO upper-limits. The squares with the pink borders are for our low-μ_{H_2} galaxies (see Sect. 4.1). The grey points are the photometric redshift members with a K-band detection. The small black dots are the spectroscopic redshifts galaxies, within $3 \times \sigma_{cl}$ of the cluster redshift, also with a K-band detection.

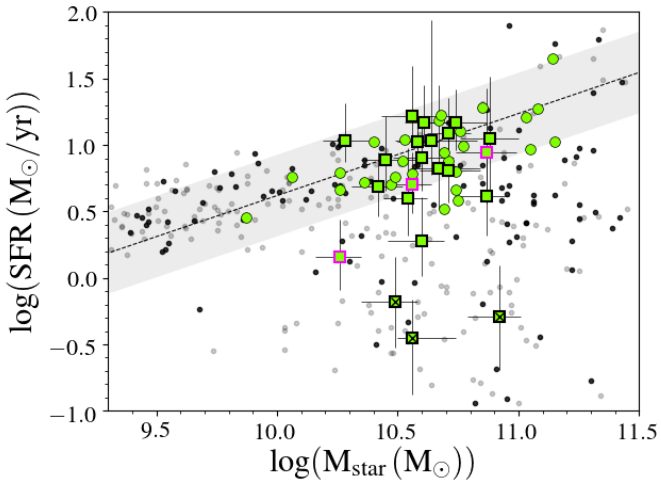

Fig. 5: Location of the CL1301 (grey) and ALMA (green squares) galaxies in the M_{star}–SFR plane. The galaxies with only upper limits in CO are identified with a cross. Squares with pink borders show the low-μ_{H_2} galaxies, see Sect. 4.1. Galaxies in black and grey are the spectroscopic and photometric samples, respectively, at the redshift of CL1301.7−1139. For comparison, the light green circles show the CL1411.1−1148 ALMA galaxies. The dashed black line is the Speagle et al. (2014) MS, corrected for a Chabrier IMF, at $z = 0.4828$, with the corresponding ±0.3 dex scatter as the grey shaded area.

2013b; Genzel et al. 2015; Chapman et al. 2015; Carleton et al. 2017; Tacconi et al. 2018)

The intrinsic CO(3-2) luminosity $L'_{CO(3-2)}$, the full width at half maximum, FWHM, the cold molecular gas mass M_{H_2}, the corresponding gas-to-stellar-mass ratio $\mu_{H_2} = M_{H_2}/M_{star}$, and the redshift of the CO emission of our sample galaxies are listed in Table 2.

3.2. Stellar masses and star formation rates

Stellar masses and SFRs were derived with MAGPHYS[3] (da Cunha et al. 2008), based on the u, g, r, i, z, and K_s total magnitudes. The stellar populations and dust extinction models are those of Bruzual & Charlot (2003) and Charlot & Fall (2000). MAGPHYS provides probability density functions (PDFs) for each parameter, like SFR, M_{star}, dust mass, and dust temperature. Their values in this work correspond to the peak values of the PDFs. The uncertainties are the 68% confidence interval of the PDFs. The photometric wavelength coverage does not allow the identification of active galactic nuclei (AGNs), which could affect the SFRs in particular. However, the analysis of the galaxy spectra, in particular, the [O II] to Hβ line ratio suggests that they are not typical AGNs (Sánchez-Blázquez et al. 2009; Rudnick et al. 2017b). These are anyway rare in clusters, less than 3% (Miller et al. 2003; Kauffmann et al. 2004; Mishra & Dai 2020).

Figure 5 presents the position of our ALMA targets relative to the main sequence (MS) of normal star-forming galaxies at the cluster redshift as inferred by Speagle et al. (2014). Only galaxies with spectroscopic or photometric redshift and with K_s photometry are shown. Indeed the NIR flux allows for the most robust mass and SFR estimates. Almost two thirds (65%) of our ALMA targets fall within the ±0.3 dex dispersion of the MS. Three ALMA targets fall much below the −0.3 dex boundary, in between the MS and the red sequence, SEDCSJ1301349−1146512, EDCSNJ1301344−1142380, and EDCSNJ1301441−1140589. These are systems in the transition region between star-forming and passive systems. Two of those are bona fide cluster members (EDCSNJ1301344−1142380 and EDCSNJ1301441−1140589), while SEDCSJ1301349−1146512 is located at a distance of $\sim 2R_{200}$, however still within $v/\sigma_{cl} < 1$, and therefore most probably an infalling system (Mahajan et al. 2011). All but three are detected in CO. Finally, three galaxies turn out to be on the passive sequence ($\log(SFR) \lesssim -0.2$). Two of them (EDCSNJ1301336−1138071 and EDCSNJ1301336−1138090 are cluster members), while SEDCSJ1302036−1137519 is an infalling system ($\sim 1.5R_{200}$ and still within $v/\sigma_{cl} \sim 1.5$). We could only place upper limits on their CO fluxes. It would be tempting to attribute their lack of star formation activity and their CO deficiency to their early-type morphologies. However, similar systems without evidence of disks in Fig. A.1 have nevertheless been detected in CO.

Figure 6 provides an overview of the galaxy specific star formation rates (sSFR) as a function of redshift from ∼ 0.02 to ∼ 2 for galaxies with existing CO line fluxes. The list of our comparison samples is identical to Paper I where their exact composition, redshift range, selection and CO line transitions, are detailed (Gao & Solomon 2004; García-Burillo et al. 2012; Saintonge et al. 2017; Baumgartner et al. 2013; Lamperti et al. 2020; Abdo et al. 2010; Bauermeister et al. 2013a,b; Morokuma-Matsui et al. 2015; Cybulski et al. 2016; Castignani et al. 2020; Jablonka et al. 2013; Geach et al. 2009, 2011; Tacconi et al. 2010, 2013, 2018; Freundlich et al. 2019; Spilker et al. 2018; Hayashi et al. 2018; Daddi et al. 2010; Noble et al. 2017, 2019; Rudnick et al. 2017a). The galaxy stellar masses of these comparison samples were originally derived by SED fitting, assuming either a 'Chabrier' or a 'Kroupa' IMF (Kroupa 2001; Chabrier 2003). We have con-

[3] http://www.iap.fr/magphys/index.html

Table 2: CO redshift, line-integrated flux, line width, luminosity of the CO(3-2) emission, cold molecular gas masses, cold molecular gas-to-stellar mass ratios, and gas depletion times of the ALMA targets.

IDs	z_{CO}	$S_{CO(3-2)}\Delta V$ (Jy km s^{-1})	FWHM (km s^{-1})	$L'_{CO(3-2)}$ (10^8 L$_\odot$)	M_{H_2} (10^9 M$_\odot$)	μ_{H_2}	t_{depl} (Gyr)
SEDCSJ1300003−1144203	0.4879	0.600 ± 0.020	440 ± 40	8.295 ± 0.280	7.23 ± 0.24	$0.155^{+0.066}_{-0.048}$	$1.089^{+1.581}_{-0.753}$
SEDCSJ1300234−1132052†	0.4907	0.105 ± 0.014	230 ± 20	1.469 ± 0.198	1.28 ± 0.17	$0.017^{+0.007}_{-0.007}$	$0.145^{+0.161}_{-0.130}$
SEDCSJ1300324−1137445	0.4841	0.523 ± 0.013	190 ± 10	7.115 ± 0.176	6.20 ± 0.15	$0.171^{+0.067}_{-0.055}$	$0.376^{+0.330}_{-0.148}$
SEDCSJ1300340−1127269	0.4789	0.722 ± 0.013	180 ± 10	9.606 ± 0.176	8.38 ± 0.15	$0.210^{+0.067}_{-0.062}$	$1.038^{+0.705}_{-0.598}$
SEDCSJ1301007−1147075	0.4874^a	0.222 ± 0.010	180 ± 10	3.063 ± 0.132	2.67 ± 0.11	$0.102^{+0.028}_{-0.030}$	$0.550^{+0.330}_{-0.279}$
SEDCSJ1301044−1146232	0.4898^a	1.420 ± 0.016	310 ± 20	19.785 ± 0.235	17.25 ± 0.21	$0.905^{+0.219}_{-0.198}$	$1.603^{+1.052}_{-0.591}$
SEDCSJ1301144−1147490	0.4880	0.295 ± 0.013	240 ± 20	4.079 ± 0.181	3.56 ± 0.16	$0.126^{+0.043}_{-0.035}$	$0.456^{+0.342}_{-0.253}$
SEDCSJ1301216−1136480	0.4927	0.694 ± 0.013	260 ± 20	9.792 ± 0.192	8.54 ± 0.17	$0.166^{+0.038}_{-0.038}$	$0.699^{+0.435}_{-0.346}$
SEDCSJ1301240−1132137	0.4935^a	0.691 ± 0.008	140 ± 10	9.780 ± 0.120	8.53 ± 0.10	$0.209^{+0.051}_{-0.041}$	$0.574^{+0.370}_{-0.218}$
EDCSNJ1301323−1141558	0.4796	0.790 ± 0.010	180 ± 10	10.541 ± 0.135	9.19 ± 0.12	$0.242^{+0.053}_{-0.048}$	$0.874^{+0.463}_{-0.362}$
EDCSNJ1301336−1138071*	0.4869	< 0.026	...	...	< 0.32	< 0.009	< 0.882
EDCSNJ1301336−1138090*	0.4854	< 0.026	...	...	< 0.32	< 0.004	< 0.607
EDCSNJ1301344−1142380†	0.4854	0.140 ± 0.012	210 ± 10	1.915 ± 0.163	1.67 ± 0.14	$0.092^{+0.027}_{-0.029}$	$1.160^{+0.754}_{-0.662}$
SEDCSJ1301349−1146512	0.4843	0.344 ± 0.024	450 ± 20	4.684 ± 0.321	4.08 ± 0.28	$0.055^{+0.015}_{-0.019}$	$0.999^{+0.808}_{-0.670}$
EDCSNJ1301363−1138495	0.4785	0.295 ± 0.014	320 ± 20	3.917 ± 0.191	3.42 ± 0.17	$0.099^{+0.023}_{-0.027}$	$0.854^{+0.739}_{-0.562}$
SEDCSJ1301380−1127055	0.4819	0.465 ± 0.022	380 ± 20	6.266 ± 0.295	5.46 ± 0.26	$0.072^{+0.023}_{-0.023}$	$0.485^{+0.520}_{-0.436}$
EDCSNJ1301383−1140011†	0.4799	0.145 ± 0.015	160 ± 20	1.937 ± 0.196	1.69 ± 0.31	$0.047^{+0.017}_{-0.018}$	$0.332^{+0.190}_{-0.179}$
EDCSNJ1301441−1140589	0.4847	0.285 ± 0.008	160 ± 10	3.886 ± 0.114	3.39 ± 0.10	$0.085^{+0.020}_{-0.030}$	$1.793^{+1.363}_{-1.075}$
EDCSNJ1301524−1138043	0.4845	0.365 ± 0.011	180 ± 10	4.973 ± 0.155	4.34 ± 0.13	$0.085^{+0.028}_{-0.026}$	$0.676^{+0.538}_{-0.374}$
SEDCSJ1302036−1137519*	0.4873	< 0.097	...	...	< 1.17	< 0.038	< 1.769
SEDCSJ1302292−1133316	0.4813	0.580 ± 0.011	130 ± 20	7.797 ± 0.147	6.8 ± 0.13	$0.124^{+0.039}_{-0.037}$	$0.458^{+0.258}_{-0.227}$
SEDCSJ1302415−1143157	0.4877	0.295 ± 0.009	120 ± 10	4.074 ± 0.129	3.55 ± 0.11	$0.081^{+0.038}_{-0.031}$	$0.330^{+0.688}_{-0.194}$

Notes. Galaxies with low μ_{H_2} are identified with †. Galaxies with CO upper-limits are identified with *. $^{(a)}$ Galaxy with z_{LDP} as z_{spec}.

verted all masses to a Chabrier IMF using the relation of Zahid et al. (2012): $M_{star,C} = 0.94 \times M_{star,K}$.

Most existing datasets have focused on field galaxies, at the exception of Geach et al. (2009, 2011), Jablonka et al. (2013), Cybulski et al. (2016), Rudnick et al. (2017a), Hayashi et al. (2018), Noble et al. (2017, 2019) and Castignani et al. (2020). The present analysis provides the second largest sample at a fixed given redshift, the other one being our analysis of galaxies related to the CL1411.1−1148 environment. Both samples cover the same range of specific star formation rates and are uniquely tracing galaxies in interconnected cosmic structures around galaxy cluster.

One hypothesis raised in Paper I is that the selection criteria of the different CO galaxy surveys could impact our understanding of the relationship between galaxy stellar mass, star formation activity and cold molecular gas content. In order to help shed light on this issue, the left panel of Fig. 7 presents the galaxy sSFRs normalized to the position of the galaxies on the main sequence (sSFR/sSFR(MS, z, M_{star}) as originally put forward by Genzel et al. (2015). Galaxies are grouped in redshift slices and we distinguish between field and clusters samples.

While, as mentioned above, the galaxy stellar masses are derived in a relatively homogeneous way, the estimates of the SFRs rely on a much larger set of methods. The most common one is based on the galaxy far infrared (FIR) luminosity, sometimes taking into account the UV emission (Daddi et al. 2007, 2010; Tacconi et al. 2013; Cybulski et al. 2016; Hayashi et al. 2018; Noble et al. 2017, 2019; Freundlich et al. 2019). Another thread of studies use galaxy SED fits (Castignani et al. 2020; Rudnick et al. 2017a; Spérone-Longin et al. 2021). Wuyts et al. (2011) showed that in the low- to intermediate-SFR regime, SFR $\lesssim 50\,M_\odot yr^{-1}$, the values obtained by the two above methods, SFR_{UV+FIR} and SFR_{SED}, agree with each other within uncertainties. Finally, SFRs can be estimated from a set of emission lines, such as [O II], [O III], Hα, [N II], and [S II] (Bauermeister et al. 2013a,b). The slope and width of the MS provided by Speagle et al. (2014) take this variety of methods into account. Therefore the comparison of the different surveys and specifically the position of the galaxies in sSFR/sSFR(MS, z, M_{star}) is meaningful.

The difference in galaxy population between surveys is conspicuous in Fig.7. It does not depend on field or cluster environments, but rather on the target selection criteria, which results in a general over representation of galaxies above the main sequence. As a matter of fact, Bauermeister et al. (2013a,b) explicitly selected their targets with sSFR between 1 and 4 times that of MS galaxies. Similarly, prior detection at 24μm (e.g., Daddi et al. 2004; Cybulski et al. 2016), or some of the `Herschel` bands (e.g., Daddi et al. 2010; Castignani et al. 2020) does play a role in this bias toward actively star forming systems, unless it is purposely controlled to include systems below the main sequence, as it was done by the PHIBSS1/2 field surveys at $0.5 < z < 0.8$ (e.g., Tacconi et al. 2010, 2013; Freundlich et al. 2019). Very noticeably, our CL1301.7−1139 and CL1411.1−1148 samples, without any prior on previous FIR detection and in the vicinity of high density environments, are devoid of galaxies above the main sequence.

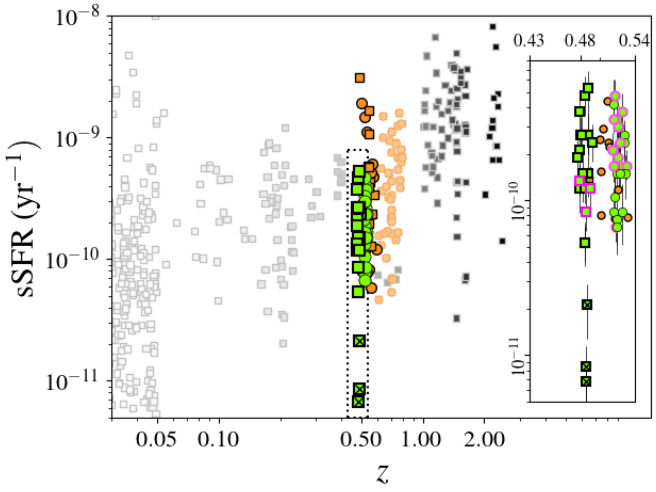

Fig. 6: Specific star formation rates as a function of redshift. The green markers identify the ALMA targets from both our clusters, with the circles for CL1411.1−1148 and the squares for CL1301.7−1139. The pink outlines are showing the galaxies with low gas fraction, as defined in Sect. 4.1. The orange circles stand for the PHIBSS2 galaxies, with dark colour for the systems at $0.49 < z \leq 0.6$ and lighter one for the galaxies at $0.6 < z \leq 0.8$. The orange squares are for the Castignani et al. (2020) luminous infrared galaxies (LIRGs) with $0.45 < z < 0.55$. We provide a zoom-in of the region delineated by the dotted lines (see inset), around the redshift of CL1301.7−1139.

4. Results

4.1. Gas fractions

The right panel of Fig. 7 presents the distribution of the galaxy gas fraction, $\mu_{H_2} = M_{H_2}/M_{star}$, corresponding to the distribution in normalized sSFRs of the left panel. The cold molecular gas masses are derived using the same value of α_{CO}, $\alpha_{MW} = 4.36\, M_\odot (\mathrm{K\,km\,s^{-1}\,pc^2})^{-1}$, for most samples (Daddi et al. 2010; Geach et al. 2011; Tacconi et al. 2010, 2013; Bauermeister et al. 2013a,b; Cybulski et al. 2016; Rudnick et al. 2017a; Hayashi et al. 2018; Noble et al. 2017, 2019). The other samples have linked the value of their CO-to-H_2 conversion factor either to metallicity (Freundlich et al. 2019), or to the position of the galaxy with respect to the MS (Castignani et al. 2020). Considering α_{MW} for these two samples slightly redistributes the position of the galaxies within the distributions, but does not modify their global shapes and mean positions. It stands out from Fig. 7 that samples that are skewed towards high sSFRs also have higher galaxy gas mass fractions. This is particularly the case at $z \leq 0.8$. At $z > 1$, the galaxy star formation activity is not sufficient to explain the very significant enhancement of the galaxy cold gas content and evolution with lookback time is an important factor.

Our CL1301.7−1139 and CL1411.1−1148 samples do not cover the high-μ_{H_2} tail of the other distributions, but do not reach particularly low values either, in particular with respect to PHIBSS2, which is the best field counterpart to our study. Just as in the case of CL1411.1−1148, differences in μ_{H_2} appear when it is matched with the galaxy M_{star}. This is done in Fig. 8.

In Paper I, we had identified a subset of star-forming galaxies with low gas mass fractions for their stellar mass. More specifically, these galaxies were falling below the $1 \times \sigma_{H_2}$ dispersion of the M_{star}–μ_{H_2} relation derived at $z = 0.55$ from the PHIBSS2 field galaxies at $0.5 < z \leq 0.6$. In order to look for a similar type of galaxies around CL1301.7−1139, we first need to set the relation between M_{star} and μ_{H_2} at $z = 0.45$. Tacconi et al. (2018) showed that the slope, in logarithmic scale, of the M_{star}–μ_{H_2} relation for MS galaxies does not vary with redshift and that only a zero point shift should be taken into account. Therefore, the M_{star}–μ_{H_2} relation for field MS systems is shown in Fig. 8 with a constant slope of −0.82 and a shift of −0.08 dex, induced by the transition from $z = 0.55$ to $z = 0.45$. This new relation is shown together with the $\pm 1 \times \sigma_{H_2}$ interval, with $\sigma_{H_2} = 0.37$ the variance of the M_{star}–μ_{H_2} relation calculated in Paper I.

We stress that the identification of the low-μ_{H_2} galaxies is drawn relative to field surveys. It does not necessarily imply that these star-forming galaxies have a low cold gas content in absolute terms, but rather that at least they were missing from earlier investigation. We explore to which extent their properties could be linked to the high density environments, themselves or their close vicinity, we are focusing on.

The three passive galaxies of Fig. 5 are not considered in this analysis, because we focus on still active systems. Therefore, following the same criterion as in Paper I, three star forming galaxies fall below the $-1 \times \sigma_{H_2}$ line of the M_{star}–μ_{H_2} relation. They are highlighted with a pink outer edges in all figures. This is formally a much smaller fraction (14%) than for CL1411.1−1148 (37%). Nevertheless, in a similar way as for CL1411.1−1148, at the exception of one galaxy, all our targets fall on the low $1 \times \sigma_{H_2}$ part of the M_{star}–μ_{H_2} relation, possibly reflecting the fact that our sample does not contain galaxies with star formation rates above the main sequence (Figs. 5 and 7).

Figure 9 presents the relation between μ_{H_2} and sSFR normalised to the galaxy position on the MS. Two of the low-μ_{H_2} galaxies are located on the main sequence, and one falls below it. This latter system, EDCSNJ1301344−1142380, is a cluster member. It is interesting to see that while its star formation activity is diminished and its gas content correspondingly low for its stellar mass, it lies however at the same level of μ_{H_2} as other (more massive) MS galaxies in Fig. 9. However, cluster members are not necessarily depleted in cold gas. Indeed, as alluded in Section 3.2, the galaxies below the main sequence are linked to the cluster environment, and this before their reservoir of cold gas is impacted for two of them.

The other low-μ_{H_2} cluster member is EDCSNJ1301383−1140011, and still is on the main sequence, but on the lower edge. The third low-μ_{H_2} galaxy is SEDCSJ1300234−1132052 again on the main sequence and on the lower edge. It is located far from the cluster core ($r > 5.5 R_{200}$) and does not belong to any identified overdensity.

We performed a Anderson–Darling (A-D) test (Scholz & Stephens 1987) between the μ_{H_2} distributions of the main-sequence PHIBSS2 and CL1411.1−1148 galaxies. It results in $p = 0.021$, meaning that there is only a 2.1% chance that the two samples arise from the same μ_{H_2} distribution. Similarly, combining both CL1301.7−1139 and CL1411.1−1148 gives p-value of 0.011, suggesting that these samples are not drawn from a PHIBSS2-like population at a 98.9% confidence level.

4.2. Comparison with CL1411.1−1148

The difference in fraction of low-μ_{H_2} galaxies in CL1301.7−1139 and CL1411.1−1148 is puzzling, given their similar properties in mass, redshift, and the identical target selection criteria that we applied. As seen in Fig. 5, the ALMA targets linked to CL1411.1−1148 span a slightly more extended stellar mass range than those linked to CL1301.7−1139. However their distributions have the same

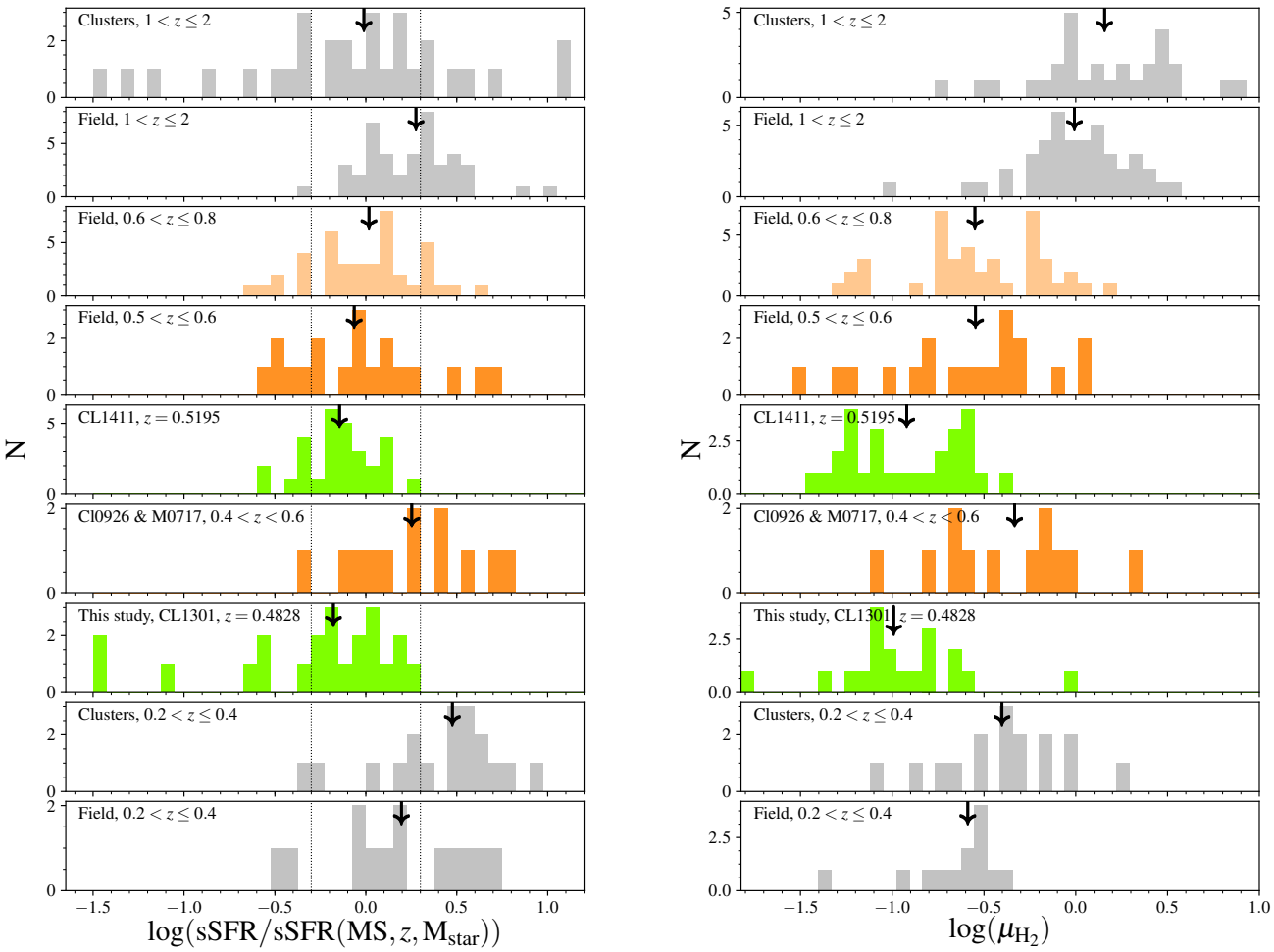

Fig. 7: Distribution of the sSFR normalised to the sSFR of the main-sequence, on the left panel, and of the molecular gas-to-stellar mass ratio, μ_{H_2}, on the right panel, for different redshift ranges and galaxy samples. Both our ALMA samples CL1411.1−1148 and CL1301.7−1139 are in green. The PHIBSS2 sample, constituted of field galaxies, is divided into 2 redshift subsamples, one at $0.5 \leq z \leq 0.6$ and the other one at $0.6 < z \leq 0.8$. A subsample of the Castignani et al. (2020) LIRGs within clusters Cl 0926+1242 and MACS J0717.5+3745. The cluster sample at lower redshifts comprises the rest of the Castignani et al. (2020) LIRGs, as well as Geach et al. (2011) and Cybulski et al. (2016) cluster galaxies. The field samples at the bottom and top part of both panels, as well as the cluster sample on top, contain galaxies from the literature at the corresponding redshifts. The black arrows correspond to the medians of each sample. The same value of α_{CO} has been used for all samples.

median, $\log(M_{star}/M_{\odot}) = 10.69$ and 10.6, respectively. Some of the CL1301.7−1139 ALMA targets have diminished SFRs, placing them further below the main sequence than in the case of CL1411.1−1148, but these galaxies do not form the bulk of the low-μ_{H_2} systems. Therefore, the origin of the difference between the two samples must be found elsewhere.

Figure 10 shows the projected phase-space diagrams of the two clusters. Following Jaffé et al. (2015), we assume a Navarro-Frenck-White (NFW) halo profile with a concentration c=6, to compute the escape velocity for our clusters (dotted lines). Here, we only look at star-forming galaxies as identified from the *UVJ* or *ugi* diagrams (black dots), because they are those for which we can define the low-μ_{H_2} systems. The spectroscopic members, including the ALMA targets, within $4\,\sigma_{cl}$ and $8 \times R_{200}$, are seen relatively to the virialized, infall, and escape region boundaries (see also Mahajan et al. 2011). Galaxies are considered infalling onto the clusters when they are located between 1 and ∼ 5 virial radii (Oman et al. 2013; Albæk et al. 2017). The difference between the two samples stands out: most of the ALMA targets are located inside the CL1411.1−1148 infall region, while they are much more spatially scattered in the case of CL1301.7−1139. Furthermore, all low-μ_{H_2} galaxies are located either inside or very close to the cluster core, or again within or very close to the CL1411.1−1148 infalling region. Leaving aside the clusters themselves, these low-μ_{H_2} galaxies represent 44% of the full infalling population, and 66% of the ones located between 1 and $4 \times R_{200}$. Applying these fractions to CL1301.7−1139 we could in principle have expected 1 or 2 low μ_{H_2} infalling galaxies, while we found none. This absence most likely reflects the fluctuations induced by low number statistics, given that we only observed 3 CL1301.7−1139 star forming galaxies between 1 and $4 \times R_{200}$. This is a strong hint that the population of low-μ_{H_2} galaxies are preferentially induced by the cluster environment. The interplay between the removal of cold gas reservoir or at least the change its properties and the decrease in SFR is subtle and difficult to catch in the act. The cluster infall regions seem

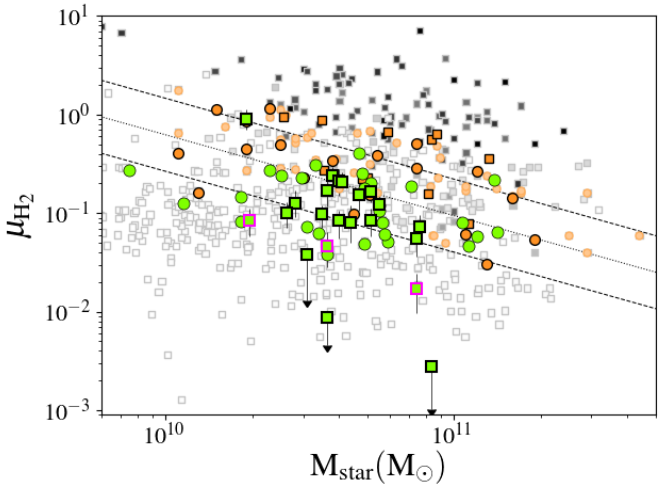

Fig. 8: Fraction of cold molecular gas as a function of the galaxy stellar mass. The colours and shapes of the markers are the same as on Fig. 6. The dotted line is the fit of the M_{star}–μ_{H_2} relation at $z \sim 0.45$ and derived from the relation for the PHIBSS2 galaxies at $z \sim 0.5$, with its dispersion being represented by the two dashed lines. The pink outlined green markers are for the CL1301 low-μ_{H_2} galaxies located below the $1\times\ \sigma_{H_2}$ line of the M_{star}–μ_{H_2} relation for the PHIBSS2 field galaxies.

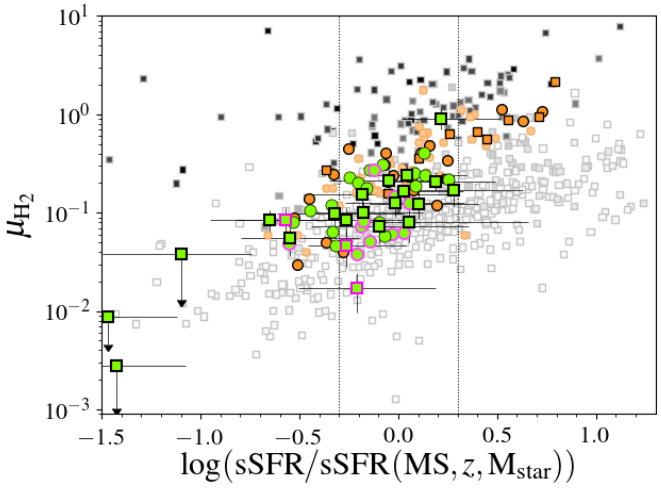

Fig. 9: Fraction of cold molecular gas as a function of the normalised specific SFR. The colours and shapes of the markers are the same as on Fig. 6. The dotted vertical lines represent the extent of the MS. The pink outlined green markers are for the low-μ_{H_2} galaxies from both ALMA samples.

to be the best place to look for them and identify the physical processes at play. Future follow-up studies of the same type will assess the significance and origin of the transformation of galaxies along their path to the cluster cores.

5. Conclusion

We have presented the analysis of the molecular gas content, derived from ALMA CO(3-2) line observations, of a sample of 22 galaxies located within CL1301.7−1139 ($z = 0.4828$, $\sigma_{cl} = 681\,km\,s^{-1}$) and in its surrounding large-scale structure.

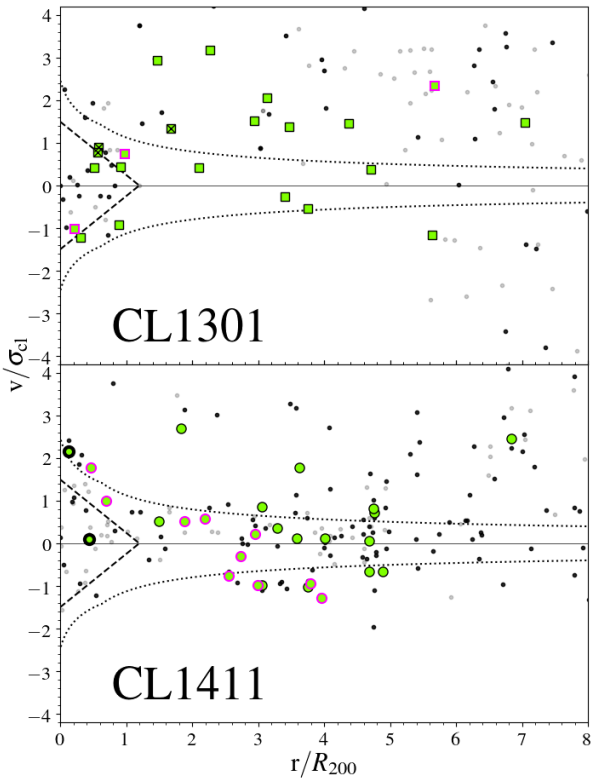

Fig. 10: Projected phase-space diagrams CL1301.7−1139 (top panel) and CL1411.1−1148 (bottom panel). The star-forming (black dots) and passive (gray points) galaxies with spectroscopic redshifts are identified in the UVJ diagram for CL1411.1−1148. As to CL1301.7−1139, when Ks band photometry is missing, the distinction between the two types of galaxies is also based on the positions of the red sequence, and the blue clump in the colour-magnitude diagrams using the u, g, and i bands. Assuming a NFW halo (Navarro et al. 1996), the area under the influence of the cluster potential, either from small relative velocities or small distance to the cluster cores, is shown with the dotted black line. The cluster virialized regions are located inside the regions delimited with dashed lines.

Unlike previous works, our sample selection does not impose a minimum galaxy star formation rate or detection in FIR. As such and as much as possible, it delivers an unbiased view of the gas content of normal star forming galaxies at $z \sim 0.5$. At the same time, it offers an insight on the status of the molecular gas content of galaxies in interconnected cosmic structures.

Our study highlights the variety of paths to star formation quenching, and most likely the variety of physical properties (i.e., temperature, density) of the corresponding galaxy cold molecular gas.

- Similarly to our first results on the analysis of the large scale structure around CL1411.1−1148 presented in Paper I, although to a smaller extent, our observations in CL1301.7−1139 reveal a number of star forming galaxies with lower gas fraction, at fixed stellar mass, than what had been found in previous surveys at comparable redshifts.
- The cluster environment does not necessarily affect the galaxy molecular gas content. Eight of our ALMA targets are bona fide CL1301.7−1139 members ($r \lesssim R_{200}$ and $v/\sigma_{cl} \lesssim 1$).

From those, only two show signs of lower gas fractions for their stellar masses when compared to the relation between these two quantities derived for field galaxies. One of them is nevertheless still on the star-forming main sequence, hence with a normal activity. The second system shows evidence of transition towards the passive sequence.

• Star formation and cold gas content are indeed not always linked in a straightforward manner. Three of our ALMA targets fall below the −0.3 dex boundary of the star-forming main sequence. These are systems in the transition region between star-forming and passive systems. While two of those are bona fide cluster members, the third one is infalling. Only one of the cluster member, mentioned above, has a low gas fraction for its stellar mass, the other two galaxies are normal despite their lowered star forming activity and irrespective of their location.

• Three galaxies turn out to be on the passive sequence ($\log(\mathrm{SFR}) \lesssim -0.2$) and only have upper limits on their CO fluxes. The lack of star formation activity and their CO deficiency does not seem to be driven by morphology (internal quenching). Indeed, similar systems in our sample, without evidence of disks, have, nevertheless, well measured CO fluxes.

• The comparison with CL1411.1−1148 highlights the enhanced fraction of galaxies with low gas fraction, compared to the field and at fixed stellar mass, in the cluster infall region. This provides a strong hint of environmental dependence and stress the needs for the extension of this type of investigations to a larger number of cluster and related large scale structure.

Acknowledgements. This paper makes use of the following ALMA data: ADS/JAO.ALMA#2017.1.00257.S. ALMA is a partnership of ESO (representing its member states), NSF (USA) and NINS (Japan), together with NRC (Canada), MOST and ASIAA (Taiwan), and KASI (Republic of Korea), in cooperation with the Republic of Chile. The Joint ALMA Observatory is operated by ESO, AUI/NRAO and NAOJ. The authors are indebted to the *International Space Science Institute* (ISSI), Bern, Switzerland, for supporting and funding the international team 'The Effect of Dense Environments on Gas in Galaxies over 10 Billion Years of Cosmic Time'. We are grateful to the `Numpy` (Oliphant 2006; Van Der Walt et al. 2011), `SciPy` (Virtanen et al. 2020), `Matplotlib` (Hunter 2007), `IPython` (Pérez & Granger 2007) and, `Astropy` (Robitaille et al. 2013; Price-Whelan et al. 2018) teams for providing the scientific community with essential Python tools.

References

Abdo, A. A., Ackermann, M., Ajello, M., et al. 2010, ApJ, 710, 133
Aghanim, N., Akrami, Y., Ashdown, M., et al. 2020, A&A, 641, A6
Albæk, L., Hansen, S. H., Martizzi, D., Moore, B., & Teyssier, R. 2017, MNRAS, 472, 3486
Bahé, Y. M., McCarthy, I. G., Balogh, M. L., & Font, A. S. 2013, MNRAS, 430, 3017
Balogh, M., Eke, V., Miller, C., et al. 2004, MNRAS, 348, 1355
Bauermeister, A., Blitz, L., Bolatto, A. D., et al. 2013a, ApJ, 768, 132
Bauermeister, A., Blitz, L., Bolatto, A. D., et al. 2013b, ApJ, 763, 64
Baumgartner, W. H., Tueller, J., Markwardt, C. B., et al. 2013, ApJS, 207, 19
Bianconi, M., Smith, G. P., Haines, C. P., et al. 2018, MNRAS Lett., 473, L79
Bigiel, F., Leroy, A., Walter, F., et al. 2008, ApJ, 136, 2846
Blanton, M. R. & Roweis, S. 2007, AJ, 133, 734
Bolatto, A. D., Wolfire, M., & Leroy, A. K. 2013, ARA&A, 51, 207
Boselli, A., Cortese, L., Boquien, M., et al. 2014, A&A, 564
Boselli, A., Mendes de Oliveira, C., Balkowski, C., Cayatte, V., & Casoli, F. 1996, A&A, 314, 738
Brammer, G. B., van Dokkum, P. G., & Coppi, P. 2008, ApJ, 686, 1503
Bruzual, G. & Charlot, S. 2003, MNRAS, 344, 1000
Carleton, T., Cooper, M. C., Bolatto, A. D., et al. 2017, MNRAS, 467, 4886
Castignani, G., Combes, F., Jablonka, P., et al. 2021, arXiv e-prints
Castignani, G., Jablonka, P., Combes, F., et al. 2020, A&A, 640, A64
Chabrier, G. 2003, PASP, 115, 763
Chapman, S. C., Bertoldi, F., Smail, I., et al. 2015, MNRAS Lett., 449, L68
Charlot, S. & Fall, S. M. 2000, ApJ, 539, 718
Cybulski, R., Yun, M. S., Erickson, N., et al. 2016, MNRAS, 459, 3287
da Cunha, E., Charlot, S., & Elbaz, D. 2008, MNRAS, 388, 1595
Daddi, E., Bournaud, F., Walter, F., et al. 2010, ApJ, 713, 686
Daddi, E., Cimatti, A., Renzini, A., et al. 2004, ApJ, 617, 746
Daddi, E., Dickinson, M., Morrison, G., et al. 2007, ApJ, 670, 156
Dame, T. M., Hartmann, D., & Thaddeus, P. 2001, ApJ, 547, 792
Dressler, A. 1980, ApJ, 236, 351
Finn, R. A., Zaritsky, D., McCarthy, D. W., et al. 2005, ApJ, 630, 206
Freundlich, J., Combes, F., Tacconi, L. J., et al. 2019, A&A, 622, A105
Gao, Y. & Solomon, P. M. 2004, ApJS, 152, 63
García-Burillo, S., Usero, A., Alonso-Herrero, A., et al. 2012, A&A, 539, A8
Geach, J. E., Smail, I., Moran, S. M., et al. 2011, ApJ, 730, L19
Geach, J. E., Smail, I., Moran, S. M., Treu, T., & Ellis, R. S. 2009, ApJ, 691, 783
Genzel, R., Tacconi, L. J., Lutz, D., et al. 2015, ApJ, 800, 20
Gomez, P. L., Nichol, R. C., Miller, C. J., et al. 2003, ApJ, 584, 210
Gouin, C., Aghanim, N., Bonjean, V., & Douspis, M. 2020, A&A, 635, A195
Grenier, I. A., Casandjian, J. M., & Terrier, R. 2005, Sci., 307, 1292
Guzzo, L., Bel, J., Bianchi, D., et al. 2018, arXiv e-prints
Haines, C. P., Pereira, M. J., Smith, G. P., et al. 2015, ApJ, 806, 101
Hayashi, M., Tadaki, K.-I., Kodama, T., et al. 2018, ApJ, 856, 118
Hunter, J. D. 2007, Computing in Science & Engineering, 9, 90
Jablonka, P., Combes, F., Rines, K., Finn, R., & Welch, T. 2013, A&A, 557, 8
Jachym, P., Combes, F., Cortese, L., Sun, M., & Kenney, J. D. P. 2014, ApJ, 792, 11
Jachym, P., Sun, M., Kenney, J. D. P., et al. 2017, ApJ, 839, 114
Jaffé, Y. L., Smith, R., Candlish, G. N., et al. 2015, MNRAS, 448, 1715
Just, D. W., Kirby, M., Zaritsky, D., et al. 2019, ApJ, 885, 6
Kauffmann, G., White, S. D., Heckman, T. M., et al. 2004, MNRAS, 353, 713
Koyama, S., Koyama, Y., Yamashita, T., et al. 2017, ApJ, 847, 137
Kroupa, P. 2001, MNRAS, 322, 231
Laigle, C., Pichon, C., Arnouts, S., et al. 2018, MNRAS, 474, 5437
Lamperti, I., Saintonge, A., Koss, M., et al. 2020, ApJ, 889, 103
Lee, B., Chung, A., Tonnesen, S., et al. 2017, MNRAS, 466, 1382
Leroy, A. K., Bolatto, A., Gordon, K., et al. 2011, ApJ, 737, 12
Leroy, A. K., Walter, F., Brinks, E., et al. 2008, AJ, 136, 2782
Lisenfeld, U., Alatalo, K., Zucker, C., et al. 2017, A&A, 607, A110
Mahajan, S., Mamon, G. A., & Raychaudhury, S. 2011, MNRAS, 416, 2882
Malavasi, N., Pozzetti, L., Cucciati, O., Bardelli, S., & Cimatti, A. 2016, A&A, 585, A116
Martinez-Badenes, V., Lisenfeld, U., Espada, D., et al. 2012, A&A, 540, A96
McGee, S. L., Balogh, M. L., Bower, R. G., Font, A. S., & McCarthy, I. G. 2009, MNRAS, 400, 937
McMullin, J. P., Waters, B., Schiebel, D., Young, W., & Golap, K. 2007, Astron. Soc. Pacific Conf. Ser., 376, 127
Miller, C. J., Nichol, R. C., Gomez, P. L., Hopkins, A. M., & Bernardi, M. 2003, ApJ, 597, 142
Milvang-Jensen, B., Noll, S., Halliday, C., et al. 2008, A&A, 482, 419
Mishra, H. D. & Dai, X. 2020, AJ, 159, 69
Morokuma-Matsui, K., Baba, J., Sorai, K., & Kuno, N. 2015, PASJ, 67, 36
Morokuma-Matsui, K., Kodama, T., Morokuma, T., et al. 2021, arXiv e-prints
Navarro, J. F., Frenk, C. S., & White, S. D. M. 1996, ApJ, 462, 563
Noble, A. G., McDonald, M., Muzzin, A., et al. 2017, ApJ, 842, L21
Noble, A. G., Muzzin, A., McDonald, M., et al. 2019, ApJ, 870, 56
Oliphant, T. E. 2006, A guide to NumPy, Vol. 1 (Trelgol Publishing USA)
Oman, K. A., Hudson, M. J., & Behroozi, P. S. 2013, MNRAS, 431, 2307
Peng, Y.-j., Lilly, S. J., Kovac, K., et al. 2010, ApJ, 721, 193
Pérez, F. & Granger, B. E. 2007, Computing in Science and Engineering, 9, 21
Price-Whelan, A. M., Sipőcz, B. M., Günther, H. M., et al. 2018, AJ, 156, 123
Riess, A. G., Casertano, S., Yuan, W., Macri, L. M., & Scolnic, D. 2019, ApJ, 876, 85
Robitaille, T. P., Tollerud, E. J., Greenfield, P., et al. 2013, A&A, 558, A33
Rudnick, G., Hodge, J., Walter, F., et al. 2017a, ApJ, 849, 27
Rudnick, G., Jablonka, P., Moustakas, J., et al. 2017b, ApJ, 850, 181
Saintonge, A., Catinella, B., Tacconi, L. J., et al. 2017, ApJS, 233, 22
Sánchez-Blázquez, P., Jablonka, P., Noll, S., et al. 2009, A&A, 499, 47
Scholz, F. W. & Stephens, M. A. 1987, J. Am. Stat. Assoc., 82, 918
Schruba, A., Leroy, A. K., Walter, F., et al. 2011, ApJ, 142, 37
Scott, T. C., Usero, A., Brinks, E., et al. 2015, MNRAS, 453, 328
Skrutskie, M. F., Cutri, R. M., Stiening, R., et al. 2006, AJ, 131, 1163
Smith, G. P., Treu, T., Ellis, R. S., Moran, S. M., & Dressler, A. 2005, ApJ, 620, 78
Solomon, P. & Vanden Bout, P. 2005, ARA&A, 43, 677
Solomon, P. M., Downes, D., Radford, S. J. E., & Barrett, J. W. 1997, ApJ, 478, 144
Song, H., Laigle, C., Hwang, H. S., et al. 2021, MNRAS, 501, 4635
Speagle, J. S., Steinhardt, C. L., Capak, P. L., & Silverman, J. D. 2014, ApJS, 214, 15
Spérone-Longin, D., Jablonka, P., Combes, F., et al. 2021, A&A, 647, A156
Spilker, J., Bezanson, R., Barišić, I., et al. 2018, ApJ, 860, 103
Tacconi, L. J., Genzel, R., Neri, R., et al. 2010, Nature, 463, 781
Tacconi, L. J., Genzel, R., Saintonge, A., et al. 2018, ApJ, 853, 179
Tacconi, L. J., Neri, R., Genzel, R., et al. 2013, ApJ, 768
Van Der Walt, S., Colbert, S. C., & Varoquaux, G. 2011, Computing in Science & Engineering, 13, 22
Virtanen, P., Gommers, R., Oliphant, T. E., et al. 2020, Nature Methods, 17, 261
White, S. D., Clowe, D. I., Simard, L., et al. 2005, A&A, 444, 365
Williams, R. J., Quadri, R. F., Franx, M., Van Dokkum, P., & Labbé, I. 2009, ApJ, 691, 1879
Wuyts, S., Förster Schreiber, N. M., Lutz, D., et al. 2011, ApJ, 738, 106
Zahid, H. J., Dima, G. I., Kewley, L. J., Erb, D. K., & Davé, R. 2012, ApJ, 757, 54

Appendix A: ALMA maps and spectra of our galaxies

In this appendix, we present the *i*-band images, the ALMA intensity maps and the spectra of all of our targets. The low μ_{H_2} targets are indicated as such by a label on the bottom left of their *i*-band image.

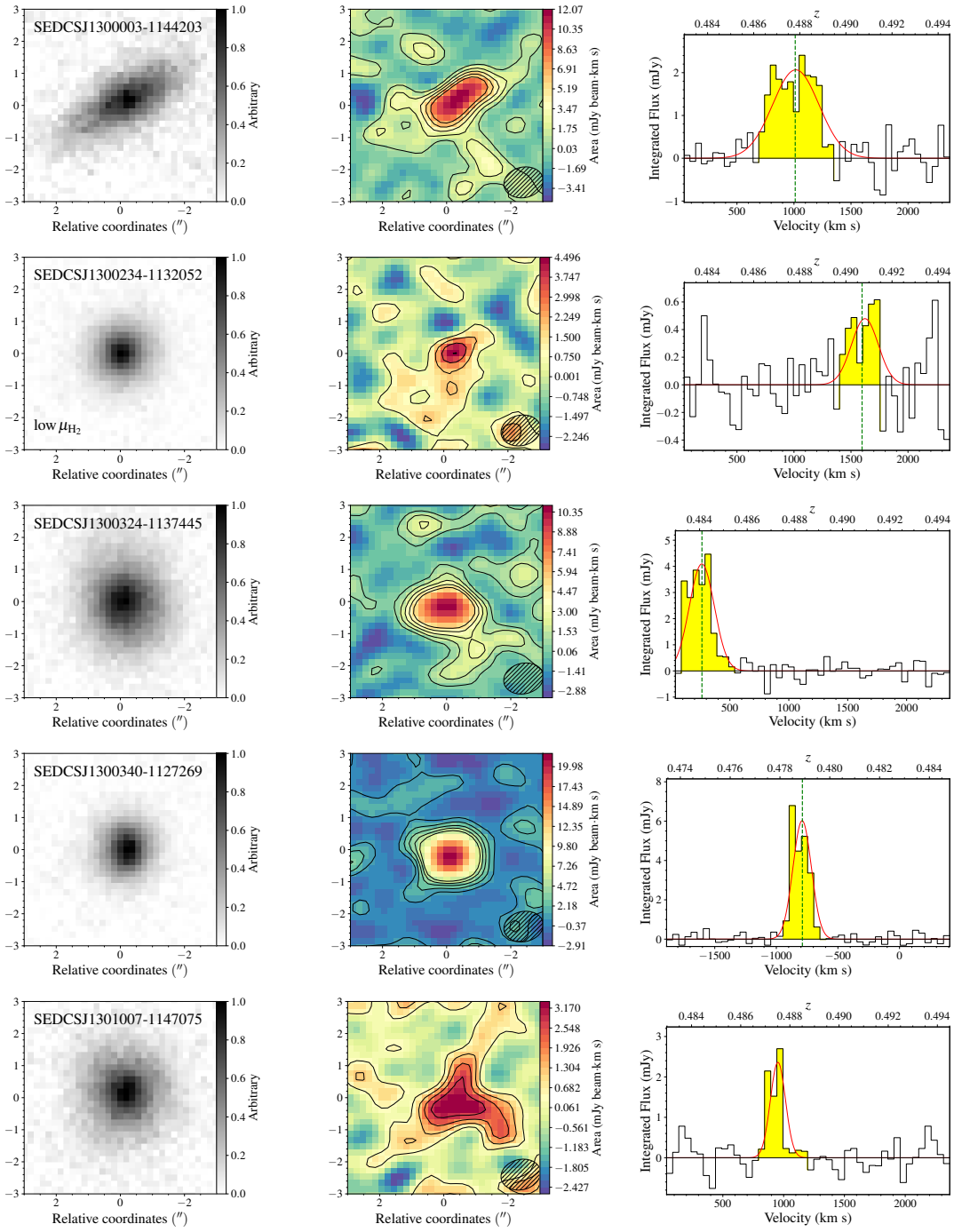

Fig. A.1: *Left*: CFHT/MEGACAM *i*-band images of our galaxies in a $6'' \times 6''$ snapshot, centred on the galaxies coordinates. *Middle*: ALMA map of the CO(3-2) emission around our galaxies. Spatial scale is the same as in the left panel. The colour wedge of the intensity map is in mJy/beam km s^{-1}. The contours are defined such that they are spaced by 2 times the rms and are between 1 and 9. In the bottom right corner is the beam size. *Right*: The spectra show the flux, S_{CO}, spatially integrated as indicated in Sect. 2.2, of the source in mJy in function of the velocity in km s^{-1}, with respect to the cluster redshift. The Gaussian profiles are fits of the emission lines from which we derived our FWHMs. The yellow filled zones correspond to the spectral extent of the emissions. The green vertical line corresponds to the spectroscopic redshift.

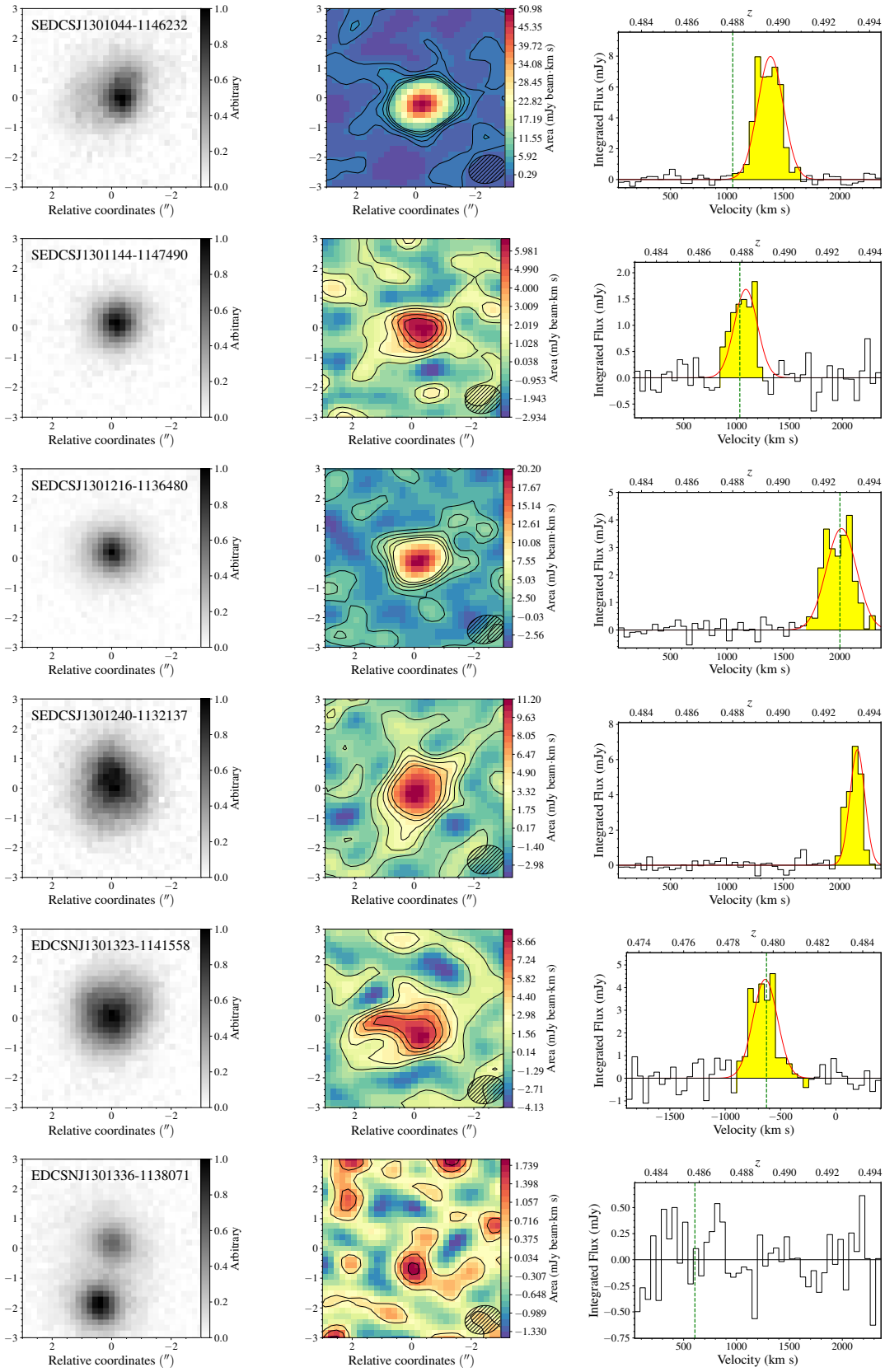

Fig. A.1: Continued.

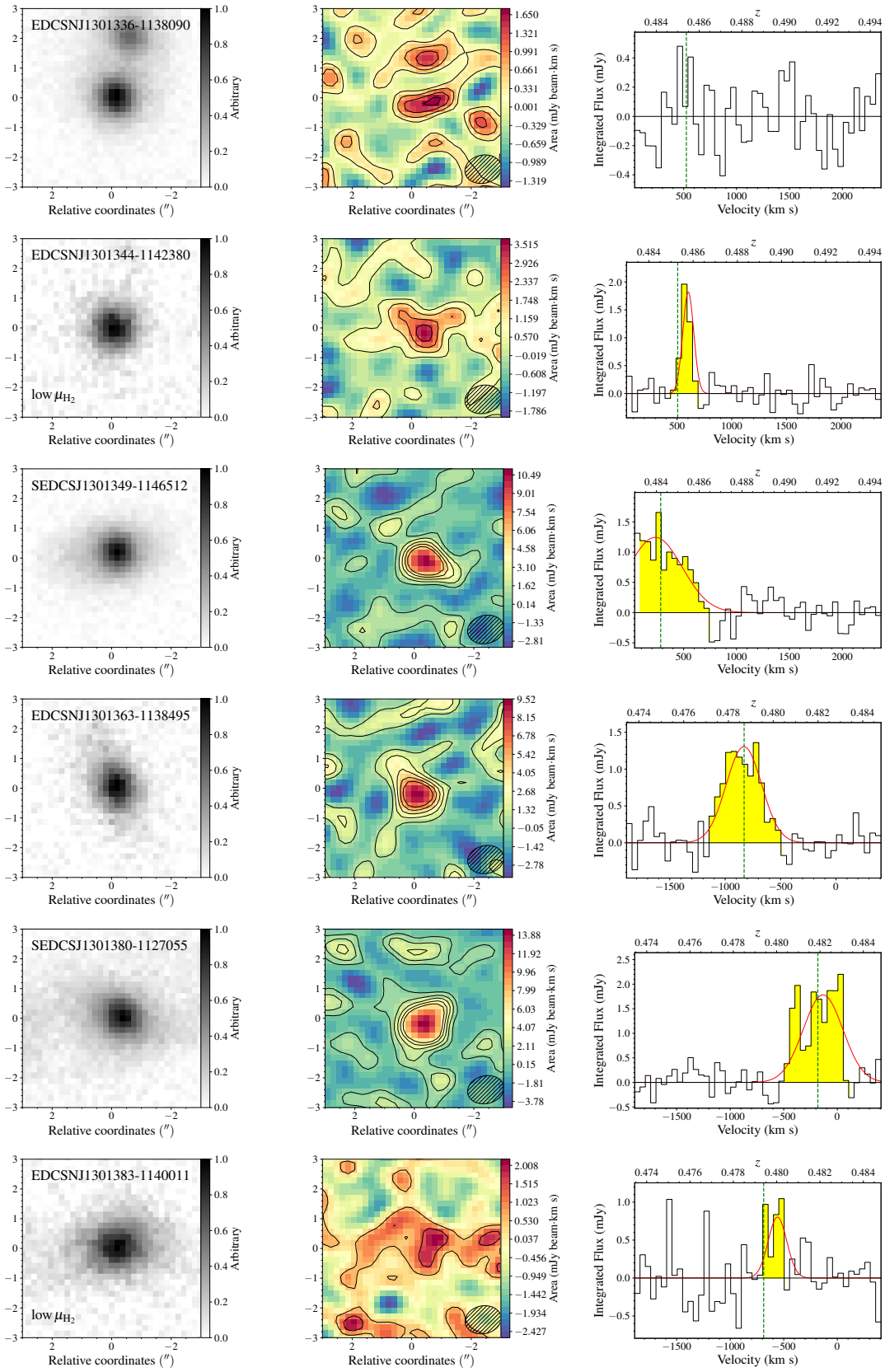

Fig. A.1: Continued.

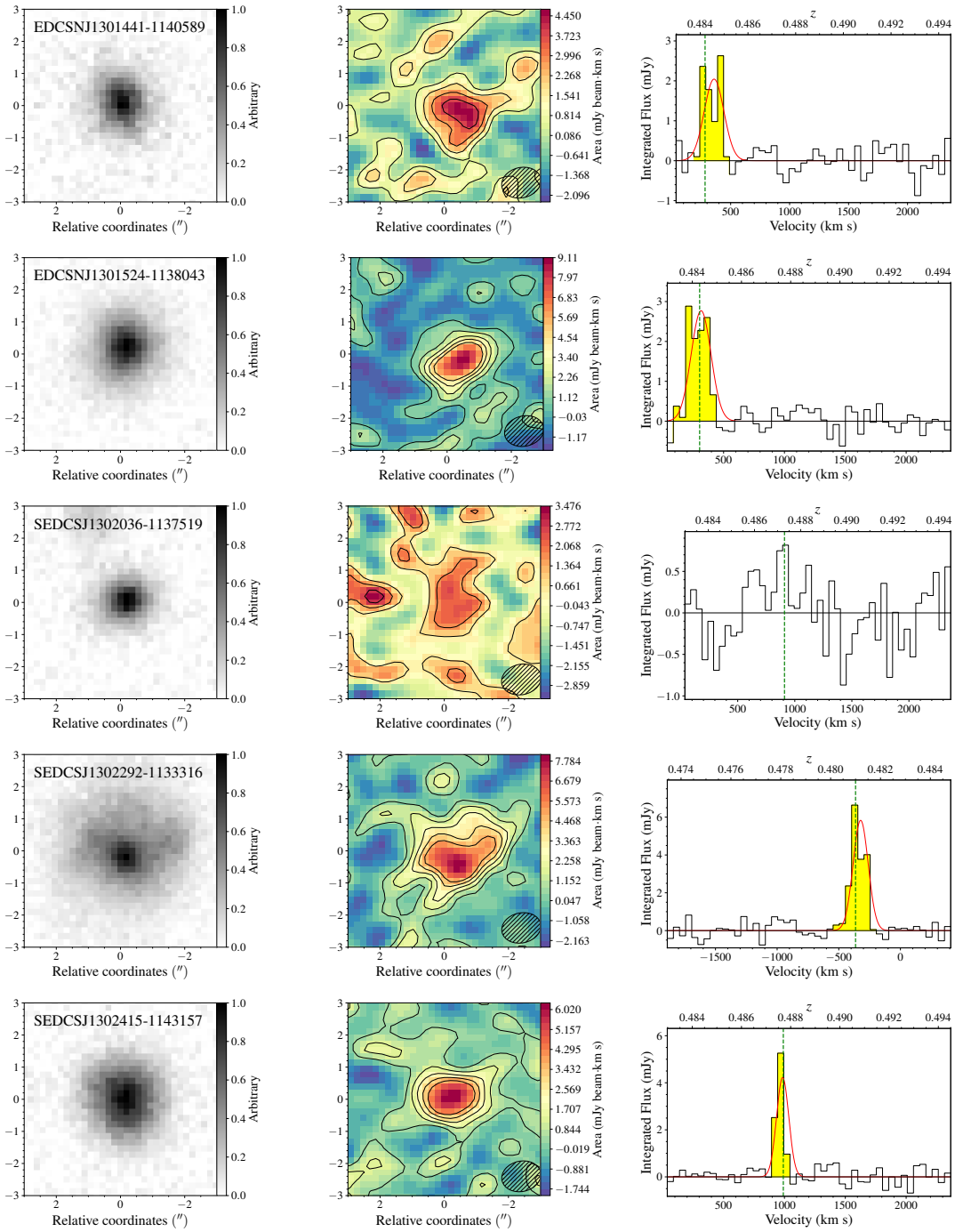

Fig. A.1: Continued.

5 Conclusions

The way the cold molecular gas reservoir of galaxies is modified during the winding down of star formation is an open question. The influence of the local environment on those reservoir is still fairly unknown. To date, most studies have focused on field galaxies or on galaxies within massive clusters. Large scale survey of the molecular gas content of galaxies evolving within the cosmic web surrounding the same cluster has never been done. SEEDisCS is the first study of this scale to solely focus on two medium-mass clusters and their surroundings to observe galaxies that have been evolving within the same part of the Universe. In this thesis, we report the results obtained from the ALMA observations of carefully selected galaxies within the cosmic web surrounding two clusters at an intermediate redshift of $z \sim 0.5$.

Chapter 2 presents some preliminary work performed before the stellar masses and SFRs derivation, the derivation in itself, and, finally, gives some details about the data reduction of the ALMA observations. In order to obtain robust estimates for the stellar mass and SFR for the galaxies at our disposal, we had to proceed with the correction of the stellar sequence, which is the common locus of stars lying on the stellar main sequence. We had to correct the u, r, and z bands by 0.25, -0.08 and 0.03 mag, respectively, for CL1301.7−1139. For CL1411.1−1148, we only had to correct two bands: u and z by 0.16 and 0.1 mag, respectively. The second correction we worked on was the aperture correction. Indeed, SExtractor, the routine used to obtain the fluxes and magnitudes of our sources, does not take all the flux coming from the source. Correcting that allowed us to recover $\sim$ 10% of 'missing' flux for our ALMA targets. Then, we explained the method we used to derive the stellar masses and SFRs of our sources. SED fitting was our method of choice, via the use of MAGPHYS. We only had six photometric bands for our sources: u, g, r, i, z, and K_s. To check for the robustness and accuracy of our methods we relied on four galaxies with far-IR fluxes coming from previous MIPS 24-micron observations performed during the EDisCS survey. These galaxies showed that the stellar masses derived from the six previous bands were accurate. The SFRs were found to be somewhat underestimated for the reddest of our galaxies, but proved to be reliable. Finally, we detailed the observational setup and explained the method used to reduce the data, through the standard method for ALMA observations and the tool called CASA. We also described the approach we used to measure the fluxes of the CO lines,

using another tool, GILDAS.

The selection of both CL1411.1−1148 and CL1301.7−1139 ALMA sample did not impose a minimum SFR or detection in far infrared. As a consequence, we were able to detect and study galaxies at a later stage in their evolution, which was not possible in previous surveys. And we also report a detection rate close to the one for the PHIBSS2 survey (Freundlich et al. 2019), which we are using for comparison.

The results and analysis for the first cluster, CL1411.1−1148, are shown in the form of an article in Chapter 3. From this first analysis, we report the discovery of a new type of star-forming galaxies with depleted CO reservoir, compared to other star-forming galaxies of the same stellar mass. Those galaxies represented 37% of our 27 ALMA galaxies. This population was also clearly deviant from the expected tail of a Gaussian distribution. However, no clear links were found between the depleted CO reservoirs and the local environment of those galaxies.

The results for the second cluster, CL1301.7−1139, are reported in Chapter 4. We also found this population of normal star-forming galaxies with depleted CO reservoir, but to a smaller extent in this cluster. Among the 8 cluster members we were targeting, only 2 had low CO content. One of them was still on the star-forming main sequence, while the other was transitioning towards a passive state. We also reported non-detection of CO for 3 galaxies that were lying within the passive sequence. Their lack of star formation and CO content can not be explained by their morphologies, because similar systems were detected in CO. We also showed that the cluster environment does not systematically affect the gas content of galaxies, even though most of our H_2-depleted galaxies seem to be induced by the cluster environment.

This thesis should be considered as a first step towards a systematic analysis of the evolution of galaxies and their gas reservoir within the same environment. For the first time, 27 and 22 galaxies were observed in CO inside and around two medium-mass, intermediate-redshift clusters: CL1411.1−1148 and CL1301.7−1139, respectively. It revealed the importance of also focusing on less active galaxies as they are potential sources of information on how cold gas reservoir and star forming activity are linked, and how it is affected by the interconnected structures around the clusters.

The new population of CO depleted but still actively star-forming galaxies opens up new questions. We do not know if the gas reservoirs of those galaxies changed its properties to still be able to fuel a ‘normal’ star-formation, or if the galaxy was on its way to transitioning towards a passive state. This thesis showed the variety of paths to star formation quenching, and most probably the variety of physical properties of the cold gas.

5.1 Future work

The possibilities to complete and improve this study are various. We present here a few of them, some are already underway. while others can be started in a near future.

In the last few months, we submitted a proposal to observe our ALMA galaxies and those around them with the Gemini Multi-Object Spectrograph (GMOS) in order to get more spectroscopically derived redshift allowing us to derive more precise local density maps, as well as, detecting the Hα line that would allow us to derive more accurate SFRs for our ALMA galaxies and the galaxies in the GMOS FoV.

An ALMA proposal has also been submitted but this time, more focused on infalling galaxies at higher redshift, $z \sim 0.8$, also targeting EDisCS clusters. This survey is aimed at studying the cold molecular gas of galaxies, which are being pre-processed in the large scale structures surrounding clusters.

Another idea would be to extend this ALMA survey and to target specifically galaxies in the transition regime of the M_{star}–SFR diagram, also called the 'green valley'. This would allow us to catch galaxies that are either transitioning towards a quenched regime, or galaxies that are rejuvenated.

As mentioned in the conclusion of Paper I, we could target the same galaxies in a lower CO transition, ideally $J = 1 \rightarrow 0$, in order to remove the effect of the conversion factor linked to higher CO transitions, and also to have a better idea of the global gas network of the galaxies, e.g. concentrated towards the centre, clumpy, or extended.

Finally, a morphology based analysis could also be beneficial to this survey. The resolution of the ground-based images at these redshifts greatly limits the accuracy of such a classification. We have a tool at our disposal, FIREDEC (Cantale et al. 2016), which can deconvolve ground-based images to resolutions close to those of the Hubble Space Telescope.

5.2 Outlook

Upcoming large-scale surveys, using different instruments like the Vera C. Rubin Observatory or the *Euclid* space telescope will observe millions and millions of galaxies in the optical and near-IR over the whole sky and get tens of millions of spectroscopic redshifts. This will also lead to the detections of hundreds of clusters at intermediate redshift, as well as the network of LSS surrounding them. Coupled with the Square Kilometer Array, an array of thousands of radio antennas that are based in Africa and Australia, will also be able to detect the LSS, using neutral hydrogen, H I, as a tracer. The cooperation of all those surveys will help our advance in understanding the influence on the environment on the gas content, morphologies and stellar populations of galaxies.

Bibliography

Allamandola, L. J., Tielens, A. G. G. M., & Barker, J. R. 1985, ApJ, 290, L25

Bahé, Y. M., McCarthy, I. G., Balogh, M. L., & Font, A. S. 2013, MNRAS, 430, 3017

Bertin, E. & Arnouts, S. 1996, A&AS, 117, 393

Bigiel, F., Leroy, A., Walter, F., et al. 2008, ApJ, 136, 2846

Boselli, A., Cortese, L., Boquien, M., et al. 2014, A&A, 564

Brammer, G. B., Whitaker, K. E., Van Dokkum, P. G., et al. 2009, ApJ, 706, L173

Bruzual, G. & Charlot, S. 2003, MNRAS, 344, 1000

Cantale, N., Jablonka, P., Courbin, F., et al. 2016, A&A, 589, A82

Carilli, C. & Walter, F. 2013, ARA&A, 51, 105

Castignani, G., Jablonka, P., Combes, F., et al. 2020, A&A, 640, A64

Chabrier, G. 2003, PASP, 115, 763

Charlot, S. & Fall, S. M. 2000, ApJ, 539, 718

Covey, K. R., Ivezić, Ž., Schlegel, D., et al. 2007, AJ, 134, 2398

Cowie, L. L. & Songaila, A. 1977, Nature, 266, 501

da Cunha, E., Charlot, S., & Elbaz, D. 2008, MNRAS, 388, 1595

Davé, R., Finlator, K., & Oppenheimer, B. D. 2012, MNRAS, 421, 98

Dressler, A. 1980, ApJ, 236, 351

Driver, S. P., Allen, P. D., Graham, A. W., et al. 2006, MNRAS, 368, 414

Duley, W. W. & Williams, D. A. 1981, MNRAS, 196, 269

Einasto, M., Deshev, B., Lietzen, H., et al. 2018, A&A, 610, A82

Eisenhardt, P. R. M., Marocco, F., Fowler, J. W., et al. 2020, ApJS, 247, 69

Ferrière, K. M. 2001, Rev. Mod. Phys., 73, 1031

Fillingham, S. P., Cooper, M. C., Wheeler, C., et al. 2015, MNRAS, 454, 2039

Finn, R. A., Desai, V., Rudnick, G., et al. 2010, ApJ, 720, 87

Freundlich, J., Combes, F., Tacconi, L. J., et al. 2019, A&A, 622, A105

Geballe, T. R., Burton, M. G., & Pike, R. E. 2017, ApJ, 837, 83

Gnedin, O. Y. 2003, ApJ, 582, 141

Gouin, C., Aghanim, N., Bonjean, V., & Douspis, M. 2020, A&A, 635, A195

Gunn, J. E. & Gott, J. R. I. 1972, Apj, 176, 1

Haines, C. P., Pereira, M. J., Smith, G. P., et al. 2015, ApJ, 806, 101

Halliday, C., Milvang-Jensen, B., Poirier, S., et al. 2004, A&A, 427, 397

Hashim, N., De Laurentis, M., Abidin, Z. Z., & Salucci, P. 2014, arXiv e-prints, 6

Herbst, E. 1995, Annu. Rev. Phys. Chem., 46, 27

Jachym, P., Combes, F., Cortese, L., Sun, M., & Kenney, J. D. P. 2014, ApJ, 792, 11

Kauffmann, G., White, S. D., Heckman, T. M., et al. 2004, MNRAS, 353, 713

Kodama, T., Smail, I., Nakata, F., Okamura, S., & Bower, R. G. 2001, ApJ, 562, L9

Koopmans, L. V. E. & Treu, T. 2003, ApJ, 583, 606

Koyama, Y., Kodama, T., Shimasaku, K., et al. 2008, MNRAS, 391, 1758

Kraljic, K., Arnouts, S., Pichon, C., et al. 2018, MNRAS, 474, 547

Kravtsov, A. V. & Borgani, S. 2012, ARA&A, 50, 353

Laigle, C., Pichon, C., Arnouts, S., et al. 2018, MNRAS, 474, 5437

Larson, R. B., Tinsley, B. M., & Caldwell, C. N. 1980, ApJ, 237, 692

Leger, A. & Puget, J. L. 1984, A&A, 500, 279

Lemaux, B. C., Gal, R. R., Lubin, L. M., et al. 2012, ApJ, 745, 106

Lequeux, J. 2005, Astronomy and Astrophysics Library, Vol. 75, The Interstellar Medium (Springer Berlin Heidelberg), 173–182

Leroy, A. K., Walter, F., Brinks, E., et al. 2008, AJ, 136, 2782

Lewis, I., Balogh, M., De Propris, R., et al. 2002, MNRAS, 334, 673

Lilly, S. J., Carollo, C. M., Pipino, A., Renzini, A., & Peng, Y. 2013, ApJ, 772, 119

Madau, P. & Dickinson, M. 2014, ARA&A, 52, 415

Malavasi, N., Pozzetti, L., Cucciati, O., Bardelli, S., & Cimatti, A. 2016, A&A, 585, A116

McMullin, J. P., Waters, B., Schiebel, D., Young, W., & Golap, K. 2007, Astron. Soc. Pacific Conf. Ser., 376, 127

Miller, C. J., Nichol, R. C., Gomez, P. L., Hopkins, A. M., & Bernardi, M. 2003, ApJ, 597, 142

Milvang-Jensen, B., Noll, S., Halliday, C., et al. 2008, A&A, 482, 419

Mishra, H. D. & Dai, X. 2020, AJ, 159, 69

Moore, B., Katz, N., Lake, G., Dressler, A., & Oemler, A. 1996, Nature, 379, 613

Moran, S. M., Ellis, R. S., Treu, T., et al. 2007, ApJ, 671, 1503

Muzzin, A., Wilson, G., Demarco, R., et al. 2013, ApJ, 767, 39

Odekon, M. C., Hallenbeck, G., Haynes, M. P., et al. 2017, ApJ, 852, 142

Olave-Rojas, D., Cerulo, P., Demarco, R., et al. 2018, MNRAS, 479, 2328

Patel, S. G., Kelson, D. D., Holden, B. P., et al. 2009, ApJ, 694, 1349

Peng, Y.-j., Lilly, S. J., Kovac, K., et al. 2010, ApJ, 721, 193

Perlmutter, S., Aldering, G., Goldhaber, G., et al. 1999, ApJ, 517, 565

Persic, M., Salucci, P., & Stel, F. 1996, MNRAS, 281, 27

Planck Collaboration. 2020, A&A, 641, A6

Poggianti, B. M., Moretti, A., Gullieuszik, M., et al. 2017, ApJ, 844, 48

Poggianti, B. M., von der Linden, A., De Lucia, G., et al. 2006, ApJ, 642, 188

Rérat, F. 2015, PhD thesis, EPFL, Lausanne

Riess, A. G., Casertano, S., Yuan, W., Macri, L. M., & Scolnic, D. 2019, ApJ, 876, 85

Riess, A. G., Filippenko, A. V., Challis, P., et al. 1998, AJ, 116, 1009

Rubin, V. C., Thonnard, N., & Ford, W. K., J. 1980, ApJ, 238, 471

Salerno, J. M., Martínez, H. J., Muriel, H., et al. 2020, MNRAS, 493, 4950

Sánchez-Blázquez, P., Jablonka, P., Noll, S., et al. 2009, A&A, 499, 47

Schaller, M., Gonnet, P., Chalk, A. B., & Draper, P. W. 2016, in PASC 2016 (Association for Computing Machinery, Inc)

Schruba, A., Leroy, A. K., Walter, F., et al. 2011, ApJ, 142, 37

Scott, T. C., Usero, A., Brinks, E., et al. 2013, MNRAS, 429, 221

Strateva, I., Ivezić, Ž., Knapp, G. R., et al. 2001, AJ, 122, 1861

Tanaka, M., Lidman, C., Bower, R. G., et al. 2009, A&A, 507, 671

van de Voort, F., Bahé, Y. M., Bower, R. G., et al. 2017, MNRAS, 466, 3460

Wagner, C. R., Courteau, S., Brodwin, M., et al. 2017, ApJ, 834, 53

Wechsler, R. H., Bullock, J. S., Primack, J. R., Kravtsov, A. V., & Dekel, A. 2002, ApJ, 568, 52

Wetzel, A. R., Tinker, J. L., Conroy, C., & van den Bosch, F. C. 2013, MNRAS, 432, 336

White, S. D., Clowe, D. I., Simard, L., et al. 2005, A&A, 444, 365

Zhang, H., Zaritsky, D., Behroozi, P., & Werk, J. 2019, ApJ, 880, 28

Zinger, E., Dekel, A., Kravtsov, A. V., & Nagai, D. 2018, MNRAS, 475, 3654

Damien Spérone-Longin — Curriculum Vitae

Personal Information

01-oct-1993, French
18 ave Francis Blanchard
01170 Gex – France
+33 (0)6 28 40 21 03
@ dam.sper@gmail.com
@damiensper
www.linkedin.com/in/damien-sprone-longin

Research Experience

PhD student LASTRO / Ecole Polytechnique Fédérale de Lausanne *Feb 2017-Mar 2021*

- First of its kind survey of the cold molecular gas content of galaxies inside and around clusters
- Reduction of high-quality data from the Atacama Large Millimeter Array and the NOrthern Extended Millimeter Array
- Derivation of physical parameters for galaxies using state-of-the-art softwares
- Publication of my results and analyses as two articles in peer-reviewed scientific journal (Astronomy & Astrophysics)
- Presentation of my results at IAU Symposium 359 (Mar 2020) and at the EAS Annual meeting (Jul 2020)

Supervisor : Prof. Pascale Jablonka

Postgraduate student IRAP, Toulouse *Mar 2016-Jun 2016*
Modelling and reconstruction of coronal shocks and study of particle acceleration in their vicinity
Supervisor : Dr. Alexis Rouillard

Postgraduate student SAAO, Cape Town *Jun 2015-Aug 2015*
Study of variable stars in order to create a routine to automatically detect the variability type of new stars and spent one week at the Southern African Large Telescope with my supervisor
Supervisor : Dr. Eric Depagne

Undergraduate student University of Glasgow *Oct 2014-Apr 2015*
6-month project on modelling the radio emission from hot chromospheric solar flare sources
Supervisor : Dr. Paulo Simões

Undergraduate student LESIA, Meudon *May 2014-Jul 2014*
Study of the periodicity of solar type-III radio emissions
Supervisor : Dr. Milan Maksimovic

Education

PhD of Science in Astrophysics *Feb 2017-Mar 2021*
Title : Cold gas the cosmic web around galaxy clusters
Ecole Polytechnique Fédérale de Lausanne, Switzerland

2nd year of MSc in Astronomy, Astrophysics & Spatial Engineering *Sep 2015-Jun 2016*
Dynamics of gravitational systems
Paris-Saclay University, Orsay, France

1st year of MSc in Physics *Sep 2014-Jun 2015*
Options : Exploring Planetary Systems, and Pulsars and Supernovae
Erasmus at the University of Glasgow, Glasgow, United Kingdom

3rd year of BSc in Physics *Sep 2013-Jun 2014*
Options : Outreach in Physics, and Introduction to Astronomy & Astrophysics
Paris Sud University, Orsay, France

1st and 2nd year in Classe Préparatoire aux Grandes Ecoles *Sep 2011-Jun 2013*
Options : Maths and Physics
Lycée Jean Perrin, Lyon, France

Skills

Operating systems : Unix, Linux

Programming languages : Python, IDL

Office softwares : LibreOffice, LaTeX

Scientific softwares : DS9, CASA, Gildas, Source Extractor

Languages : French (native), English (C1), German (A2)

Hobbies and Interests

Amateur astronomy, reading, travels, theater, video games, music, and cinema